Building Integration of a Solar Air Heating System

Fernando Superbi Guerreiro BSc MSc

Supervisors: Dr. Michael McKeever, Prof. David Kennedy,

Prof. Brian Norton

School of Electrical and Electronic Engineering

Technological University Dublin

Republic of Ireland

December 2023

ABSTRACT

In order to achieve the global carbon emission target, the high fraction of locally available renewable energy sources will become necessary to meet energy demand. Solar energy is one of the most important renewable sources locally available for use in space heating, cooling, hot water supply and power production. Building integrated solar thermal systems (BISTS) can be a potential solution towards the enhanced energy efficiency and reduced operational cost in built environment. The current research aimed at developing an active solar air heating collector for building integration. This system consisted of several asymmetric compound parabolic concentrating collectors with inverted transpired absorber stacked on the top of each other capable of receiving direct solar insolation for 8 hours/day during the summer season. An optical analysis was carried out with the assistance of a 3D ray tracing technique in order to investigate the optical performance through a parametric analysis, and thus to decide the design to be used as a prototype. It has dimensions of 0.42 m x 0.40 m x 1.25 m and concentration ration 2.28, able to absorb up to 67% of direct solar radiation in the period of operation. Subsequently, the prototype was experimentally tested by using five different air flow rates (22 – 60 kg/h) in open loop configuration. Experimental results show that, on clear days and in periods of high solar insolation (greater than 800 W/m^2), the airflow temperature rise varied between 12 ^{o}C (at the highest airflow rate) and 27 ^{o}C (at the smallest rate), characterising thus thermal efficiencies between 52 – 62%. After experimental characterisation, a thermal modelling based on energy balance was undertaken with the objective of simulating the collector's thermal performance for further control of multiple units connected altogether. Valida-

tion of this model indicates that it predicts data of air temperature delivered and energy collected with uncertainties of ± 2 ^{o}C and ± 50 W/m^2 of absorber area, respectively. The thermal modelling was also used to predict the thermal performance of three collectors connected in series and in parallel. The connection in series was able to deliver higher outlet airflow temperatures (higher than 70 ^{o}C on a clear day), whereas the connection in parallel can collect more useful heat but delivering the same airflow temperature as if it is leaving the first collector in series. Lastly, this model was used for simulating barley drying. Three scenarios were employed to fulfill energy requirements: using only a gas burner to heat the airflow to 60°C, combining a solar heating system with a gas burner to achieve the same temperature, and solely relying on the solar heating system without an air temperature limit. For a specific airflow level, the gas burner system consumed the most gas and had a solar fraction of 0, indicating full reliance on gas for heating. Conversely, the standalone Solar Air Heating System (SAHS) yielded less dried mass, but both configurations achieved a solar fraction of 1, signifying exclusive reliance on solar energy. Results demonstrate that incorporating solar air heating systems can significantly reduce the need for natural gas heating. Specifically, the gas burner + SAHS in parallel exhibited the lowest gas consumption and the highest solar fraction among all the gas burner-based systems.

DECLARATION

I certify that this thesis which I now submit for examination for the award of PhD, is entirely my own work and has not been taken from the work of others, save and to the extent that such work has been cited and acknowledged within the text of my work.

This thesis was prepared according to the regulations for graduate study by research of the Technological University Dublin and has not been submitted in whole or in part for another award in any other third level institution.

The work reported on in this thesis conforms to the principles and requirements of the TU Dublin's guidelines for ethics in research.

Signature

Date

Candidate

ACKNOWLEDGEMENT

I would like to express my sincere appreciation to the individuals and organizations who have provided support and guidance throughout my PhD journey. I am deeply grateful to my supervisors, Professor Mick McKeever, Professor David Kennedy, and Professor Brian Norton, for their unwavering encouragement, support, and valuable insights.

In addition, I would like to thank my thesis committee members for their constructive criticism and feedback, which significantly improved the quality of my research.

I am thankful for the welcoming and supportive research environment created by the staff and students of TU Dublin. Working with inspiring and talented individuals has been a privilege, and I am grateful for the collaborations and friendships that have emerged from this community.

My family has been a constant source of love, support, and encouragement throughout my academic journey, and I am deeply indebted to them for their sacrifices and unwavering belief in my abilities.

I would also like to acknowledge the invaluable support and encouragement of my friends, who have provided inspiration and motivation during the ups and downs of my research journey.

Finally, I would like to acknowledge the National Council for Scientific and Technological Development (CNPq: process number 233789/2014-6) for providing me financial support to complete this PhD.

LIST OF SYMBOLS

Acronyms

ACPC	Asymmetric Compound Parabolic Concentration
BISTS	Building Integratied Solar Thermal System
CFD	Computational Fluid Dynamics
CPC	Compound Parabolic Concentrator
ETC	Evacuated Tube Collector
IACPC	Inverted Absorber Compound Parabolic Concentrator
ODE	Ordinary Differential Equation
PV	Photovoltaic

Latin

A'_{abs}	Absorber area without the holes (m^2)
a_s	Altitude solar angle
A	Area (m^2)
C_p	Specific heat (J/(kg K))
C	Geometric concentration ratio
d_{air}	Air density (kg/m^3)
E_T	Equation of time
G_{air}	Mass airflow rate based on the absorber area ($kg/(s\ m^2)$)
g	Acceleration due to gravity (9.81 m/s^2)
I_B	Beam solar radiation (W/m^2)
I_D	Diffuse solar radiation (W/m^2)
I_T	Global solar radiation (W/m^2)
k_{air}	Air thermal conductivity (W/m K)
K_{ext}	Extinction coefficient of the glazing (m^{-1})

L_{col}	Collector length (m)
l_{local}	Local longitude
l_{ST}	Standard longitude
M	Mass (kg)
N_c	Number of glazing covers
N_{obs}	Number of observations
Nu	Nusselt number
Pr	Prandtl number
Q_u	Useful energy rate transferred to the airflow (W)
Ra	Rayleigh number
Re	Reynolds number
S	Solar radiation rate absorbed (W)
t_{LST}	Local standard time
t_{ST}	Solar time
T	Temperature (K)
t	Time (s)
U_L	Overall heat loss coefficient (W/(m^2 K))
U	Internal energy (J)
v	Air velocity (m/s)
W	Width (m)
X_{exp}	Experimental or observed value of the variable X
X_{in}	Barley moisture content at the dryer's inlet (in dry base)
X_{out}	Barley moisture content at the dryer's outlet (in dry base)
X_{sim}	Simulated of predicted value of the variable X
H	Height (m)
h	Heat transfer coefficient (W/(m^{2}K))
R	Thermal resistance (K/W)

Greek

α	Absorptivity
β_{th}	Volume expansion coefficient of the air (K^{-1})
Δt	Time step (s)
η_o	Optical efficiency
η_{th}	Thermal efficiency

γ_{col}	Collector's azimuth angle
γ_{s}	Solar azimuth angle
ν_{air}	Air kinematic viscosity (m^2/s)
δ	Thickness (m)
ℓ	Hole pitch (m)
Γ	Fraction of total solar radiation accepted
φ_{h}	Hole size (m)
φ_{p}	Absorber porosity
σ	Stefan-Boltzmann constant (5.67 x 10^{-8} W/(m^2 K^4))
τ	Transmissivity
ε	Infra-red emissivity
ε_{eff}	Effective emissivity
ξ	Mean absolute error

Subscripts

abs	Absorber
amb	Ambient
apt	Aperture
avg	Average
bar	Barley grains
C1	Convection from absorber to glazing
C2	Convection from glazing to ambient
glaz	Glazing
h	Hole
HX	Convection from absorber to airflow
in	Air at the inlet
out	Air at the outlet
R1	Radiation from absorber to glazing
R2	Radiation from glazing to ambient
TS	Tertiary section
v	Vaporization point
w	Wind

TABLE OF CONTENTS

LIST OF FIGURES

LIST OF TABLES

CHAPTER 1

INTRODUCTION

To achieve the carbon emission target, high fraction of locally available renewable energy sources will become necessary to reduce energy demand. Solar energy is one of the most important renewable sources for use in building heating, cooling, hot water supply and power production. Solar thermal systems for water and air heating are well established technologies. Their use promotes environmental sustainability, as it eliminates the need to provide heat by combusting of fossil fuels therefore contributing to reducing greenhouse gases emissions. Building integrated solar thermal systems (BISTS) can be a potential solution towards the enhanced energy efficiency and reduced operational cost in contemporary built environment. According to the vision plan issued by European Solar Thermal Technology Platform (ESTTP), by 2030 up to 50% of the low and medium temperature heat will be delivered through solar thermal systems (European Solar Thermal Technology Platform, 2009).

Solar air heating collectors transfer solar thermal energy from an absorbing surface to an airflow. The heated air can be used for applications, such as space heating, timber seasoning, curing of industrial products and food drying (Shams et al., 2016), as can be seen in Table 1.1 with the corresponding air temperature range. A solar air heater can integrate to a concentrator to produce air at medium or high temperatures (Duffie and Beckman, 2013). A concentrating collector combining inverted absorber and asymmetric compound parabolic concentrator (IACPC), in which solar radiation is reflected to be incident from below onto the absorbing surface, has been proposed by Rabl (1976b). Although there are optical losses due to the multiple reflections of incident solar energy

(Kothdiwala et al., 1996), this type of concentrator is able to achieve higher absorber temperatures by suppressing convective and radiative heat losses (Kothdiwala et al., 1999). A competing technology for this application is on evacuated tube collectors (ETC). This also has optical losses due to reflection from the tubular aperture. An ETC's low heat losses arise from a vacuum between the glass tube envelope and an absorber. As well as limiting long-term durability, this is challenging to fabricate and to envelope the large cross-section duct required for airflow.

Table 1.1: Application for air heating and operating air temperature range. From Norton (2012) and Pranesh et al. (2019)

Application	Temperature range (^{o}C)
Timber drying	60 – 100
Food drying	30 – 90
Brick curing	60 – 140
Space heating	30 – 100

An IACPC was designed to be used as a solar air heater collector by Shams (2013). This collector had a perforated absorber surface made of carbon fibre placed at a fixed cavity height, a glazed aperture, a concentration ratio of 2.0, and was optically characterised and experimentally tested at different airflow rates. In this design, the air inlet was located at one end below the absorber and the outlet was placed at the top near the other end. The lowest experimental airflow rate (0.03 kg/(m^2.s)) resulted in the highest temperature rise of 38 ^{o}C at a radiation level of 1000 W/m^2. The highest experimental operating flow rate (0.09 kg/(m^2.s)) resulted in a temperature rise of 19.6 ^{o}C at a radiation level of 1000 W/m^2.

This current research designed IACPC collectors to be stacked on a wall. The collector had a vertical aperture so that shading could be avoided when two or more collectors are stacked on a vertical wall, enabling the full façade area available to be harnessed (as shown in Figure 1.1. The concentration ratio was increased to receive more solar radiation. However, solar air heating systems comprising more than one interconnected IACPC collector have not been thermal characterised to date. The number of collectors needed to meet air temperature requirement for specified conditions is not known nor is the cost involved. The behaviour of the airflow and the heat transfer mechanism inside the collector have never been studied in sufficient detail to enable detailed parametric analysis. Such understanding will allow designers to propose improvements to the system. Based on the scale and size of the collector developed, the system has the potential application for pre-heating fresh air for buildings.

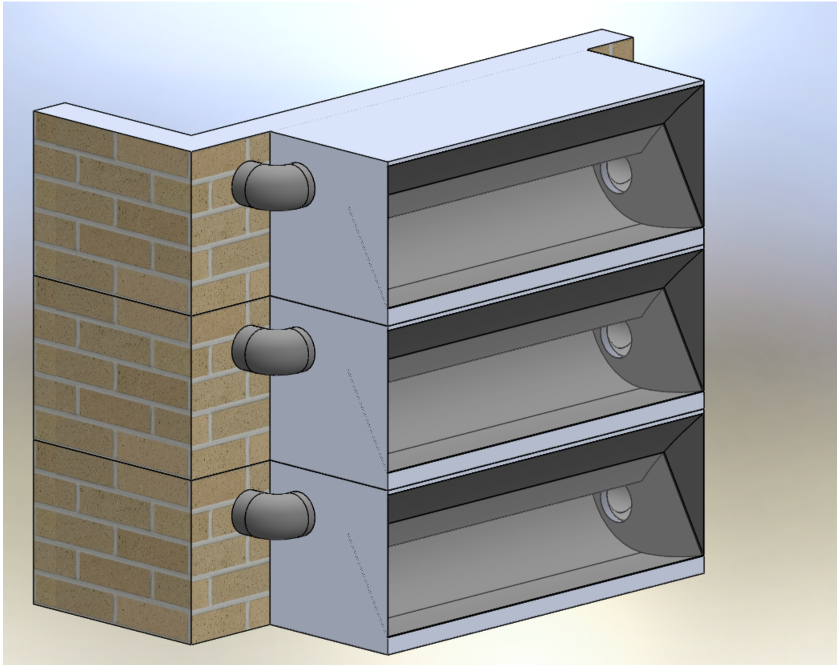

Figure 1.1: Array of 3 collectors stacked on a 1-m^2 wall of facade.

1.1 Aim and objectives of this research

This research aims to design and characterise an asymmetric compound parabolic air heating solar collector with an inverted transpired heating absorber. The intended application constraint is a building integrated air heating system comprising several collectors capable of collecting solar radiation for eight hours per day in summer to heat an airflow. An array of 3 collectors is shown in Figure 1.1. The specific objectives are to:

- ✓ develop a mathematical model to build the collector's shape;
- ✓ use this model to assess the optical performance with a ray tracing technique in 3D and thus decide the design of the collector;
- ✓ fabricate a prototype and undertake field tests for the collector characterisation to

achieve a well understanding of the operational variables that affect its performance;

✓ simulate the collector's thermal behaviour through a transient heat transfer modelling and validate it using the experimental results obtained from the prototype unit;

✓ simulate the thermal performance of more than one collector connected in series and in parallel from the validated model;

✓ simulate a barley drying as an application to the solar collector system based on the energy demand.

1.2 Significant new knowledge to the research area

The significant new contribution to knowledge in the research area of solar thermal energy for air heating are:

✓ development of an accurate model capable of bulding the shape of CPCs, ACPCs and coupled with inverted absorbers. It considers design parameters, such as parabolic shape, concentration ratio, truncation, length, inclination and absorber position;

✓ coupling of this model to a 3D ray tracing technique that simulates direct solar radiation using solar angles (azimuth and altitude) from the Sun's position;

✓ additional results obtained from an optical modelling in 3D when compared to the modelling in 2D, such as end losses and energy distribution along the absorber area;

✓ thermal modelling and simulation of more than one collector connected in series and in parallel to deliver higher airflow temperatures or more useful energy rate;

✓ use of the thermal modelling to simulate barley drying application to find how much energy can be replaced by the solar air heating system.

1.3 Thesis overview

The research methodology is shown in Figure 1.2. The Thesis overview with the chapters is depicted as follows:

✓ Chapter 1 introduces the research topic, research motivation and establishes the problem statement. The main aims of the research, specific objectives and methodology

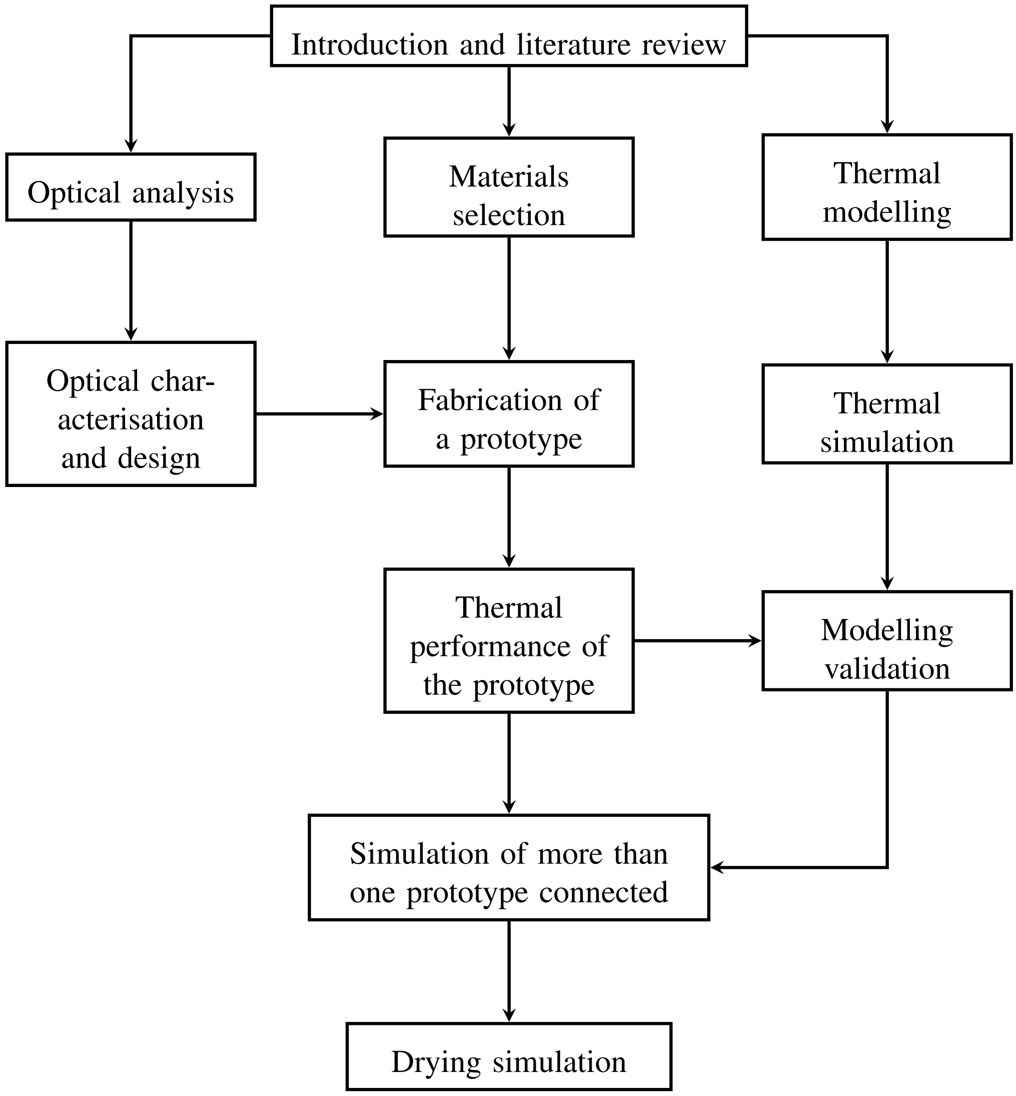

Figure 1.2: Research methodology.

used are presented here;

✓ Chapter 2 – Literature review: it presents a literature survey that identifies the state-of-the-art of solar thermal collectors for medium temperatures applications with a focus on the main factors that affect the thermal performance. This chapter also presents the optical aspects of a CPC and how an optical analysis can be performed. Optical concentrator designs were examined to identify possible ways to concentrate solar radiation on to an inverted absorber. Lastly, it shows an overview building integrated solar thermal collectors;

✓ Chapter 3 – Optical modelling and design analysis: presents the design of the solar air heating concentrator as well as the development of a model to calculate optical efficiency. It also depicts details of the concentrator's geometric specification. A 3D ray tracing technique implemented in Matlab software were developed to calculate the energy distribution at the absorber surface and the effect of the end plates on the optical performance;

- ✓ Chapter 4 – Experimental performance analysis: it describes physical properties of the materials, fabrication and experimental characterisation of the built collector prototype at different airflow rates. The performance of the system depends on wind speed, solar radiation, inlet air and ambient temperatures;
- ✓ Chapter 5 – Heat transfer modelling and simulation: depicts the heat transfer model developed to characterise and simulate the thermal performance of the proposed solar air heater in operation. This model was used to calculate the outlet airflow temperature and thermal efficiency and experimental data was used to validate the model. Then the model was used to simulate the thermal performance of collectors connected in series and in parallel. Lastly, the validated model was used as an energy input for simulating barley drying to meet the energy demand for an application.
- ✓ Chapter 6 – Conclusions: it summarises the main conclusions, presents the contributions to knowledge in the field and then proposes recommendations for future work.

CHAPTER 2

LITERATURE REVIEW

This chapter depicts the concept and characteristics of solar air heating collectors – unglazed and glazed collectors. Considerations will be given to:

✓ Elements and factors to affect collector's performance;

✓ Optical concentrator, specifically ACPC with inverted absorber;

✓ Building integration of solar thermal systems.

2.1 Solar air heating collectors

Solar air heating collectors (SAHCs) are equipment designed to receive solar radiation and convert it into heat for working air heating. They are widely applied in many commercial applications, such as hot air supply to shopping malls, agricultural barns, industrial drying, etc. They are usually low cost, with no freezing and high pressure problems. Compared to water heating solar collectors, SAHCs are outperformed due to the air thermal properties (Buker and Riffat, 2015). To overcome this challenge, the heat transfer from the hot absorber surface of the collector to the air needs to be enhanced while the collector's overall heat losses are minimised. (Shams, 2013).

SAHCs can be classified into two main types: unglazed and glazed. The basic difference between these types is the presence of a glazing cover and the shape of the absorber surface. Unglazed air heating collectors (also known as Unglazed Transpired Solar Collectors – UTSCs) do not have glazing cover and are composed of a perforated (transpired) absorber plate, as shown in Figure 2.1(a). The absorber plate is usually a metallic plate (steel or aluminium), which can be integrated into building façades. The contact between absorber plate and ambient air is increased by drawing air through the multiple perforations into the cavity (also called plenum) between the plate and the façade (Shukla et al., 2012). This heated air in the plenum is pulled into the building by a fan (Buker and Riffat, 2015).

The other main type is the glazed SAHC (or Glazed Air Heating Collector – GAHC), which has at least a flat glazing cover to prevent the absorber from being exposed to the ambient and avoiding efficiency losses. A common design can be seen in Figure 2.1(b). The air is pulled into the collector by a fan to be heated after contact to the absorber plate, which can have different shapes and/or other modifications to enhance the transfer mechanism.

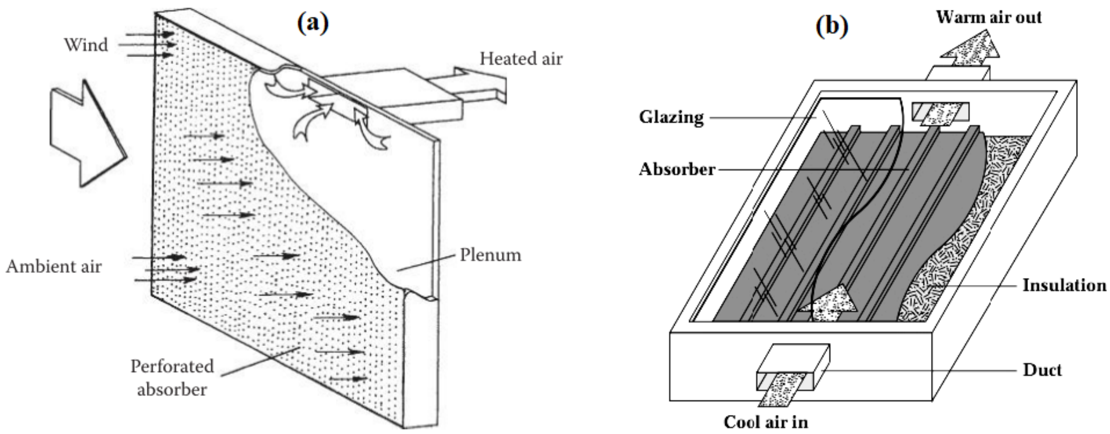

Figure 2.1: Illustration of (a) an unglazed and (b) a glazed solar air heating collector. From Kutscher (1994) and Solar Tribune (2011).

To improve the heat transfer from the hot absorber surface to the working air, a wide range of designs for SAHCs has been studied and reported in the literature: glazed, unglazed, bare plate, back-pass, perforated, un-perforated, single, double or triple passes, etc. (Kutscher, 1994; Christensen et al., 1997; Gawlik et al., 2005; Koyuncu, 2006; Leon and Kumar, 2007; Tchinda, 2008; El-Sebaii and Al-Snani, 2010; Athienitis et al., 2011; Zheng et al., 2016; Li et al., 2016).

2.1.1 Energy analysis

To understand how SAHCs' thermal performance is improved, it is worthy defining the response variables to quantify that. It is common to define the thermal efficiency as the ratio of useful energy rate to the incoming total solar radiation I_T received on the aperture area A_{apt}, calculated by Eq. (2.1). Such efficiency can be evaluated either instantaneously or as an average over a certain period of time (Goswami, 2015):

$$\eta_{th} = \frac{Q_u}{I_T A_{apt}} \tag{2.1}$$

where the useful energy rate can be calculated considering the airflow rate m_{air}, the temperature difference between outlet and inlet, and the air specific heat at constant pressure:

$$Q_u = m_{air} C_{p,air} (T_{out} - T_{in}) \tag{2.2}$$

The thermal characterisation of a SAHC relates the thermal efficiency under steady state to each temperature rise normalised by the corresponding solar radiation according to the Hottel-Whillier-Bliss equation, expressed by Eq. (2.3).

$$\eta_{th} = \eta_o - U_L \frac{(T_{abs} - T_{amb})}{I_T} \tag{2.3}$$

where U_L is the collector's overall heat loss coefficient. The U_L value depends weakly on temperature and, in most cases, it is considered to be constant at typical operating conditions (Rabl, 1985). Lastly, the optical efficiency η_o is defined as the ratio between the absorbed and the incident solar radiation. From this equation, η_{th} can be plotted against $(T_{abs} - T_{amb})/I_T$, resulting in a linear curve, with η_o and U_L as the linear coefficient and the slope, respectively (Goswami, 2015).

It is usual to calculate the efficiency based on the air temperature, as it is more practical to measure it rather than the temperature of the absorber surface. Particularly the air temperatures T_{in} and T_{in} at the inlet and outlet of the collector, respectively. Eq. (2.3) can be rewritten by adding a multiplicative term known as the heat removal factor (in Heat Transfer textbooks it is also known as heat exchange effectiveness). It is defined as the ratio of the heat transferred to the airflow to the maximum possible heat transfer, if the outlet air temperature was heated to the absorber surface temperature (Kutscher, 1994). This effectiveness is calculated as:

$$\varepsilon_{HX} = \frac{T_{out} - T_{in}}{T_{abs} - T_{in}} \tag{2.4}$$

This effectiveness can also be written as function of the airflow rate and the convective heat transfer coefficient (h_{HX}):

$$\varepsilon_{HX} = 1 - \exp\left(-\frac{h_{HX} A_{abs}}{m_{air} C_{p,air}}\right) \tag{2.5}$$

where this convective coefficient takes into account the heat transfer mechanism between the airflow and the hot absorber plate. It is related to the Nusselt number, which it is the ratio of convective to conductive heat transfer (Incropera et al., 2006). This is calculated by Eq. (2.6):

$$Nu = \frac{L_c}{k_{air}} h_{HX} \tag{2.6}$$

where L_c is the characteristic length associated to the heat transfer and k_{air} is the air thermal conductivity. The Nusselt number is usually a function of the Reynolds number, which is proportional to the air velocity. Therefore, to enhance the heat transfer, it is desirable to operate a solar collector with higher airflow rates. In addition to that, there are many other factor that influence the heat transfer mechanism. The next section describes the elements of a SAHC and how they influence its thermal performance. These elements are absorber plate, glazing cover, air flow rate and system modifications.

2.1.2 Effect of absorber surface

The absorber surfaces of SAHCs are usually metal plates. As the airflow to be heated goes through the perforated absorber surface, the heat transfer mechanism between the holes and the air is more effective compared to flat plate collectors. The absorber design considers the following factors: i) material and coatings; ii) shape; iii) thickness of the absorber; and iv) modified area.

2.1.2.1 Absorber material and coatings

It was previously assumed that a collector's high performance was consequence of high thermal conductive materials. This assumption was based that a significant portion of the thermal energy was transferred to the airflow. Plus, it would considerably rise the average surface temperature and, consequently, increase the radiative heat loss to the ambient (Gawlik and Kutscher, 2002; Gawlik et al., 2005).

Christensen et al. (1997) compared experimentally the thermal performance of an UTSC for two absorber materials: aluminium (k = 216 W/(m K)) and styrene plastic (k = 0.16 W/(m K)), where both surfaces had the same geometry. Results show that the UTSC's efficiency is relatively insensitive to low thermal conductivity materials. It means that there is sufficient thermal energy from the absorber surface to the air so that high thermal conductivity materials is not as critical as previously assumed.

Arulanandam et al. (1999) simulated an UTSC's thermal performance in CFD, under no wind conditions, varying the absorber's thermal conductivity from 0.196 to 15.121 W/(m K)). They concluded that, for low porosity plates, the heat exchange effectiveness dropped by 10 – 20% but the thermal efficiency only decreased by approximately 5%.

The temperature distribution along the absorber surface can vary for low conductive materials. The local convective heat transfer is higher in regions of higher surface temperature and lower in regions of lower surface temperature. This effect is reduced if the hole pitch is small so that a large temperature gradient is not achieved. Gawlik et al. (2005) showed that the effect of material conductivity on the thermal performance is small. The study then concluded that low thermal conductivity materials can be used with no thermal efficieny penalty but a great benefit in cost savings and corrosion resistance.

One or both of the front and back surfaces of the absorber may be dark colour to absorb solar radiation. Surfaces may be treated or coated to have a low emittance of infra-red radiation so that heat losses are reduced. The effect of the radiative properties absorptivity and emissivity has also been reported. Leon and Kumar (2007) simulated an UTSC varying the values of both properties and found out that the absorptivity has a stronger effect on the thermal efficiency than the emissivity. El-Sebaii and Al-Snani (2010) simulated a single pass GAHC comparing absorber surfaces using different coatings. They concluded that the highest daily efficiency was achieved using nickel–tin (absorptivity and emissivity of 0.98 and 0.14). Compared to a black painted galvanized iron absorber (0.88 of absorptivity and emissivity), the nickel-tin coated absorber outperformed by 29.23%. Li et al. (2016) simulated a glazed TSC and found that painting the absorber plate with a selective coating of higher absorptivity and lower emissivity would enhance the heat transfer mechanism from absorber plate to plenum and reduce the radiative losses from the absorber surface to the glazing cover. The effect of coating absorptivity on the thermal efficiency is more considerable than that of emissivity.

2.1.2.2 Effect of porosity, perforation diameter and pitch

The plate posority for flat plates is defined as the ratio of perforation area to the total surface area. It can only be calculated by setting values of perforation diameter and pitch. Smaller perforation diameters tend to strengthen the jet impingement and thus increase the heat transfer mechanism (Li et al. (2016)). The pitch (or perforation spacing) has a stronger influence on heat exchange effectiveness than on thermal efficiency. With larger pitches, hot spots tend to develop on regions of the absorber surface which are away from the perforations (Arulanandam et al. (1999)). However, if the distance between the holes is small enough, this effect can be avoided.

Kutscher (1994) investigated the effect of increasing perforation diameter (1.6 mm to 3.2 mm) and pitch (13.5 mm to 27 mm) and verified that the heat exchange effectiveness decreased. Arulanandam et al. (1999) found out that the Nusselt number was increased in a range of plate porosity from 0.5% to 2%. Decker et al. (2001) simulated an UTSC and found that the heat exchange effectiveness decreased with increasing pitch (7 mm to 24 mm) and perforation diameter (0.8 mm to 3.6 mm). They also concluded that 28% of the air temperature rise occurs in holes of the perforated plate. Gawlik et al. (2005) tested two plates of different porosities (0.3% and 5%) and concluded that there was no significant difference in terms of air temperature rise because the perforation diameter was increased and the pitch was decreased by the same proportion.

According to Leon and Kumar (2007), simulation results showed that the airflow temperature rise and heat exchange effectiveness increased with decreasing pitch and perforation diameter. For a constant solar radiation and airflow rate, changing the pitch from 12 to 24 mm with a corresponding change in perforation diameter from 0.8 mm to 1.55 mm resulted in a drop of 5.5 ^{o}C in the airflow temperature rise. Furthermore, for a particular pitch, any change in hole diameter affected the effectiveness only moderately; when the porosity was increased, the effectiveness and the thermal efficiency marginally decreased.

2.1.2.3 Effect of absorber thickness

The effect of the absorber surface thickness is insignificant to the thermal effectiveness when it is thin (smaller than 1.5 mm) (Kutscher, 1994). However, for thick absorbers (between 1.6 and 3.6 mm), the heat transfer varies between different perforation area, thus affecting the collector's thermal performance. Zomorodian and Zamanian (2012) tested UTSCs with two different absorber plate thicknesses and concluded that the thicker was more efficient.

2.1.2.4 Effect of the absorber modified area

One way of enhancing the heat transfer from the absorber to the airflow is introducing obstacles in the air stream to increase the absorber surface area. These obstacles can be fixed either to the internal face of the absorber or on the back plate or as a combination. The objective of using these obstacles is to increase the outlet air temperature, as well as the efficiency with minimum losses (Karsli, 2007). Modifications of the absorber area include using finned, wavy or V-corrugated shapes, as seen in Figure 2.2.

Karim and Hawlader (2004) studied and compared three types of GAHCs: flat plate, finned and V-corrugated to achieve an efficient design suitable for a solar dryer. They found that the V-corrugated collector is the most efficient collector and the flat plate one the least. Results show that the V-corrugated collector has 7—12% higher efficiency than flat plate collectors. Kurtbas and Durmus (2004) also studied different absorber geometries and concluded that all GAHCs outperform the flat plate collector. Karsli (2007)

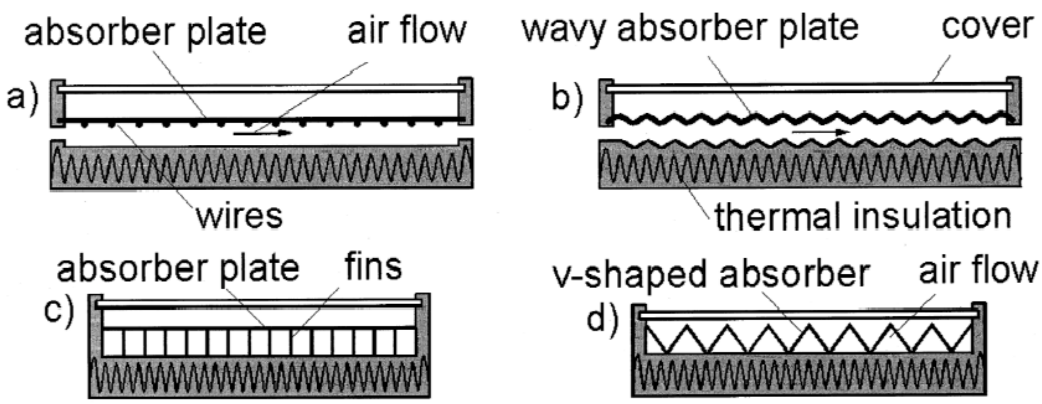

Figure 2.2: Illustration of GAHCs with different absorber area: (a) wired, (b) wavy, (c) finned, and (d) V-shaped (or V-corrugated). From Pottler et al. (1999).

compared the thermal performance of finned absorber collector to a flat plate one with no fins and concluded that the finned GAHC is more efficient than the flat plate. This is because the fins create turbulent flow and it leads to a higher heat transfer coefficient, lowering the absorber temperature and reducing the thermal heat loss at the same time. Alta et al. (2010) compared a GAHC with flat absorber surface to one with finned absorber and concluded that attaching fins on that surface increases the thermal efficiency. Assari et al. (2011) developed a mathematical model based on effectiveness method for assessing the thermal performance of a GAHC, where water and air flow simultaneously. Three different types of channels were used to enhance the collector's performance: rectangular fin, triangular fin (V-corruated) and without fin. Simulation results show that channels with rectangular fin had the best performance. El-Sebaii et al. (2011) compared the thermal peformance of a flat plate collector to a V-corrugated collector. The results showed that the double pass V-corrugated plate collector is 11 – 14% more efficient compared to the double pass flat plate collector.

2.1.3 Effect of glazing cover

A glazing cover plays an important role to suppress convective heat losses from the absorber plate to the ambient and also protect the solar collector against weather conditions. It also needs to have high transmissivity to the solar spectrum and extensively opaque to long (or infrared) wavelength radiation emitted by the absorber (Saxena et al., 2015). In other words, a glazing cover is used to reduce convective and radiative heat losses while transmits most of the incoming solar radiation (Norton, 2006).

Glazing materials commonly used are glass, plastic and fibreglass, where the challenge is to find a material with high transmissivity, low thermal conductivity, being affordable and have the required mechanical properties for building integrated systems. Glass is considered as a glazing cover because it is transparent for the solar range and it absorbs almost all the infrared radiation re-emitted by the absorber plate. This results in an enhancement of the collector's thermal efficiency by creating a greenhouse effect (Khoukhi and Maruyama, 2006).

To minimize the heat losses from the collector, more than one glazing cover may be used (El-Sebaii and Al-Snani, 2010; Yeh and Ho, 2009). However, the transmissivity then decreases due to the increased number of reflections (Michalopoulos and Massouros, 1994). Alta et al. (2010) conducted an experimental study comparing single and double glazed flat plate collector with finned absorber. The authors stated that the double glazed collector performed better, also showing higher air temperature difference.

Reflection losses at the glazing surface depend on the refractive index of the cover material and structural orientation of the glazing. The lowest reflection losses can be achieved if an antireflective coating with a refractive index between the air and the cover material is used. Investigations have shown that the glass transmittance and solar collector efficiency can be increased by 4% if an antireflection coating is applied instead of a normal glass as the cover plate for the solar collector (Furbo and Shah, 2003).

Glass is also very resistant to scratching, high operating temperatures and practically impervious to the damaging effects of ultraviolet exposure. The incident sunlight transmitted through glass depends on the iron content of the glass, between 85% to 92%, at normal incidence. While low iron content increases the transmittance of glass, low iron glass is more expensive. Glass can be easily broken, but this can be minimized by using tempered glass which adds a further additional cost (Duffie and Beckman, 2013).

Transparent plastics, such as polycarbonates, polyethylene and acrylics have also been used as glazing materials (Koyuncu, 2006). Their main advantages are resistance to breakage and light weight, and are cheaper than glasses. The main disadvantages of plastics are high transmittance in the longer wavelength, and deterioration over a period of time due to ultraviolet solar radiation (Goswami, 2015; Duffie and Beckman, 2013). Additionally, plastics are generally limited in the temperatures they can sustain without deteriorating or undergoing dimensional changes. Although glass is an expensive option when considering 20 years collector life span, this is the best option as the glazing material (Shams, 2013).

2.1.4 Effect of airflow rate

The flow rate is the most important factors in the thermal performance of a solar collector. Effect of that have been extensively studied. Experimental and simulation results show that when the flow rate is increased, more useful heat is collected, overall losses are reduced, thus increasing the collector's thermal efficiency. On the other side, the outlet temperature and the heat exchange effectiveness are decreased (Christensen et al., 1997; Ammari, 2003; Leon and Kumar, 2007; El-Sebaii and Al-Snani, 2010; Zomorodian and Zamanian, 2012; Li et al., 2016). A typical relationship between air temperature rise, thermal efficiency and flow rate is shown in Figure 2.3.

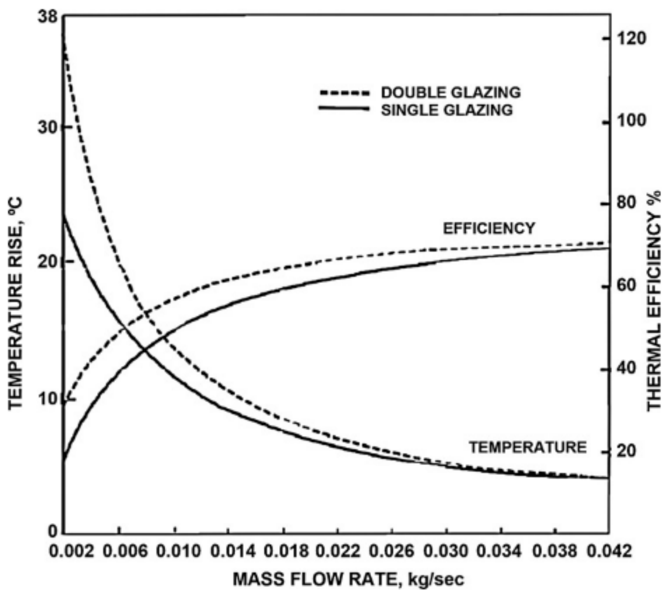

Figure 2.3: Graphs of air temperature rise and thermal efficiency against mass flow rate at the steady state. From Tyagi et al. (2012).

Ammari (2003) simulated a single pass GAHC and found that the thermal efficiency increased fast until a certain level of volumetric flow rate and then it increased moderately. A decreasing pattern could be observed for the air temperature as the flow rate was increased. Leon and Kumar (2007) simulated an UTSC and observed that the rate of decrease in energy rate is lower at lower approach velocities. They also concluded that the collector efficiency decreases with increasing outlet air temperatures. Jafarkazemi and Ahmadifard (2013) simulated a flat plate collector and also observed that the overall heat loss coefficient dropped as the mass flow rate increased. Badache et al. (2014) and Nowzari et al. (2015) analyzed different factors that affect both UTSC and GAHC performances and concluded that the airflow rate had the strongest influence on the thermal efficiency. Li et al. (2016) evaluated the performance of a GAHC with a perforated absorber taking into account the fan power required to overcome air flow resistance through collector. In this case, higher airflow rates lead to higher useful heat collected but also higher fan power required. Results show that there is a level of airflow rate to be operated that maximised the energy efficiency.

2.1.5 System modification

This topics depicts the influence of the air flow passing through the collector in contact to the absorber, the parameterization of the channel dimension through which the air flows, and the manner in which multiple collectors are connected (series or parallel).

2.1.5.1 Air passage through the collector

In literature, considerations are given to the contact of the airflow to the absorber plate (or PV module for electricity generation) when the former passes through the collector. It is named single pass collector when the airflow comes in contact absorber only once. Alternatively, it is named double pass when air flows in contact to the absorber twice, as shown in Figure 2.4.

Hegazy (2000) simulated a photovoltaic/thermal (PV/T) glazed collector using different modes: air flowing over or below the absorber, and even on both sides in a single or in a double pass. He found out that flowing air on both sides leads to the best perfor-

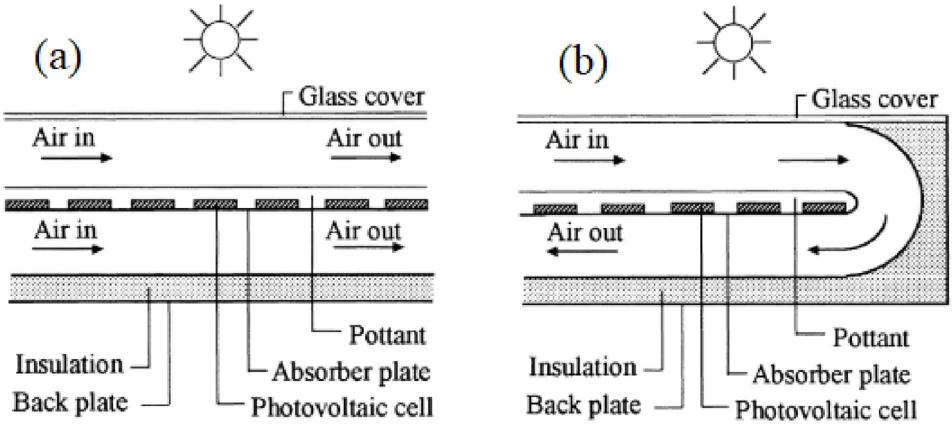

Figure 2.4: Illustration of (a) single pass and (b) double pass air heating collector. From Hegazy (2000).

mance, considering both applications. Yousef and Adam (2008) tested single and double pass GAHCs and concluded that double pass achieved higher thermal efficiency and outlet air temperature. Nowzari et al. (2015) investigated a single and double pass GAHC and concluded that the higher efficiencies are achieved using double pass mode. Karim and Hawlader (2004) investigated collectors with different absorber configurations and from the efficiency tests in double pass operation, it is concluded that the efficiency of all collectors increases in double pass mode.

The effect of external recycle on the GHAC thermal efficiency has been investigated. It was found that considerable improvement in collector's thermal performance is obtained if it is operated with an external recycle, where the desirable effect overcomes the drawbacks. The performance is enhanced with increasing reflux ratio, especially for operating at lower air flow rate with higher inlet air temperature (Yeh and Ho, 2009).

2.1.5.2 Channel's dimensions

Hegazy (1999) showed a criterion for determining the channel optimum depth-to-length ratio which maximizes the useful energy from GAHCs to operate at fixed mass rate of air flow. He also observed that decreasing the depth or increasing the length improves the thermal performance. Tonui and Tripanagnostopoulos (2007) studied a photovoltaic/thermal glazed collector where forced air was used to extract heat from the back of the PV module through a channel. They evaluated the effect of the channel depth (distance between the PV module and the collector's bottom) and the length on the thermal performance at constant airflow rate. It was verified that the thermal efficiency and air outlet temperature reduced with increasing channel depth. They also concluded that the thermal efficiency increased with increasing channel length and approaches constant value as the length increases. The same pattern was verified by Yousef and Adam (2008) when they investigated the thermal performance of a single pass GAHC where forced air was pumped above the absorber plate. They also concluded that air temperature and efficiency decreased with increasing channel depth at constant airflow rate. Tonui and Tripanagnostopoulos (2008) simulated a photovoltaic/thermal glazed collector using natural convection to aleviate the PV module temperature and found out that there is an optimum channel depth that maximises the thermal efficiency.

2.1.5.3 Connection of collectors

Solar collector arrays can be connected in series or parallel, each with different thermal performance outcomes. In a series connection system, the total heat transfer of the collectors is higher since the total airflow passes through all collectors. However, the temperature rise in the collectors reduces the thermal efficiency of each progressive collector, and the power consumption to pump the airflow is also higher (Hastings, 2000). A schematic of multiple units in connection is shown in Figure 2.5. Oonk et al. (1979) developed a formula to predict the performance of N collectors in series by deriving the exit temperature of one collector and using it as the inlet temperature of the next collector. Fanney and Thomas (1981) also developed an equation to predict the thermal performance of collector arrays, both in series and parallel, based on energy balance.

2.2 Concentrating collectors

When it is required to warm the airflow to higher temperatures with high thermal performance, concentrators can be employed to meet the objective. The working principle is to receive solar radiation through a larger area and direct that, using reflectors, to a smaller absorber area. There are different types of concentrating collectors, depicted as

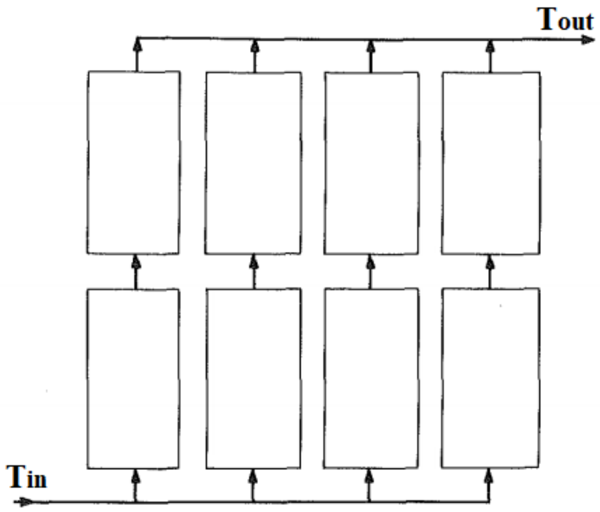

Figure 2.5: Schematics of a system with collectors in series and in parallel. From Fanney and Thomas (1981).

follows (Evangelisti et al., 2019):

✓ Parabolic trough collector (PTC): it consists of a parabolic reflector and an absorber placed along the whole length of the concentrator at the parabola's focus. PTCs generally track the sun using east-west, north-south, or polar orientations. The absorber is usually tubular, enclosed in a glass tube to reduce radiative and convective losses (Goswami, 2015). The solar radiation is reflected torwards the tube, bringing it to high temperatures and heating the heat-transfer fluid that flows inside the tube. The absorber temperature varies between 50 °C and 300 °C, but it can also reach 400 °C;

✓ Compound parabolic concentrator (CPC): It is designed from two distinct parabolic segments, where the focus of each one is located at the opposing absorber surface end points. The axes of the parabolic segments are oriented away from the CPC axis by the acceptance angle θ_{a}. The slope of the reflector surfaces at the aperture is parallel to the optical axis for untruncated CPCs;

✓ Heliostat field collector: it is composed by flat reflectors placed all around a central receiver, called solar tower. These reflectors can face the sun through a tracking system. Central receivers can achieve temperatures of the order of 1000 °C or even higher. Therefore, a heliostat collector is suitable for thermal electric power production of 10 – 1000 MW (Goswami, 2015);

✓ Linear Fresnel collector: it is comprised by linear receivers and reflectors. Usually, the reflector segments are aligned horizontally, facing the sun so that the receiver can be hit by the rays without needing movements;

✓ Parabolic dish collector: it is characterized by a paraboloidal geometry able to concentrate solar radiation onto a receiver placed at the focal point of the collector.

2.2.1 Optical analysis

One way of evaluating a concentrator is by characterising its optical performance. The optical efficiency is defined as the ratio between the absorbed and the incident solar radiation. For this analysis, the optical properties of the reflectors, glazing cover and absorber should be taken into consideration, as well as the reflectors' shape and the concentration ratio (Sellami and Mallick, 2013):

$$\eta_{\mathrm{o}} = \tau_{\mathrm{col}}\tau_{\mathrm{g}}\alpha_{\mathrm{abs}} \tag{2.7}$$

where the term τ_{col} takes into account the number of reflections at the reflectors. The reflector's shape and concentration ratio dictate the number of reflections and, therefore, the optical efficiency. The term τ_{g} is the transmissivity of the glazing cover; alternatively, for collector without cover or glass-tube absorbers, this term is unity. Therefore, it is desirable that the concentrator transmits most of the solar radiation through the glazed aperture, has a highly reflective reflector surface and a high absorptivity absorber with low emissivity. Most of these properties have been discussed in the previous section of this Chapter.

Other factors are taken into consideration: i) incoming solar radiation and its components; ii) the position of the Sun at a specific location and what direction the concentrator is facing at a set inclination; iii) the optics in the glazing cover, and; iv) the effect of truncation. Other factors such as the parabolic shape of a CPC collector and concentration ratio will be further investigated in other section.

2.2.1.1 Solar radiation and intercept factor

The total solar radiation (I_T) incident on the concentrator's aperture is the sum of the beam (I_B) and diffuse (I_D) components. However, since only part of the diffuse radiation is exploitable by concentrators, the factor Γ must be defined, as being the fraction of total solar radiation accepted. Assuming that the angular distribution of diffuse radiation is isotropic, this factor can be estimated as (Rabl et al., 1980):

$$\Gamma = \frac{\left(I_B + \frac{I_D}{C}\right)}{I_T} \tag{2.8}$$

and therefore the incoming solar radiation available to reach the absorber surface is assumed to be $I_T\Gamma$. Since CPC collectors operate in the concentration ratio range of 2 to 10 to capitalize on the corresponding reduced tracking requirement, from one-half to one-tenth of the incident diffuse radiation is accepted (Goswami, 2015).

It is important to highlight other angular distributions of the diffuse insolation that can affect the performance of a PTC and CPC collectors. Two other particular distributions can be considered: cosine, and hybrid Gaussian. The hybrid Gaussian distribution combines an isotropic background with a circumsolar Gaussian part. This distribution is more realistic for a tracking system than both the isotropic model (which underestimates the insolation intensities at incidence angles near zero) and the cosine model (which underestimates the intensities at large incidence angles). The analytical expressions for the three distributions considered have been presented by Prapas et al. (1987). However, on clear days (diffuse radiation is approximately 11% of total radiation), the difference in optical efficiency between the three distributions of diffuse radiation is not significant.

2.2.1.2 Collector's inclination and orientation

It is important to establish the position of the collector's aperture considering its inclination in relation to the horizontal plane, and the Sun's position as function of the day, time and location. Figure 2.6 shows a basic scheme of the Sun's position by the altitude (a_S) and azimuth (γ_S) solar angles, as well as the inclination β and the collector azimuth angle γ_w. The latter defines the orientation of the collector: if $\gamma_w = 0$, the collector is south-facing.

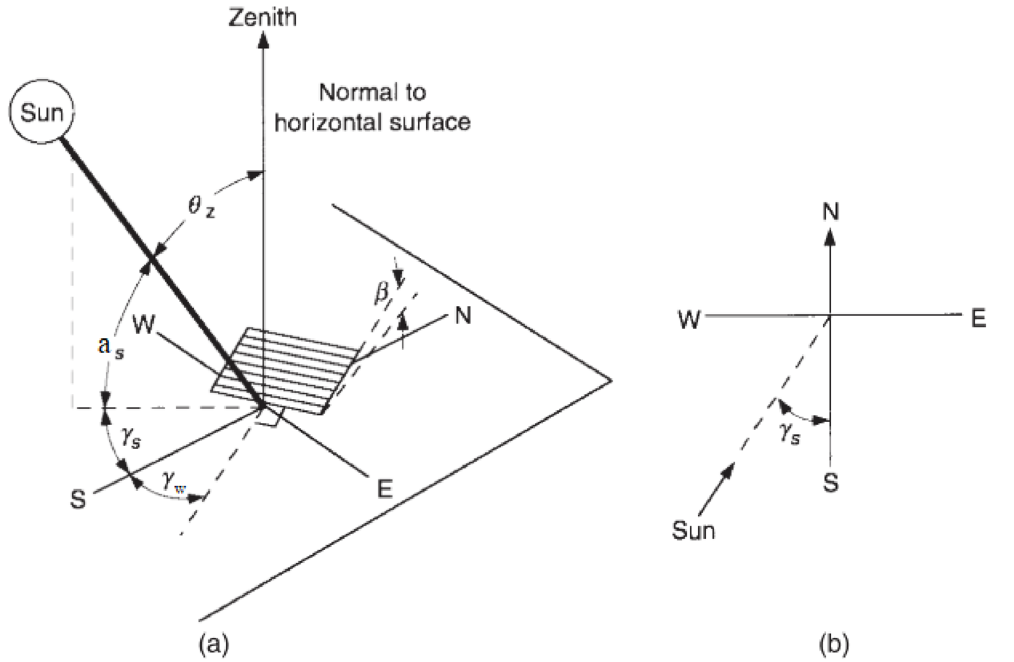

Figure 2.6: (a) Altitude solar angle, surface azimuth angle, and solar azimuth angle for an inclined surface. (b) Plan view showing solar azimuth angle. Adapted from Duffie and Beckman (2013).

The incident angle θ_i, defined as the angle between the incident solar ray and the normal to the glazing, is calculated by Eq. (2.9):

$$\theta_i = \cos^{-1}\left[\cos a_s \cos(\gamma_s - \gamma_w)\sin\beta + \sin a_s \cos\beta\right] \tag{2.9}$$

Solar hour angles (ω_s) were obtained from the solar time for each day of operation. The solar altitude and solar azimuth angles were calculated from (Duffie and Beckman, 2013):

$$a_s = \sin^{-1}(\sin\phi \sin\delta_s + \cos\phi \cos\delta_s \cos\omega_s) \tag{2.10}$$

$$\gamma_s = \sin^{-1}\left(\frac{\cos\omega_s \sin\delta_s}{\cos a_s}\right) \tag{2.11}$$

where the solar declination δ_s is a function of the year's day and ϕ is the latitude of the location.

Pottler et al. (1999) calculated the total energy collected for a GAHC at north, south, west and east orientations located in the Northern Hemisphere and verified that the south facing orientation collects more energy because it is optically more efficient. Roux (2016) used a ray tracing simulator to calculate the optimum inclination and azimuth angle of a flat plate collector at different locations. Results showed that an optimally positioned collector can, on average, collect 10% more annual solar energy than a horizontally-fixed collector. The optimum fixed inclinaton angle is similar to the latitude of the location and the optimum fixed azimuth angle is a function of the longitude angle minus the absolute latitude angle.

2.2.1.3 Glazing optics

By Snell's law, considering the angle of incidence at the glazing cover, the angle of refraction is calculated by Eq. (2.12):

$$\theta_{\mathrm{r}} = \arcsin\left(\frac{\sin\theta_{\mathrm{i}}}{\mathrm{n_{idx}}}\right) \tag{2.12}$$

where $\mathrm{n_g}$ is the refraction index of the glazing cover that is dependent of the material. When passing through the glazing medium, part of the incident radiation is reflected and absorbed. The term that takes into account the transmissivity related to the reflected radiation alone is given by Eq. (2.13):

$$\tau_{\mathrm{r}} = \frac{1}{2}\left[\frac{1-\mathrm{r_{par}}}{1+(2\mathrm{N_c}-1)\mathrm{r_{par}}} + \frac{1-\mathrm{r_{perp}}}{1+(2\mathrm{N_c}-1)\mathrm{r_{perp}}}\right] \tag{2.13}$$

where N is the number of glazing covers, and $\mathrm{r_{par}}$ and $\mathrm{r_{perp}}$ are the terms related to the reflections, functions of the angles of incidence and refraction (Duffie and Beckman, 2013). Similarly, the term that considers the glazing absorptivity τ_{a} is given by Eq. (2.14):

$$\tau_{\mathrm{a}} = \exp\left(-\frac{\mathrm{K_{ext}}\delta_{\mathrm{glaz}}}{\cos\theta_{\mathrm{r}}}\right) \tag{2.14}$$

where δ_{glaz} is the glazing thickness and $\mathrm{K_{ext}}$ is the extinction coefficient which is a function of the material: for glass, the value of this coefficient varies from approximately 4 $\mathrm{m^{-1}}$ for "water white" glass to nearly 32 $\mathrm{m^{-1}}$ for high iron oxide content (greenish cast of edge) glass. Lastly the glazing transmissivity τ_g can be approximated by the product of the glazing absorptivity and the standalone transmissivity as a function of the glazing material and the incidence angle:

$$\tau_{glaz} \cong \tau_r \tau_a \tag{2.15}$$

2.2.1.4 End losses

If a linear concentrator is long in an east-west orientation compared to its width and height, it can be assumed to behave as a two dimensional system where end effects are negligible (Eames and Norton, 1993b). For concentrators with short axial lengths, the end losses need to be included on the optical analysis as a portion of reflected solar rays may not reach the absorber under certain obtuse solar incident angles. To take into account the end losses, the opical efficiency is multiplied by a factor for that pupose, which is a function of the incidence angle and the collector's geometry. This factor has been analytically calculated for imaging parabolic troughs (Rabl, 1985) and for linear Fresnel concentrators. End losses have stronger influence at high latitude locations and it could cause the absorber to be completely in shadow in winter days (Hongn et al., 2015). Pu and Xia (2011) estimated the end-effect for the north-south and east-west linear Fresnel collectors analyzing the angles between incident solar rays and the tacking axes of the reflectors. They concluded that the end losses can be compensated by increasing the length of the mirror field. Heimsath et al. (2014) quantified optical losses of Fresnel collectors and proposed a corrective end loss factor for end loss modeling. They also observed that the optical losses are higher for wider zenith angles and shorter collectors. Xu et al. (2014) presented an optical analysis and compensation method for the end loss effect of parabolic trough solar collectors with horizontal north-south axis. The calculation formulae for optical end loss ratio and increased optical efficiency are derived, and various factors affecting them are analyzed. The compensation method is found to be applicable for regions with latitudes over 25^{o} and short trough collectors.

2.2.1.5 Truncation

Compared to a simple parabola a CPC is very deep, and therein lies its main disadvantage; it requires a rather large reflector area for a given aperture area. For example, for a concentration ratio of 10, the ratio reflector area to aperture area is approximately 11, while a PTC has the ratio around 1.2. To overcome this drawback, a large portion of the top of a CPC can be cut off with almost no loss in performance. In practical applications, a CPC will amost always be truncated, for economic reasons (Rabl, 1976b). Carvalho et al. (1985) derived analytic expressions of angular acceptance range and evaluated the yearly collectable energy as function of the extent of truncation. Truncated concentrators accept solar rays at broader incident angles, thus collecting more solar energy due to reduction of reflections. Francesconi and Antonelli (2018) simulated a five-CPC assembly's performance in CFD; they concluded that a concentration ratio reduction from 2.0 to 1.96 resulted in a 2% increase of the system's thermal efficiency.

2.2.2 The Compound Parabolic Concentrator (CPC) family

This section depicts the geometry of a symmetric CPC, assymetric CPC and a modification to include an inverted absorber.

2.2.2.1 Symmetric CPC

The compound parabolic concentrator (CPC) is a non-imaging solar concentrator that has the advantages (compared to focusing ones) of i) there being no need for solar tracking, and ii) the ability to collect a portion of diffuse radiation (Winston, 1974). The CPC has been used for heating and PV electricity production (Jaaz et al., 2017). A typical CPC cross section is shown in Figure 2.7. Solar radiation accepted within the angular acceptance range is focused onto an absorber by reflection at the two symmetrical parabolic reflectors.

One of the geometric parameters of a CPC is the geometrical concentration ratio, which is the ratio of the aperture to the absorber areas. This parameter has an upper limit calculated by Eq. (2.16):

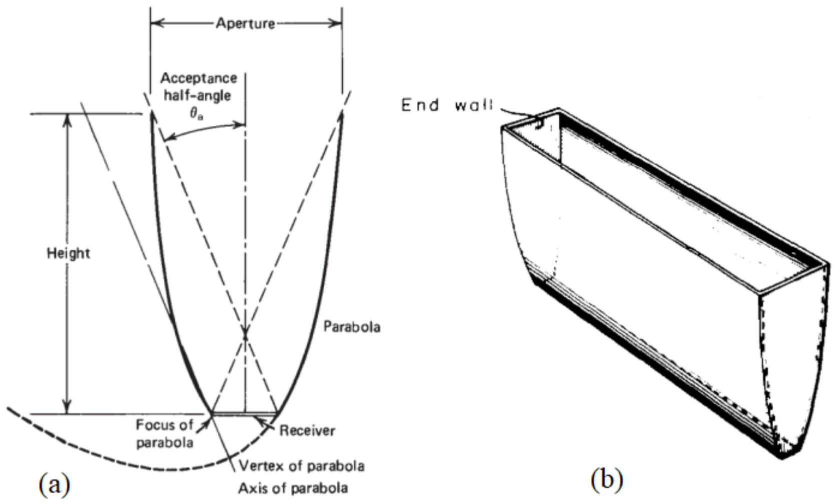

Figure 2.7: Basic CPC with flat plate absorber: (a) cross section design in 2D and (b) in 3D. From Duffie and Beckman (2013) and Winston (1974).

$$\mathrm{CR} = \frac{1}{\sin\theta_{\mathrm{a}}} \tag{2.16}$$

where the half-acceptance angle θ_a is the angular limit over which radiation is fully accepted without moving all or part of the concentrator (Rabl, 1976a). If the reflectors are specular, all the solar rays incident at angles within the acceptance range (between $\pm\theta_a$) reach the absorber surface. Figure 2.8 shows the untruncated and truncated versions of the same CPC. The effect of truncation on the design parameters concentration ratio, height-aperture width ratio (H_{CPC}/W_{apt}) and reflector length has been presented by graphs and equations (McIntire, 1979; Rabl, 1976b). Figure 2.9 shows the angular acceptance function for an untruncated (full) CPC and for a truncated configuration.

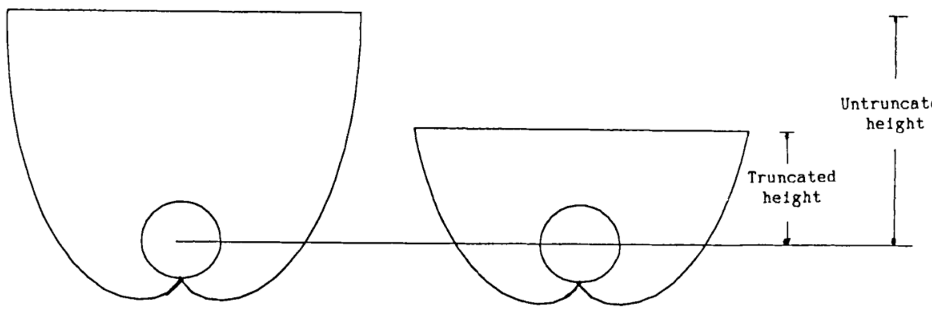

Figure 2.8: Truncated and untruncated CPC with tubular absorber. From Norton et al. (1991)

The shape of reflectors affects size, angular acceptance range (Zacharopoulos et

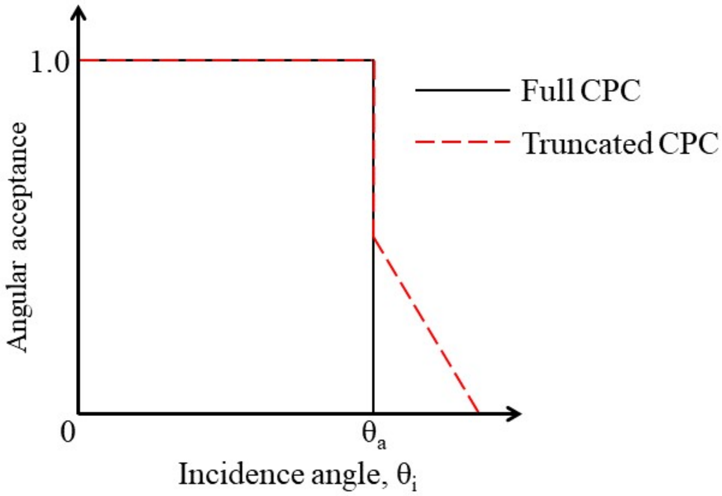

Figure 2.9: Angular acceptance function of a full and truncated CPC. Adapted from Norton et al. (1991).

al., 2000; Harmim et al., 2012) and maximum geometric concentration ratio (Mills and Giutronich, 1978). Given the same level of concentration ratio, concentrators of narrow angular acceptance are more efficient so collect higher amounts of the available solar energy (Sarmah et al., 2011; Kostić and Pavlović, 2012).

The CPC has been extensively studied and reported in the literature. A common case of study considered a CPC where a working fluid passes within the absorber to capture the heat. However, the cavity between the absorber and the glazing cover is filled with dead air, and therefore, convective losses occur due to the temperature gradient. This has effect in the motion of air, known as natural or free convection. Hence, this free convective heat transfer coefficient h_f is calculated as:

$$h_f = \frac{k_{air}}{L_c} Nu_f = a(Ra)^b \tag{2.17}$$

where the parameters a and b depend on the geometry and the flow regime (Cengel and Turner, 2004). The Rayleigh number is defined as the product of the Grashoff and the Prandtl numbers, shown by Eq. (2.18):

$$Ra = Gr\,Pr = \frac{g\beta_{th}}{\nu_{air}^2} L_c^3 \Delta T^* \, Pr \tag{2.18}$$

where: L_c is the characteristic length; the volume expansion coefficient β_{th} is $1/T_{air}$ as the air is considered an ideal gas; ΔT^* is the temperature difference between the surface and the air; and ν_{air} is the air kinematic viscosity.

Abdel-Khalik et al. (1978) evalutated the natural convective coefficients between absorber surface and cover plate for vertically oriented two-dimensional CPC using finite-element techniques. Values of the critical Rayleigh number for different concentration rc atios ($2 < CR < 10$) with three levels of truncated CPCs are determined. Results show that convection is suppressed in high-concentration cavities where the height/aperture ratio is large.

Prapas et al. (1987) developed a heat transfer model and found out that the Nusselt number is affected by the concentration ratio of the collector, its inclination and the absorber temperature. The average Nusselt number rises as the inclination of the collector increases, and this effect is enhanced for higher concentration ratios. Moreover, generalised correlations for the variation of Nusselt number have been obtained.

Eames and Norton (1993a) performed a detailed parametric analysis of heat transfer in untruncated CPCs using a model for their optical and thermal behaviour. The effects of inclination and acceptance angles on free convection within the cavity were studied. A convective heat transfer correlation is obtained for the average Nusselt number with respect to Grashof number that takes into account acceptance angle and angular inclination. They also observed that CPCs of higher acceptance angles have lower Nusselt numbers.

A theoretical and experimental investigation into the modifications in optical and thermal performance resulting from the introduction of a baffle into the cavity of a CPC has been performed. Results shown that the introduction of a baffle reduces internal convection thereby reducing heat losses with small reduction in optical efficiency (Eames and Norton, 1995).

A heat transfer modelling in CPCs has been investigated. This considered the effect of the inclination angle of an east-west aligned collector. The internal and external convective heat transfer correlations employed are angular dependent. The model also considered the contribution of beam and diffuse radiation. The results demonstrate that there is a 10% variation in convective heat transfer with angle of inclination for low concentration CPCs (i.e. CR = 1.5). Furthermore, the thermal efficiency was lower for incoming radiation of more diffuse component. In this case, because of the high diffuse radiation, a CPC of lower concentration would be preferred to maximise the fraction of the diffuse insolation collected. (Kothdiwala et al., 1995).

The results show that when radiation is neglected the onset of fluid motion is delayed by the level of concentration of the cavity. When radiation is considered, it has an important effect on the temperature distribution inside the parabolic cavities, as well as the local and average values of the convective and radiative Nusselt numbers. The emissivity has a strong effect on the average radiative Nusselt number especially at high Rayleigh numbers (Diaz and Winston, 2008).

Tchinda (2008) developed a mathematical model for computing the thermal performance of an SAHC with truncated CPC having a flat one-sided absorber. The effects of the air mass flow rate, the wind speed and the collector length on the thermal performance of the present collector were investigated. Predictions for the performance of the SAHC also exhibit reasonable agreement, with experimental data with an average error of 7%.

2.2.2.2 Asymmetric CPC

Symmetric CPCs have two equal half acceptance angles in relation to the optical axis. The asymmetric compound parabolic concentrator (ACPC) introduced by Rabl (1976b), a particular case of its symmetric counterpart. Figure 2.10 shows a general cross section of an ACPC, where the acceptance angle is $2\theta_{\mathrm{a}} = \alpha_{\mathrm{PU}} + \alpha_{\mathrm{PL}}$. The geometric concentration ratio is also the ratio of the aperture to absorber areas. The axis of the upper (lower) parabola subtends an angle $\alpha_{\mathrm{PU}}(\alpha_{\mathrm{PL}})$ with the normal of absorber. Therefore, broader angular acceptance range and designs with higher concentration ratios can be achieved due to the asymmetry (Tian et al., 2018).

Asymmetric concentrator systems present the following advantages (Mills and Giutronich, 1978):

✓ Ability to compensate lower solar radiations in early morning and late afternoon, allowing more uniform output;

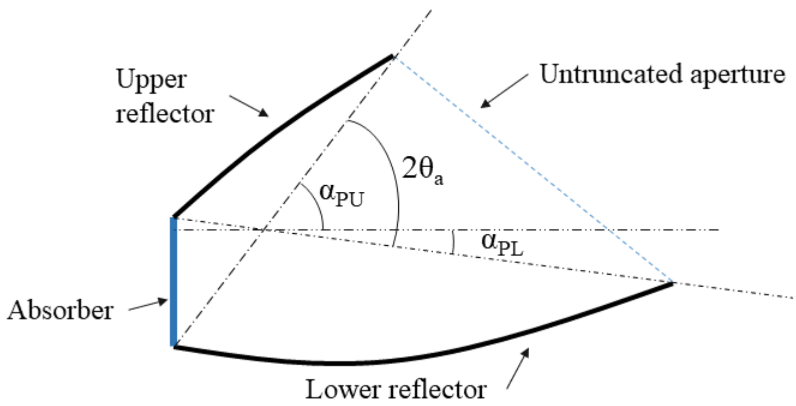

Figure 2.10: General design of an asymmetric CPC.

✓ Greater operational flexibility for unexpected variations in energy demand and higher yearly average energy input per reflector surface area.

Researchers have studied this type of concentrator in detail. Zacharopoulos et al. (2000) analysed the optical performance of a 3D dielectric ACPC with a 78% truncation at the vertical compared to a symmetric version (Figure 2.11). The analysis showed that the asymmetric concentrator design is more suitable for use in a building facade compared to a symmetric one. Using a dielectric concentrator, an ACPC can collect 40% of solar radiation with, due to refraction, collection even outside the angular acceptance range. Tripanagnostopoulos et al. (2000) proposed a collector design based on a truncated asymmetric CPC reflector, consisting of a parabolic and a circular part. This design features a flat bifacial absorber installed at the upper part of the collector, parallel to the glazing to form a thermal trap space between the reverse absorber surface and the circular part of the mirror. The experimental results showed that the proposed collector could achieve a maximum efficiency of 71% and a stagnation temperature of 180 ^{o}C. Mallick et al. (2006) presented a comparative experimental characterisation of a non-imaging line-axis 0 – 50^{o} acceptance-half angles asymmetric compound parabolic photovoltaic concentrator (ACPPVC-50) suitable for vertical building facade integration with its non-concentrating counterpart. Mallick et al. (2007) performed an optical and heat transfer analysis for a truncated ACPC of concentration ratio 2.01 suitable for photovoltaic applications with the aim of using airflow to alleviate temperature at the solar cells. Sarmah et al. (2011) compared the optical performance of three dielectric ACPC designs (all truncated with concentration ratio of 2.82) of acceptance angles 0 – 55°, 0 – 66°, and 0 – 77°, in order to optimize the concentrator for building facade photovoltaic applications in northern latitudes (> 55 °N). Based on the annual solar energy collection by all the designs, it was found that the system of acceptance angles 0 – 55° is more optically efficient and can collect more energy compared to the other two. Harmim et al. (2012) constructed and evaluated the performance of a box-type solar cooker equipped with an ACPC of concentration ratio 2.12. The reflectors were designed so that the absorber could receive solar rays at solar altitude angle was between 30 and 75°.

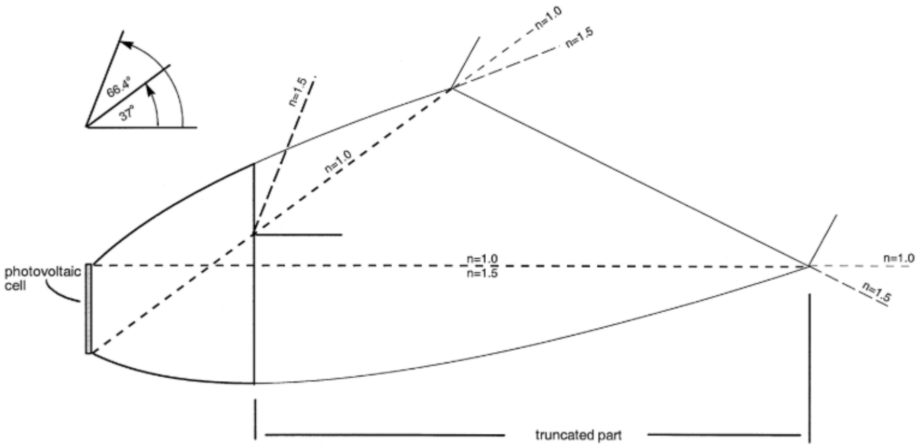

Figure 2.11: Dielectric ACPC with 78% truncated at the vertical for building integration photovoltaic.

2.2.2.3 ACPC with Inverted Absorber

Collectors employing inverted absorber, in which solar radiation is reflected from below onto the downward-facing absorbing surface, have been proposed by Rabl (1976b) and shown in Figure 2.12. They are also called inverted absorber asymmetric compound parabolic concentrator (IACPC). Although optically less efficient due to the multiple reflections of incident solar energy (Eames et al., 1996; Kothdiwala et al., 1996; Shams, 2013), this type of concentrator is able to achieve higher absorber temperatures by suppressing convective and radiative heat losses (Kothdiwala et al., 1997; Kothdiwala et al., 1999). This is due to the formation of thermally stratified air layers below the absorber, and also because this surface does not view the aperture directly (Kienzlen et al., 1988; Eames et al., 2001).

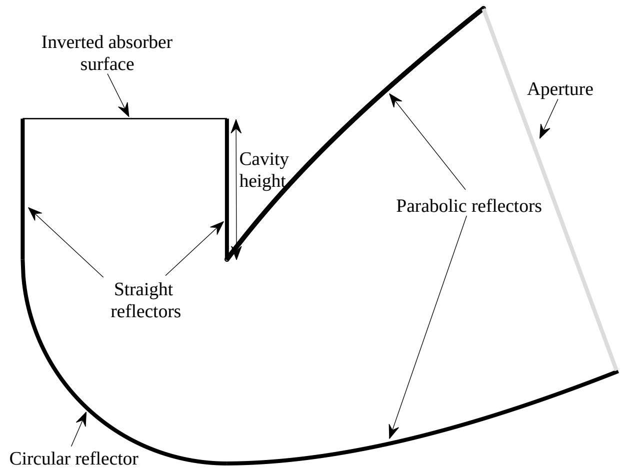

Figure 2.12: Basic CPC geometry with inverted absorber.

Kothdiwala et al. (1996) developed a ray trace model to simulate and optimise the IACPC optical performance. This model considered the effect of beam and diffuse radiation separately. They verified that the beam optical efficiency decreases with the increase of the cavity height and concentration ratio.

Eames et al. (1996) predicted the thermo-physical performance of the IACPC system. In their study, the energy flux at the absorber was determined by a ray trace technique and a finite element model was developed to predict the system's thermo-fluid behaviour. Kothdiwala et al. (1997) conducted indoor experiments under a solar simulator to analyse the performance of the IACPC, which was copper sheeting onto a tubing along the concentrator's long axis. The tests were carried out using water as the flowing fluid at various cavity heights. Kothdiwala et al. (1999) compared a tubular absorber CPC with glass envelope to an IACPC at different cavity heights, both for water heating purposes. They concluded that the appropriate use of an absorber configuration on the IACPC maximises convection suppression and minimises optical losses. Furthermore, at the optimum configuration, this system outperforms the other compared in this study. Eames et al. (2001) simulated the performance of an IACPC by using a combined ray trace and finite element computational fluid dynamics model previously developed by Eames and Norton (1993b). This model was validated by direct comparison with experimental results.

Tiwari and Suneja (1998) modelled and evaluated the performance of an inverted absorber solar still for distillation purpose. They found that this inverted configuration provided double the hourly yield compared to a conventional still. The experimental comparison between an inverted absorber solar still and conventional single slope solar at various water depths has been conducted by Dev et al. (2011). They found that the water temperature in the basin of an inverted absorber solar still is higher than the conventional one.

In order to suppress convection losses, Smyth et al. (2005) investigated the use of transparent baffles at different locations within the collector cavity; the system consisted of an integrated collector storage solar water heater (ICSSWH) mounted in the cavity of an IACPC. Shams et al. (2016) designed and fabricated a concentrating transpired air heating system comprised by an IACPC with a perforated absorber. This collector had the transpired absorber surface made of woven carbon fibre placed at a fixed cavity height, a glazed aperture, a concentration ratio of 2.0, and was experimentally tested at different air flow rates.

2.2.3 Optical systems and Ray tracing technique

A major part of the design and analysis of concentrating collectors involves ray tracing techniques, which are algorithms to simulate sunlight rays passing through an optical system. Ray tracing analysis is an important method adopted in optical systems to obtain the optical performance for complex geometries regarding direct and diffuse solar radiation (Ali et al., 2013). When a ray hits a real reflecting surface, most part of its energy will be reflected. To formulate a suitable ray tracing procedure, the law of reflection can be applied into vector form (Winston et al., 2005). Figure 2.13 shows the unit vectors r_{inc} and r_{ref} along the incident and reflected rays and a unit vector r_n at the normal point of incidence into the reflecting surface. The law of reflection is expressed by Eq. (2.19):

$$r_{ref} = r_{inc} - 2(r_n \cdot r_{inc})r_n \tag{2.19}$$

The ray tracing analysis with optical study can provide:

✓ Average number of reflections before the incoming rays reach the absorber plate

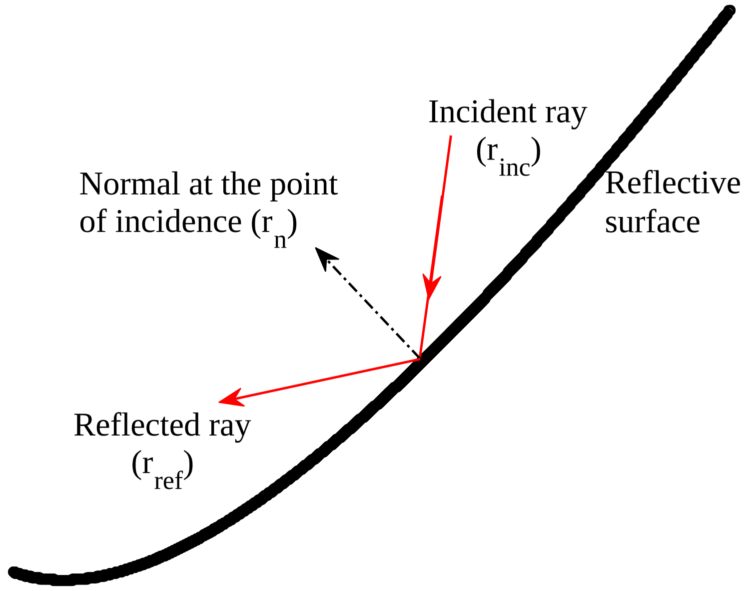

Figure 2.13: Law of reflection applied on a reflecting surface.

(Shams, 2013; Benrejeb et al., 2016);

- ✓ Optical efficiency as a function of the incidence angle (Kothdiwala et al., 1996; Souliotis et al., 2011);
- ✓ Visualisation of rays' path and reflection points (Mallick and Eames, 2007; Ratismith et al., 2014; Ustaoglu et al., 2016);
- ✓ Intensity of energy distributed at the absorber surface (Smyth et al., 1999; Sellami and Mallick, 2013; Ali et al., 2014; Bellos et al., 2016);
- ✓ System's optical characterisation for thermal modelling and simulation (Mallick and Eames, 2007; Shams, 2013; Bellos et al., 2016);
- ✓ Comparison between two or more systems (Zacharopoulos et al., 2000; Sarmah et al., 2011; Wu, 2009).

Several concentrating system have been proposed and optically analysed for different purposes and reported in literature in details. Souliotis et al. (2011) used a two-dimensional ray tracing method to analyse the optical properties of an asymmetric CPC collector. The process involved tracing the paths of a large number of rays through the system and calculating the acceptance angle. The results showed that the collector achieves optical efficiencies above 75% within its acceptance angle, with efficiency decreasing rapidly outside this range.

Sarmah et al. (2011) presented the design and optical performance evaluation of stationary dielectric asymmetric compound parabolic concentrators using ray tracing methods. The designed concentrators have a geometric concentration ratio of 2.82 and a maximum optical efficiency of 83%. The ray tracing simulations show that all rays within the acceptance half-angle range can be collected without escaping from the concentrator's aperture.

Zheng et al. (2011) presented a new multiple chamber trough solar collector and an optical analysis software was used to simulate the ray tracing of the solar light concentrating system. The study investigated the flat receiver and cylindrical receiver and the relationship between the receiving beam and the incident ray. The simulation results showed the distribution, width, eccentric magnitude of the image, and efficiency of the concentrated light varying with the incident angle. The concentration ability of the system with a flat receiver and a cylindrical receiver was quantitatively analyzed and compared.

Using the OpticsWorks software, Sellami et al. (2012) performed an optical analysis and developed a novel geometry of a 3D static concentrator in form of a square elliptical hyperboloid (SEH) to be integrated in glazing windows or facades for photovoltaic application. The SEH of concentration ratio 4.0 was optically optimised considering different incident angles of the incoming light rays.

Ali et al. (2013) evaluated the optical performance of a static 3D elliptical hyperboloid concentrator using a ray tracing software called Optis. Effective concentration ratio, optical efficiency and geometric parameters were analysed. Furthermore, the geometry was optimised to improve the overall performance.

Binotti et al. (2013) proposed an analytical approach to evaluate the impact of 3D effects on the optical performance of parabolic trough collectors. The approach is an extension of the First-principle OPTical Intercept Calculation (FirstOPTIC) method and was validated against numerical solutions and ray-tracing simulation results. The new approach was applied to case studies to examine the impact of 3D effects on the intercept factor, and a correction was proposed for the approach generally accepted for specularity mirror errors for non-zero incidence angles.

Sellami and Mallick (2013) developed a 3D ray trace code in Matlab to determine the beam optical efficiency and the energy distribution of a 3D crossed CPC (CCPC) for different incident angles. The authors found that this type of CPC is an ideal concentrator for a half-acceptance angle of 30^{o} and concentration ratio of 3.6.

Ali et al. (2014) presented the design and experimental analysis of a 3D solar elliptical hyperboloid concentrator (EHC) for process heat applications. Ray tracing analysis was used to obtain the solar flux distribution on the receiver aperture plane, and the optical efficiency was obtained theoretically using a ray tracing program. The design was optimized before finalizing and experimentally testing the EHC.

Abu-Bakar et al. (2014) proposed a new type of concentrator, known as the rotationally ACPC, for use in building integrated systems for PV applications, where the geometrical concentration gain and the optical concentration gain were evaluated. From the simulations, it has been found that the concentration could produce an optical concentration gain as high as 6.18 when compared with the non-concentrating cell depending on the half-acceptance angle.

Ratismith et al. (2014) proposed non-tracking configurations of solar collector modules which are designed to operate efficiently along the day, for varying incident angles of direct and diffuse radiation. The design criteria for achieving a high intercept factor without tracking throughout the day are emphasized by conducting ray tracing analysis on different trough shapes and absorber plate orientations. Furthermore, the superiority of the flat base collector over the double-parabolic design was demonstrated.

Abdullahi et al. (2015) investigated the optical efficiency of two tubular receivers in a compound parabolic concentrator or a single elliptical receiver. Ray tracing is used to predict the optical efficiency, and the results show that the horizontal configuration outperforms both the single and vertical configurations by up to 15%. Moreover, the horizontally aligned elliptical single tube configuration increases the average daily optical efficiency by 17% compared to the single tube configuration.

Benrejeb et al. (2015) used mathematical equations describing the geometric design of an integrated collector storage system. Therefore, an optical study was given with details to achieve the ray tracing technique results and the energy flux distribution on the absorber surface. Furthermore the optical results was used as inputs in the heat transfer model to simulate the temperature of the water inside the absorber.

Benrejeb et al. (2016) worked on a numerical model based on ray tracing technique to study the effect of truncation on the optical and thermal performances of an integrated collector storage system of solar water heater with asymmetric CPC reflectors. The model can predict both full and truncated CPC systems, and the simulation involves analyzing several parameters such as geometric concentration and half acceptance angle. The effect of truncation on ray trace diagrams and its impact on optical and thermal performances was also studied.

Bellos et al. (2016) performed an optical analysis and optimised the geometry of a CPC with an evacuated tube, where this design is considered to be optimum because all the reflected ray reach the receiver. They also calculated the optical losses at different solar angles. The authors also indicate the need of tracking the collector in order to minimise the incident angle. Qin et al. (2013) designed and optimised the geometry of an aspheric reflecting solar concentrator with the aim of focusing sunlight on a narrow line segment. To do so, they used a particular aspheric equation in three dimensions together with the law of reflection to trace the incident rays.

Ustaoglu et al. (2016) developed an optical analysis on a cylindrical CPC for reducing hot spots on a PV cell caused by non-uniform solar irradiation. Different truncation levels were tested to determine the optimum levels for optical and thermal efficiency. The study analysed average efficiency, incident angle, and annual performance for different absorber surfaces. Heat flux and temperature distribution on the absorber were also evaluated to determine the uniformity of solar illumination.

2.3 Building integration of solar systems

Building integrated solar thermal system (BISTS) is a solar thermal collector integrated to a building to meet local energy requirements. This integration must consider functionality (useful thermal energy, thermal insulation, shading, construction stability) and/or appearance aspects (aesthetics, dimensions, shape, colour of the building). In addition to that, they need to be technically and structurally efficient (Wall et al., 2012; Buker and Riffat, 2015). A few more factors will need to be taken into consideration, such as (COST Office, 2015): i) amount of useful thermal energy collected and and fluid temperature delivered; ii) resistance to weather conditions; iii) light and solar energy characteristics in case of transparent layer; iv) thermal resistance and thermal transmittance characteristics of the construction (overall heat transfer coefficient); v) fire protection, and; vi) noise attenuation.

These systems have been classified across a range of operating characteristics and system features and mounting configurations. The main classification criteria of all solar thermal systems are based on the method of transferring collected solar energy to the application (active or passive), the thermal transfer fluid (air, water, water-glycol, oil, etc.) and the final application for the energy collected (hot water and/or space heating, cooling, process heat or mixed applications). In the passive or active classification, in the first case the thermal transfer fluid flows by natural convection or circulation or no transport at all, and in the second case, pumps or fans are used to circulate the fluid to a point of demand or storage (forced convection or circulation). A number of systems are however hybrids, operating by a combination of natural and forced transport methods. Many façade solar air heaters use thermal buoyancy to induce an air flow through the vertical cavities that can be further augmented with in-line fans (and heating) if necessary.

The BISTS delivers thermal energy to the building but additionally other forms of energy may contribute to the buildings energy balance. For instance daylight comes through a transparent window or façade collector, or PV/T systems will also deliver electrical power which may be used directly by any auxiliary electrical services. Heated air or water can be stored or delivered directly to the point of use. Although the range of applications for thermal energy is extensive, all of the evaluated studies demonstrate that the energy is used to provide one or a combination of the following cases:

Space heating: Thermal energy produced by a BISTS may reduce the space heating load of a building by adding solar gains directly (by a passive window) or indirectly (by transferring heat from the collector via storage to a heating element) into the building;

Air heating and ventilation: Thermal heat may be used also to pre-heat fresh air needed in the building. Air is heated directly or indirectly and to provide space air heating and/or ventilation to the building. In some cases, an auxiliary heating system is used to enhance the heat input because of comfort reasons;

Water heating: Hot water demand in the building is the most popular application. In the majority of water heating BISTS, a customized heat exchanger or integrated proprietary solar water is used to transfer collected heat to a (forced) heat transfer fluid circuit and on to an intermediate thermal store and/or directly to a domestic hot water application;

Cooling and ventilation: In cooling dominated climates, buildings may have an excess of thermal energy, and therefore BISTS can also be a technology to extract heat from a building. There are a number of methods described in providing a cooling (and/or ventilation) effect to a building: shading vital building elements, desiccant linings, induced ventilation through a stack effect and reverse operation of solar collecting elements for night-time radiation cooling.

2.3.1 Building integrated solar thermal collectors for air heating

Air-based BISTs are solar thermal air collectors integrated on roofs and façades. These collectors are characterised by low costs but also by a low efficiency due to the thermal characteristics of the air as a heat transfer fluid. Air has low thermal properties, thus influencing convective heat transfer phenomena. To compensate these limits, large collector areas and ducts are needed. However, these can introduce problems related to costs and roof/façade size. Solar thermal façades that use air can be made by integrating an air gap between the rear surface of the glass covers and the building envelope. In space heating systems, constant air flows are generally provided, thus the outlet air temperature varies during the day in function of the solar radiation variations.

Using water instead of air is effective because of its high thermal capacity and thermal conductivity. Water allows easy storage as it is suitable for direct domestic hot water generation, but it is corrosive. The water-based BIST can be classified into two groups: single-channel and multiple-channel BISTs. The first group has evolved from the passive solar heating mechanism, which often provides solutions for the use of hot water. The second group is characterised by a design with an additional air space between the photovoltaic module and the building envelope.

Roof integrated mini-parabolic solar collector have been studied for building-integrated applications. These systems adopt linear Fresnel reflectors to focus the beam solar radiation on a stationary receiver with the use of mirrors and an active tracking system (ref). The use of concentrating optical system for building integrated solar applications was proposed by Chemisana et al. [25]. The analysis of a stationary wide-angle Fresnel lens with a moving CPC was proposed by the authors. A building integrated mini parabolic thermal collector investigated by Petrakis et al. [26], had a East-West orientation with a slope to receive the sun's rays perpendicularly during the day. A solar micro-concentrator collector is shown in Fig. 11.

Another solution is represented by the ceramic solar collectors, mainly characterised by economic convenience, without absorption attenuation and good integration in buildings. As asserted by Buker and Riffat [23], the raw material for this system is traditional ceramic (porcelain clay, quartz and feldspar). The building integration of these solar collectors was also proposed by Yang et al. [27]. The collectors act both as heat source of the water system, and as balcony railings, with a thermal efficiency equal to 41.7%.

Overhang louvre shading modules, placed horizontally, can incorporate solar collectors. This approach allows an increased number of collectors to be installed as space is freed on the building roof for the installation of additional panels. The various designs of solar louvre thermal collector have been discussed by Abu-Zour et al. [28]. They have proposed a design that used heat pipe technology. Marrero et al. [29] analysed a solar thermal system that exploited building louvre shading devices. They proposed the modification of existing designs. The proposed system was tested under several climatic conditions, showing great potential from both an economic and a renewable energy supply point of view.

CHAPTER 3

OPTICAL MODELLING AND DESIGN ANALYSIS

3.1 Aims and objectives

The aim of this chapter is to define the design of a concentrating collector for an air heating system using ray tracing optical analysis. The specific objectives are to:

✓ Develop a ray tracing technique in 3D and implement the optical model in Matlab®;

✓ Evaluate the effect of the parabolic reflectors and the tertiary cavity geometry on the optical performance;

✓ Assess the impact of the concentrator's length on reflector cost;

✓ Analyse the influence of the glazing inclination on the light transmittance through the glazed aperture;

✓ Characterise the optical profile of a concentrator used for experimental tests.

3.2 Design considerations of the concentrator

3.2.1 Overall assembly

The proposed solar concentrator combines of an inverted absorber with an asymmetric compound parabolic concentrator (ACPC). It comprises: i) two parabolic reflectors; ii) a circular reflector; iii) two straight reflectors; iv) two end reflectors; v) a glazing cover not coincident to the aperture, and; vi) an transpired absorber plate. The entire collector is oriented south. A full drawing and cross-section are shown in Figures 3.1 and 3.2, respectively.

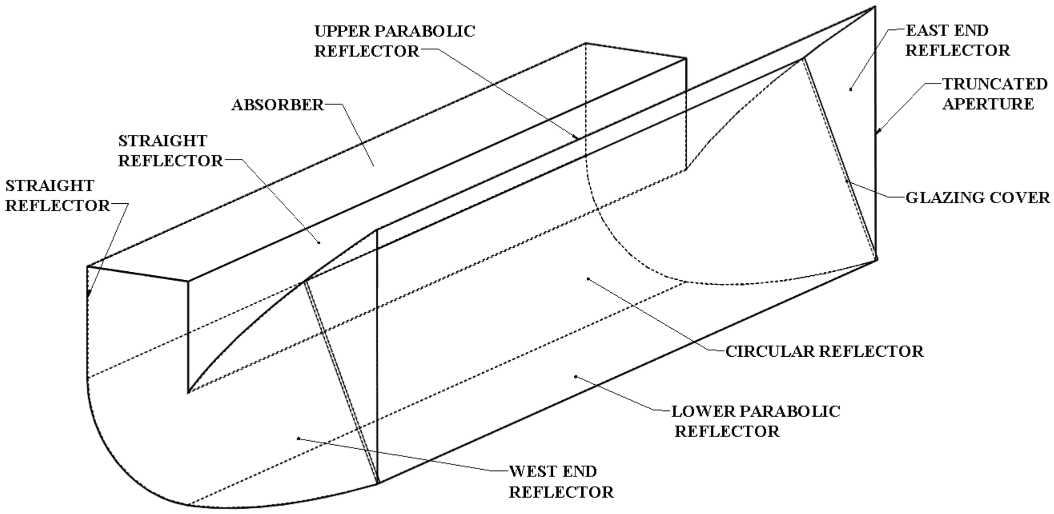

Figure 3.1: Concentrator's design in 3D.

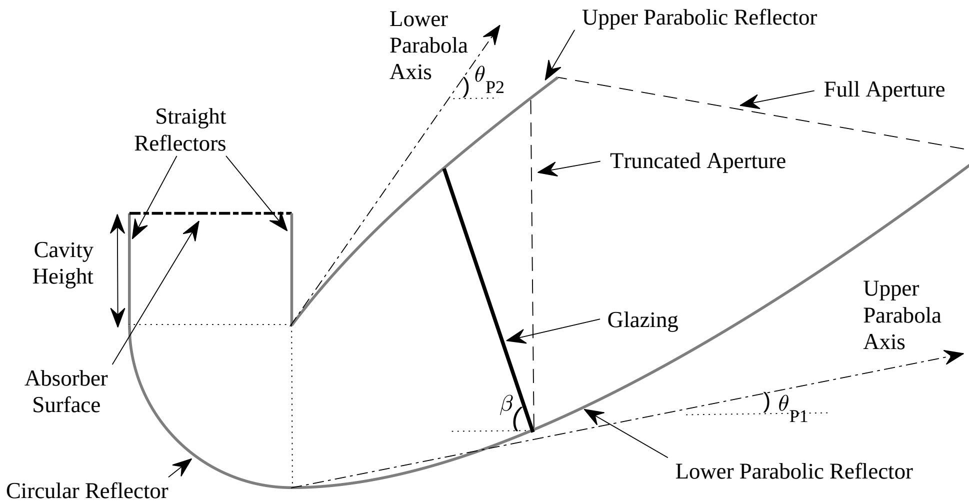

Figure 3.2: Concentrator's cross section view.

3.2.2 Glazing position

The glazing placed from the aperture confines heated air in the collectors, as well as offering protection for the collector interior against weather conditions (Shams et al., 2016). Its position at a given inclination β (shown in Figure 3.2) seeks to gain solar energy transmittance and reduce light reflection.

3.2.3 Aperture position

The concentrator's aperture is set at the vertical position (at the truncation line in Figure 3.2) so that shading can be avoided when two or more collectors are stacked on a vertical wall enabling the full façade area available to be harnessed.

3.2.4 Parabolic shape

The angles of both parabolas axes (θ_{P1} and θ_{P2}) shown in Figure 3.2 define the parabolic shape, therefore affecting size, angular acceptance range (Zacharopoulos et al., 2000; Harmim et al., 2012) and maximum geometric concentration ratio (Mills and Giutronich, 1978). Given the same level of concentration ratio, concentrators of narrow angular acceptance are more efficient so collect higher amounts of the available solar energy (Sarmah et al., 2011).

3.2.5 Cavity height

The cavity contributes to the formation of thermally stratified air layers below the absorber that suppresses convective and radiative heat losses. The height of this cavity affects the distribution of incoming solar radiation along the absorber surface in a way to enhance heat transfer mechanism and mitigate hot spots.

3.3 Operation conditions

This solar air heating system is designed to operate in Dublin, Ireland, where the latitude (ϕ) is 53.35° and the longitude is -6.26° over the summer season (from 21/06 to 21/09) for 8 hours per day, from 9 am to 5 pm (local time).

Defining the operating constraint is an essential prerequisite to calculate the sun angles applicable to the period of operation. They are obtained using solar time (t_{st}), which does not coincide with the local standard time. The relationship between solar and local times, given by Eq. (3.1), is due to the deviation between the local longitude and the chosen meridian on which the local standard time is based.

$$t_{st} = t_{LST} + \frac{4(\ell_{st} - \ell_{local}) + E_T}{60} \quad (3.1)$$

Irregularity of the earth's motion around the sun, accounted by the "Equation of Time" (E_T) as a function of the year's day (Goswami, 2015). Solar hour angles (ω_s) were obtained from the solar time for each day of operation.

A solar position plot of a_s against γ_s at the latitude of Dublin is shown in Figure 3.3, where each graph corresponds to a particular day in the operation period. The values of a_s and γ_s at any point in time in the operation period were used as inputs in the optical modelling. The calculation of these solar angles was verified by Sun calculators available on the Internet (Time and Date, 2018; SunCalc, 2018).

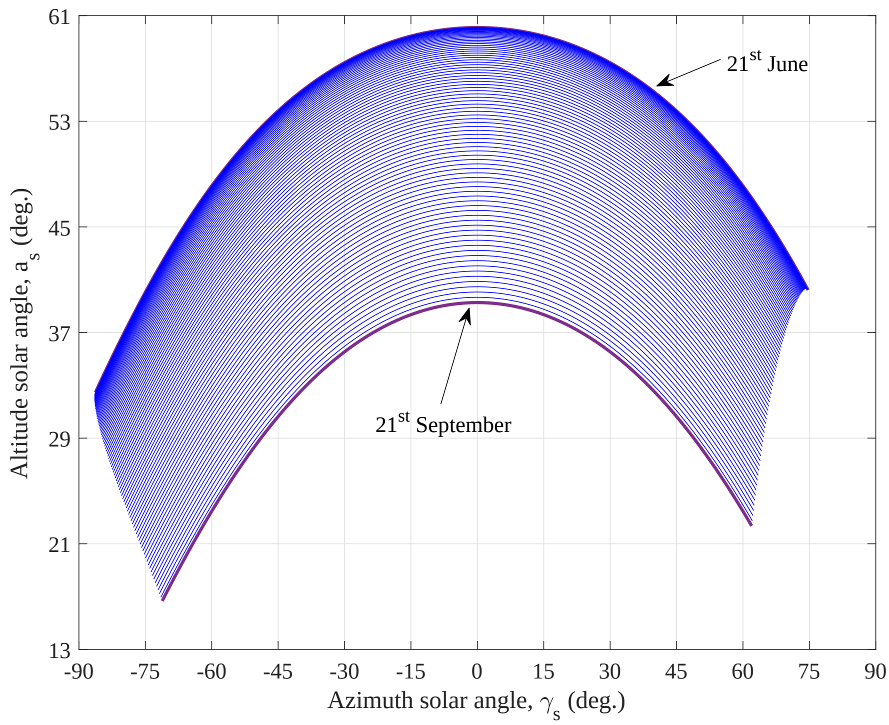

Figure 3.3: Solar position diagram for 53.35° of latitude.

Over the period of operation, the calculated limits of altitude solar angle were 60.1° when the Sun is at its highest altitude, on 21/06 at noon; and 14.6° when the Sun is at its lowest altitude in the last day of summer (21/09) at 9am. The collector must therefore accept direct solar radiation within the solar altitude range, from 15° to 61°.

3.4 Reflector's design specification

3.4.1 Parabolic reflectors design

To design the parabolic reflectors, the first step was to define the equation of the parabola whose axis is coincident to the y-axis with the vertex set at the origin:

$$y_p = \left(\frac{1}{4f}\right) x_p{}^2 \tag{3.2}$$

where f is the focal distance, given by Eq. (3.3) (Winston et al., 2005):

$$f = \frac{W_{abs}}{2}(1 - \cos\theta_a) \tag{3.3}$$

and θ_a is angle related to position of the parabola. The next step was to translate and rotate the parabola to form the parabolic section. Both parabolas were designed and placed at the correct position using basic tools from SolidWorks® as shown in Figure 3.4. The expressions for calculating θ_a, Δx and Δy for each parabola are shown in Table 3.1.

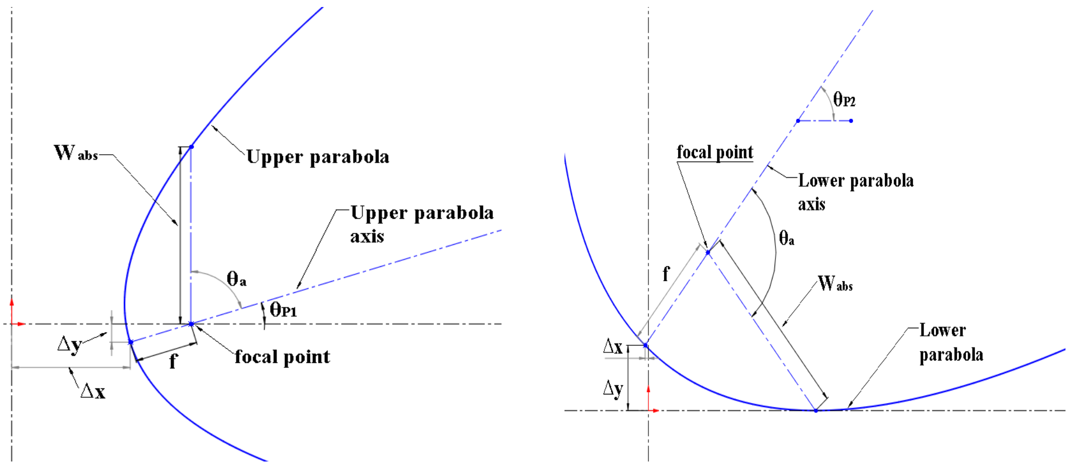

(a) Upper parabola. (b) Lower parabola.

Figure 3.4: (a) Upper and (b) lower parabolas placed at the final position.

The next step was to arrange the parabolas properly in a common coordinate system to form the full untruncated parabolic section shape APQD, shown in Figure 3.5. In this case, point D intercepts the x-axis and the vertical segment length AD is equal the absorber width (W_{abs}), as it is the section end. The full aperture indicated by the segment

Table 3.1: Expressions for the parabolas' parameters.

Parameter	Upper Parabola	Lower Parabola
θ_a	$90-\theta_{P1}$	$2\theta_{P2}$
Δx	$W_{abs}-f\cos\theta_{P1}$	$W_{abs}-(W_{abs}+f)\cos\theta_{P2}$
Δy	$-f\sin\theta_{P1}$	$(W_{abs}-f)\sin\theta_{P2}$

PQ is obtained according to the parabola axes angles. The aperture was set to be vertical, therefore the section is truncated at the line indicated by the segment BC. The curves AB and DC then represent the shapes of the upper and lower reflectors, respectively. Their coordinate limits are given in Table 3.2.

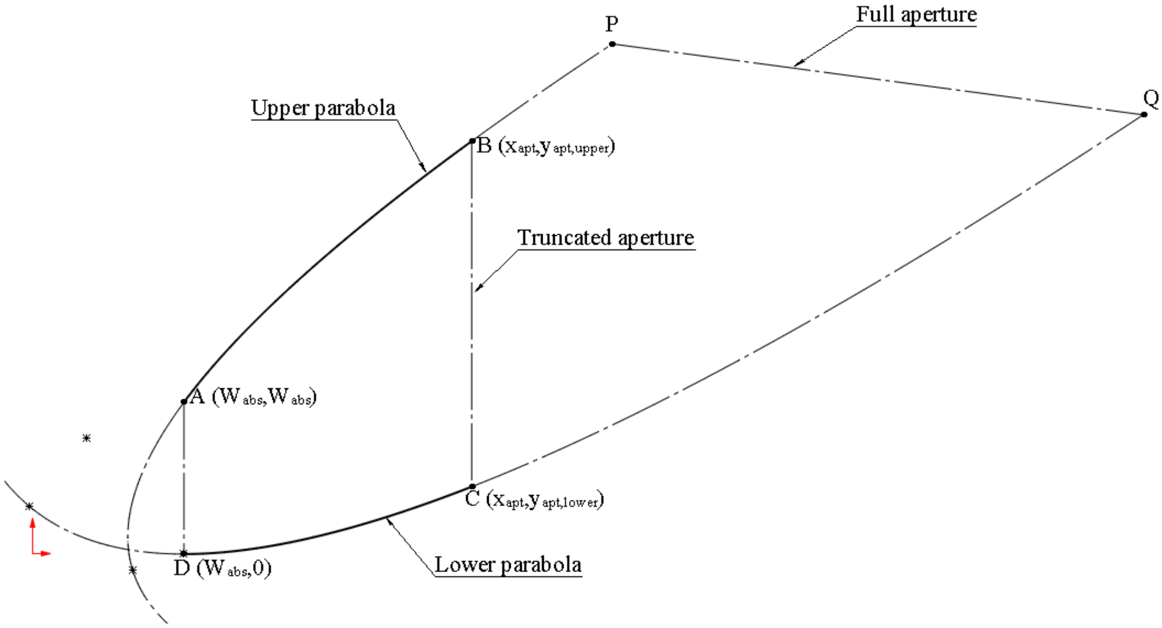

Figure 3.5: Two parabolas arranged to form the truncated parabolic section (ABCD). Dashed curves of the parabolas were eliminated.

Table 3.2: Reflector coordinate limits.

Reflector	x limits	y limits
Upper	$W_{abs}\leq x\leq x_{apt}$	$W_{abs}\leq y\leq y_{apt,upper}$
Lower	$W_{abs}\leq x\leq x_{apt}$	$0\leq y\leq y_{apt,lower}$

The equations used to model the parabolas consider x and y as function of a new parametric variable t_p assigned for each parabolic shape, as shown in Eqs. (3.4) and (3.5). These parametric equations model the exact parabolic shapes and are quadratic polynomials in t_p, which takes minimum process time to be solved.

$$x = \frac{1}{4f}\sin\theta_a t_p^2 + \cos\theta_a t_p + \Delta x \tag{3.4}$$

$$y = \frac{1}{4f}\cos\theta_a t_p^2 - \sin\theta_a t_p + \Delta y \tag{3.5}$$

where the parametric variables range to provide x and y coordinates whose limits are established in Table 3.2.

3.4.2 Circular reflector design

For this circular reflector, a quarter of a circle was used, whose centre was set at (W_{abs}, W_{abs}) and radius W_{abs}. Eq. (3.6) expresses the calculation for the circular section obtained:

$$y = W_{abs} - \sqrt{W_{abs}^2 - (x - W_{abs})^2} \tag{3.6}$$

where the coordinate limits are $0 \le x \le W_{abs}$ and $0 \le y \le W_{abs}$. The shape of the circular sector is illustrated in Figure 3.6 by the curve DE.

3.4.3 Straight reflector design

The straight reflector section comprises two vertically straight reflector of height H_{TS} above the circular section and ends at the absorber surface (whose y-coordinate is y_{TS}). The coordinate limits here are $0 \le x \le W_{abs}$ and $W_{abs} \le y \le y_{TS}$. In Figure 3.6 they are represented by the vertical segments EF and AG.

3.4.4 End reflectors design

The end reflectors are two identical flat surfaces, one at each end of the concentrator (west and east sides shown in Figure 3.1), where their boundaries are the shapes of the other reflectors altogether.

3.4.5 Summary of overall coordinates

Figure 3.6 illustrates all the reflectors arranged along with the main coordinates.

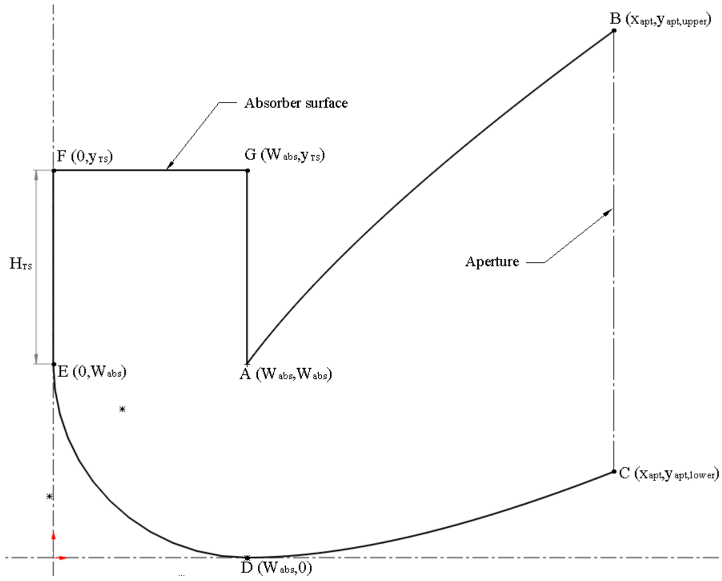

Figure 3.6: Concentrator's cross section view with the appropriate coordinate information.

Figure 3.7 shows the concentrator in three dimensions, where:

✓ AHIB and DKJC are the upper and lower parabolic reflectors;

✓ ELKD is the circular reflector;

✓ ABCDEFG and HIJKLMN are the western and eastern end reflectors, respectively;

✓ FMNG is the absorber surface and BIJC is the aperture;

✓ The concentrator's main dimensions are: depth W_{col}, height H_{col} and length L_{col}.

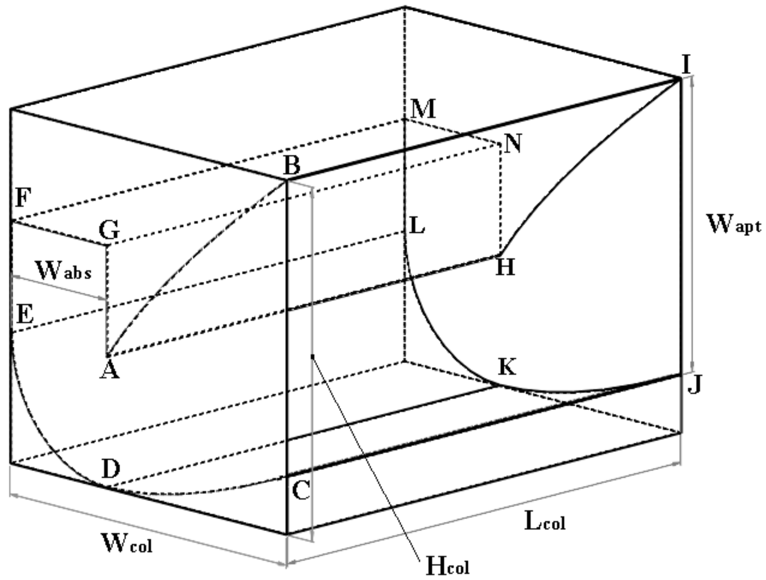

Figure 3.7: Final concentrator concept.

3.5 Ray Tracing and Optical Modelling

Ray tracing techniques are algorithms to simulate sunlight rays passing through an optical system. Ray tracing analysis gives the optical performance for complex reflecting geometries considering both direct and diffuse solar radiation (Ali et al., 2013). When a ray is incident on a reflecting surface, most of its energy will be reflected. In ray tracing, the law of reflection is applied in vector form (Winston et al., 2005). As the IACPC is a complex geometry, there is no set of analytic equations for predicting its optical performance. A ray tracing technique is therefore employed to simulate the passage of direct radiation rays through the concentrator (Ali et al., 2013). This analysis provides:

- ✓ The average number of reflections before the incoming rays reach the absorber (Shams, 2013; Benrejeb et al., 2016);
- ✓ The optical efficiency as a function of the incidence angle (Kothdiwala et al., 1996; Souliotis et al., 2011);
- ✓ Visualisation of rays' path and reflection points (Mallick and Eames, 2007; Ratismith et al., 2014; Ustaoglu et al., 2016);
- ✓ The intensity of the incident energy distribution at the absorber (Sellami and Mallick, 2013; Ali et al., 2014; Bellos et al., 2016);
- ✓ The system's optical characteristics as boundary conditions for detailed computational fluid dynamics (Mallick and Eames, 2007; Shams, 2013; Bellos et al., 2016);
- ✓ Comparisons between two or more systems (Zacharopoulos et al., 2000; Sarmah et al., 2011; Wu, 2009).

To assist the optical analysis, a 2D and a 3D ray tracing algorithms implemented in Matlab® were used to simulate direct solar radiation incident through the aperture to be reflected at the reflectors to reach the absorber. Figure 3.9 shows the concentrator oriented south facing with its length coincident to the east-west axis. A single ray is illustrated passing through the aperture at its angular components (a_s,γ_s).

The following assumptions were made in the algorithm development:

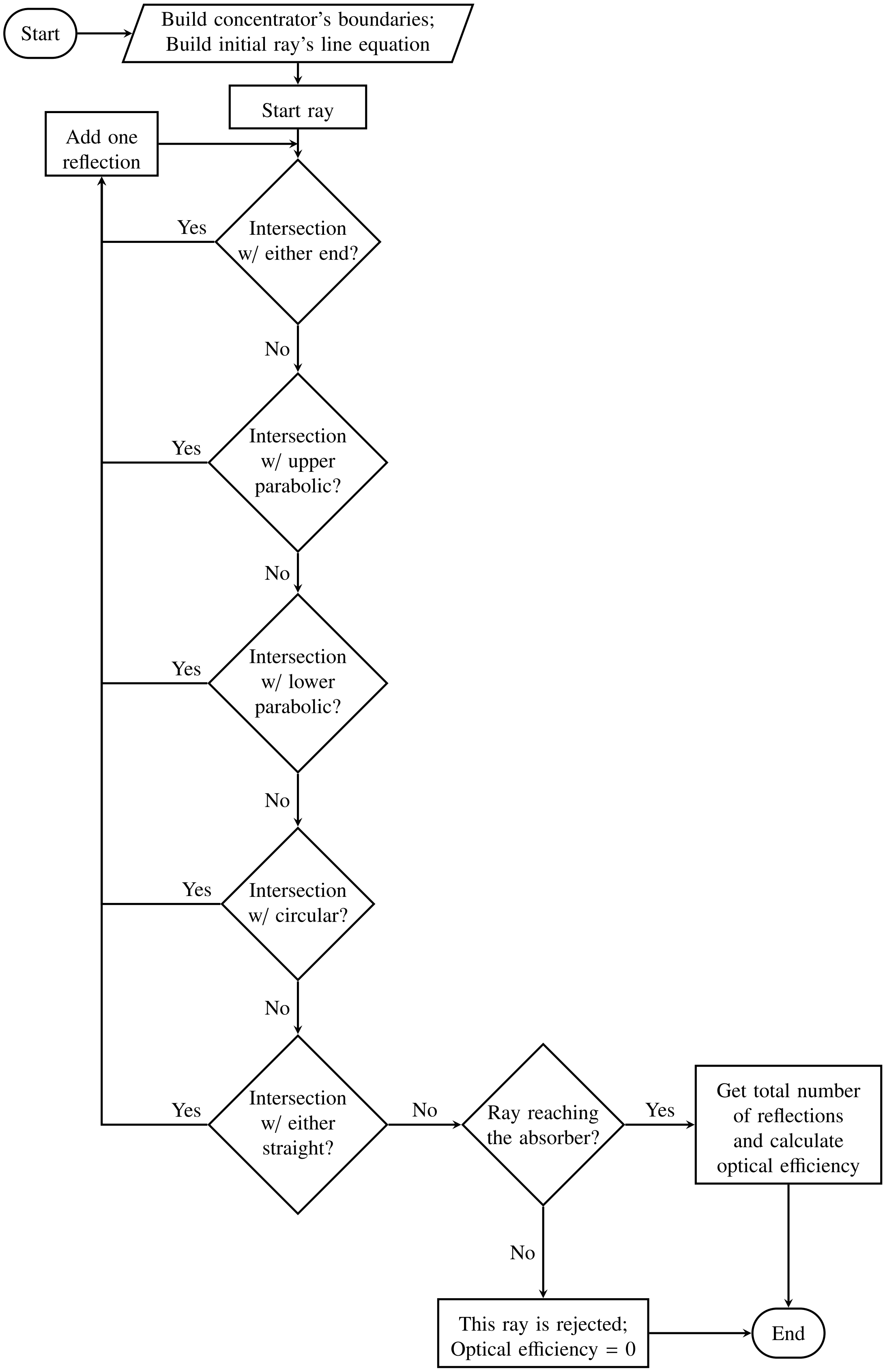

Figure 3.8: Flowchart of the algorithm to execute the optical modeling.

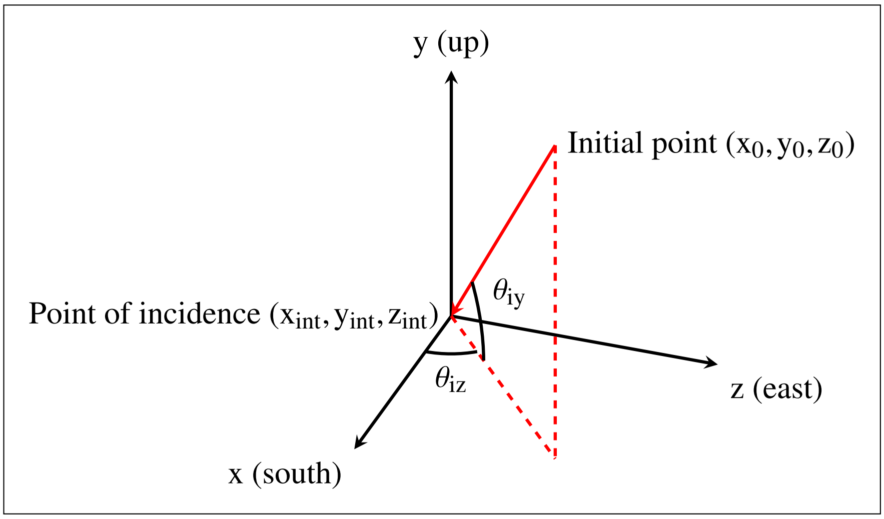

Figure 3.9: Orientation in space of one incoming ray going through the concentrator.

✓ All reflectors are specular so the incident angle is equal to the reflected angle in relation to the normal at the intersection point;

✓ 1 ray per mm^2 of aperture was initially placed on the surface and equally spaced, where each ray carries equal amounts of energy regardless of altitude and azimuth solar angles;

✓ The boundaries are the reflective surfaces shown in Figure 3.7, where the rays go through the face BIJC.

The 2D ray tracing is only the particular case of the 3D ray tracing, at which the azimuth solar angle is zero. For all the 2D simulations there is no reflections at the end reflectors. Figure 3.10 illustrates rays entering the concentrator and getting reflected until reaching the absorber, in 2D and 3D, respectively.

The optical efficiency is defined as the ratio between the absorbed and the incident solar energy. Considering number of reflections, glazing transmittance and absorber absorptance, it is calculated using Eq. (3.7) as function of the reflectors' shape and the concentration ratio (Sellami and Mallick, 2013):

$$\eta_o = \sum_{i=1}^{N_{rays}} \rho_r^{r_i} \tau_g \alpha_{abs} \tag{3.7}$$

where r_i is the number of reflections of the solar ray i.

The effective concentration ratio (C_{eff}), which is the product of the geometric con-

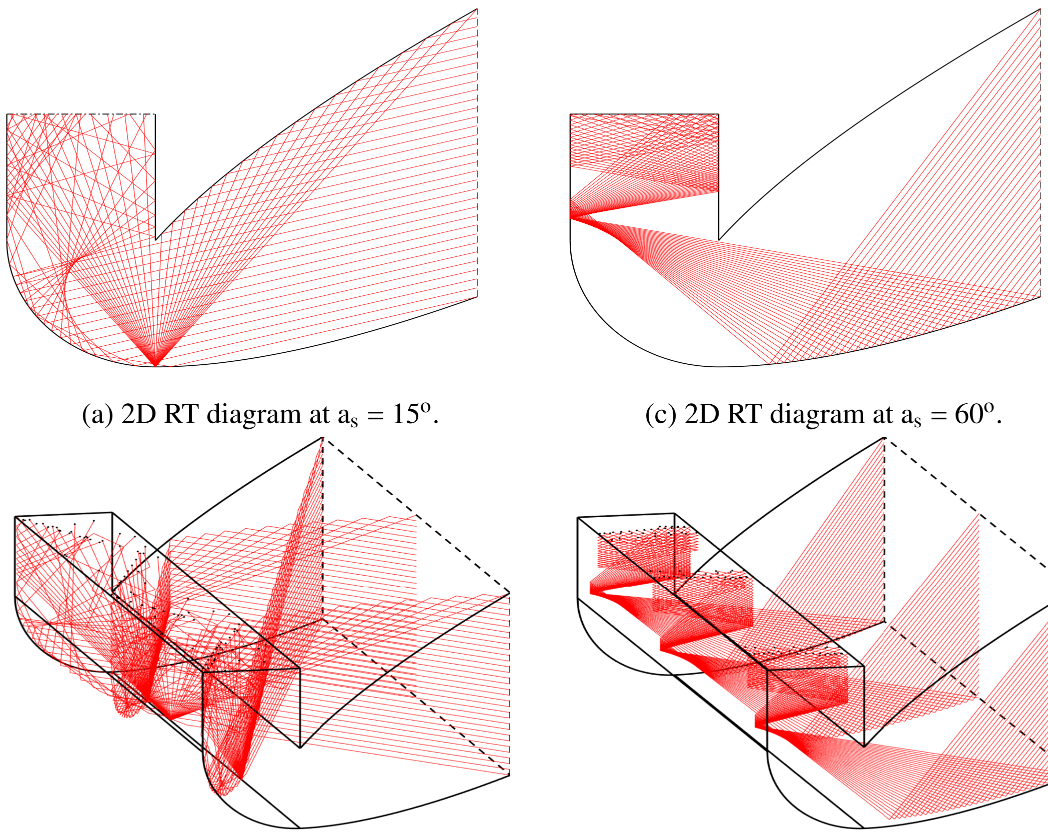

(a) 2D RT diagram at $a_s = 15^o$.

(c) 2D RT diagram at $a_s = 60^o$.

(b) 3D RT diagram at $a_s = 15^o$ and $\gamma_s = 70^o$.

(d) 3D RT diagram at $a_s = 60^o$ and $\gamma_s = 10^o$.

Figure 3.10: Ray tracing diagrams in 2D and 3D.

centration ratio and the optical efficiency, is given by Eq. (3.8). C_{eff} is useful to select shapes capable of enhancing both concentration of energy at the absorber and optical efficiency. All the optical outputs τ_g, η_o and C_{eff} can be calculated as averaged values to represent the whole period of operation for each particular concentrator. They were referred to as $\tau_{g,avg}$, $\eta_{o,avg}$ and $C_{eff,avg}$.

$$C_{eff} = \eta_o CR \tag{3.8}$$

The collector's dimensions can also be related as dimensionless relative to the absorber width: $W^* = W_{col}/W_{abs}$, $H^* = H_{col}/W_{abs}$ and $L^* = L_{col}/W_{abs}$. The dimensionless parameter A^* was introduced to consider the reflector area relative to the absorber area, where:

$$A^* = \frac{A_R}{A_{abs}} = \frac{W_r}{W_{abs}} + 2\frac{W^*H^*}{L^*} \tag{3.9}$$

where W_r is the width of reflective material employed for a particular shape.

3.6 Results and Discussion

3.6.1 Overview and collector specification

This section was organised as follows:

✓ Design analysis of a standalone collector's geometry by means of the dimensionless parameters W^*, H^* and A^* at different parabolic shapes as function of the truncation level (in terms of the geometric concentration ratio CR);

✓ Optical performance considering the average values of optical efficiency η_o and effective concentration ratio C_{eff} at different shapes (in terms of α_{P2}) as function of CR at a fixed absorber width, zero tertiary section height ($H_{TS} = 0$) and $L_{col} = 10W_{abs}$,

✓ Optical performance of two different geometries by varying the length;

✓ Selection of the collector for further fabrication;

✓ Evaluation of the cavity height on the optical efficiency and the energy distribution over the absorber;

✓ Optical characterisation of the collector.

An optical analysis was conducted for an air heating solar concentrating collector with the following specifications:

✓ The absorber absorptance (α_{abs}) is 0.85;

✓ The reflector reflectance (ρ_r) is 0.95;

✓ A 4-mm thick low iron glass was employed with a refractive index of 1.526 and an extinction coefficient of 4 m^{-1}. When the rays are perpendicular to the surface, the value of τ_g is 0.90;

✓ The maximum truncation level was set to result in the minimum geometric concentration ratio of 2.0 regardless of the parabolic shape.

✓ The upper parabola axis angle was set to be coincident to the lowest solar altitude angle ($\alpha_{P1} = 15°$);

✓ The range of lower parabola axis angles (α_{p2}) considered was between 44° to 61°.

3.6.2 Effect of the glazing inclination on the light transmittance

Glazing transmittance τ_g varies in relation to the incident angle θ_i as shown in Figure 3.11.

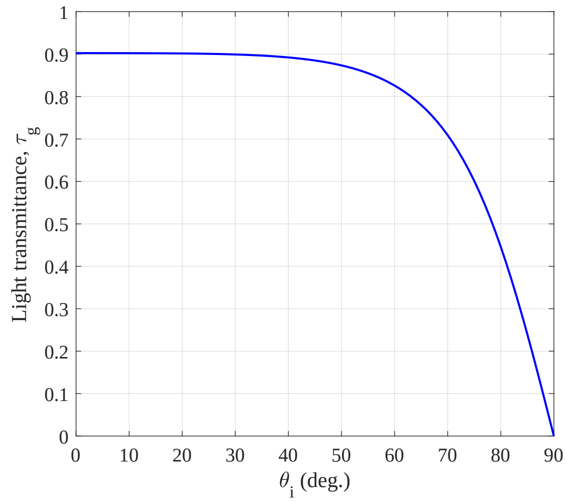

Figure 3.11: Transmittance as function of the angle of incidence.

The average transmittance calculated as function of the glazing inclination are shown in Figure 3.12. A maximum average transmittance is at β = 33° as 0.8907, thus is the inclination of which the glazing losses are minimum overall. Compared to the transmittance with the glazing placed vertically, there is a relative difference of 14%. However, an inclination at β = 33° brings practical difficulties, such as high accumulation of dust and rain water over the glazing cover. For this reason, steeper inclination was desirable, even though there is less solar energy reaching the absorber. Therefore, β = 62° was chosen, where $\tau_{g,avg}$ = 0.8770, which is more than 98% of the maximum average transmittance.

The results of instantaneous light transmittance against daytime is shown in Figure 3.13 for different glazing inclinations on 30th June. The maximum transmittance profile is at β = 33°, whereas the one of inclination at the local latitude angle (β = 53°) and the one at β = 62° do not present significant difference. All the three profiles are similar between 11h and 16h of this day. On the other hand, the profile of which the glazing is at the

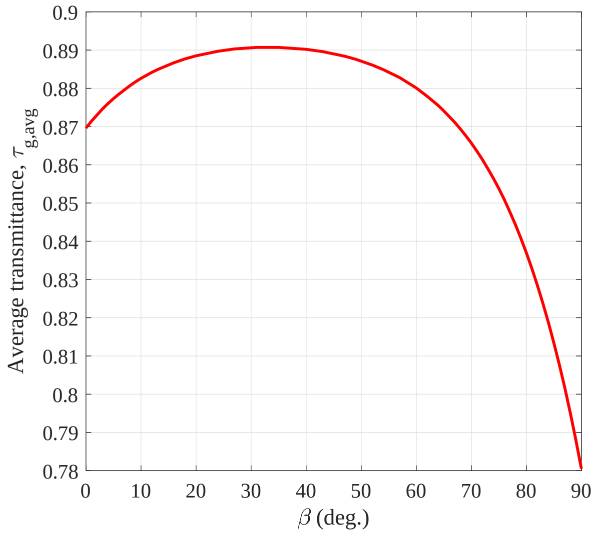

Figure 3.12: Average transmittance dependent on glazing inclination.

vertical shows the highest amount of solar reflection.

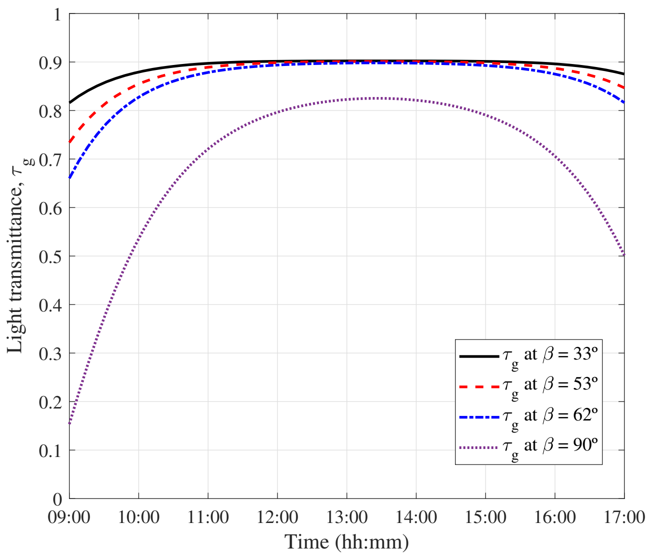

Figure 3.13: Light transmittance throughout the day (30th June).

3.6.3 Design analysis of standalone collectors

The dimensionless parameters W* and H* are presented by graphs in Figure 3.14, where each graph corresponds to a particular shape. The maximum concentration ratio, obtained from the shape at $\theta_{P2} = 44°$, was found to be 2.98. For the same concentration ratio, both W* and H* decrease as θ_{P2} increases because the concentrator's acceptance angle is broader. For the same concentrator (fixed shape), the size increases when CR also increases until its maximum aperture width, thus defining its maximum size (indicated by the dashed line in Figure 3.14). The smallest concentrator has the shape of narrowest acceptance angle (θ_{P2} = 44°) and smallest concentration ratio (CR = 2.0) for being the most truncated ($W_{col} = 2.2W_{abs}$ and $H_{col} = 2.2W_{abs}$), whereas the largest concentrator has also the narrowest acceptance angle but at the highest concentration ratio ($W_{col} = 7.3W_{abs}$ and $H_{col} = 5.4W_{abs}$).

As shown in Figure 3.15, the dimensionless parameter A^* increases as the concentrator's size increases. Thus the graphs in Figures 3.14 and 3.15 are similar. The reflector area varied from $5.4A_{abs}$ for the smallest concentrator to nearly $24A_{abs}$ for the largest one. Because this collector is an asymmetric compound parabolic concentrator, these graphs are similar to those found by Rabl (1976b) for symmetric concentrators.

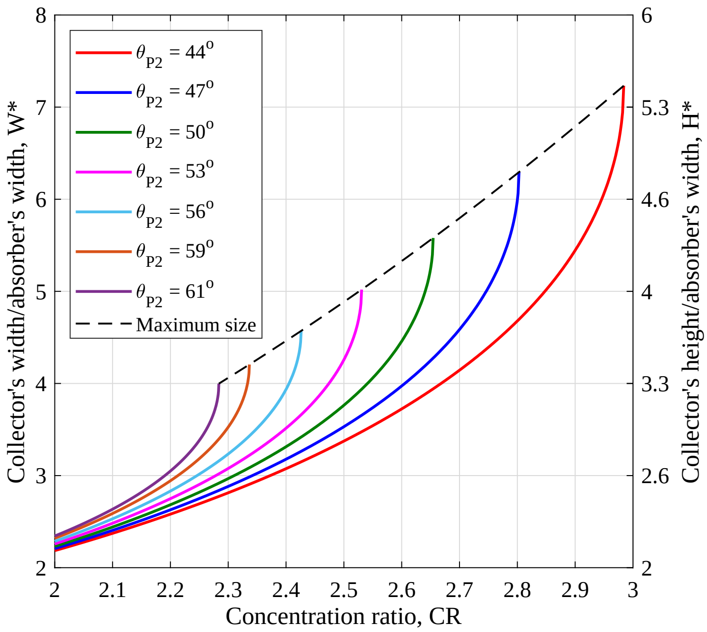

Figure 3.14: Dimensionless parameters W^* and H^* matching particular CR for different shapes.

3.6.4 Optical performance of standalone collectors

3.6.4.1 Optical performance by varying parabolic shape and truncation level

The average optical efficiency as a function of CR for different shapes are shown in Figure 3.17. For concentrators of concentration ratio below 2.2 the shape of highest optical efficiency is the one of θ_{P2} = 44°. For truncation levels resulting in concentration

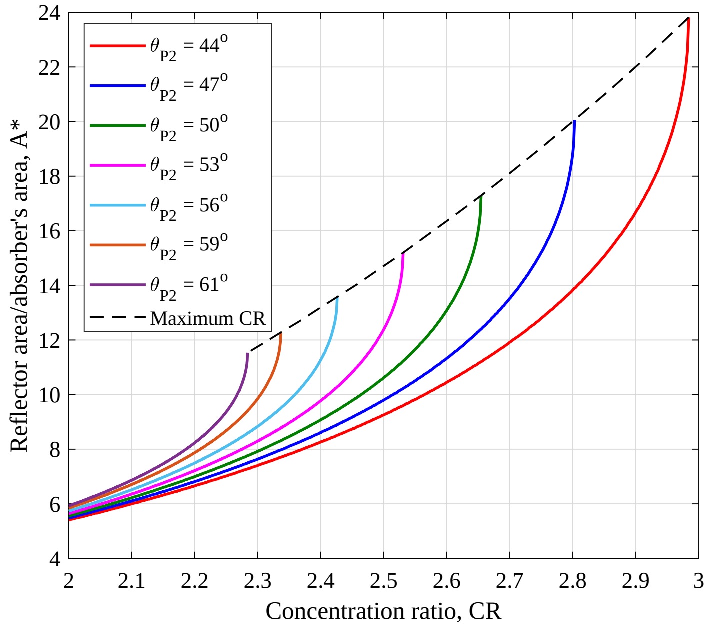

Figure 3.15: Dimensionless parameter A* matching particular CR for different shapes.

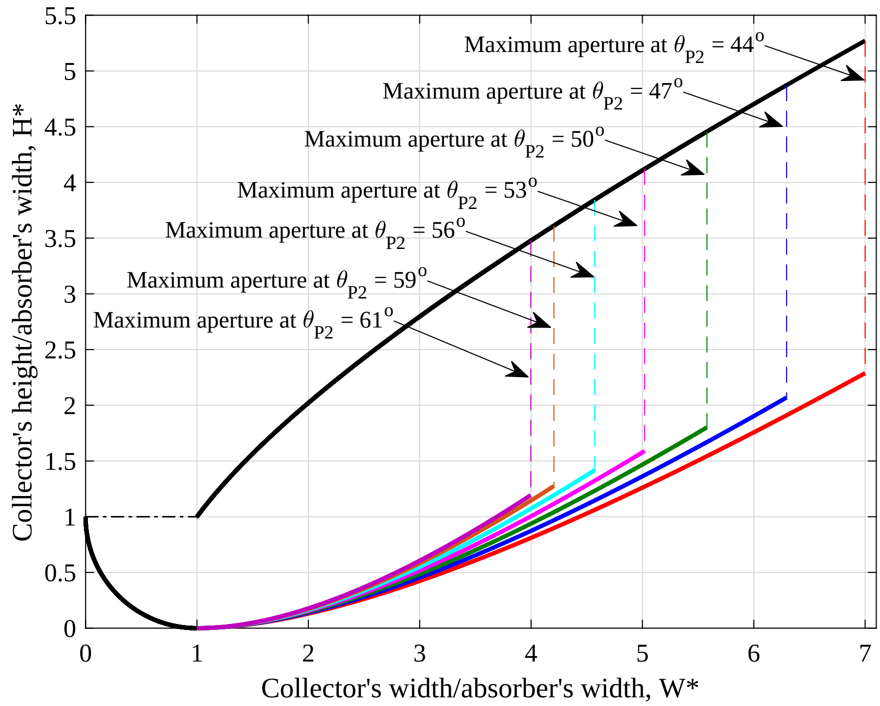

Figure 3.16: Dimensionless parameter A* matching particular CR for different shapes.

ratio above 2.4, concentrators are unable to accept a portion of direct solar radiation of solar altitude angles (a_s) above 50°, which is the reason why the graphs has decaying behaviours. The shape of θ_{P2} = 44° and CR = 2.0 is the most efficient with $\eta_{o,avg} = 0.689$ for being the smallest concentrator that accepts all direct solar radiation in the period of operation. The least efficient concentrator is the one of maximum CR ($\eta_{o,avg} = 0.432$)

because it requires more reflections for the solar rays to reach the absorber and it does not accept direct solar radiation above 50° of a_s, which is equivalent to 35% of the period of operation.

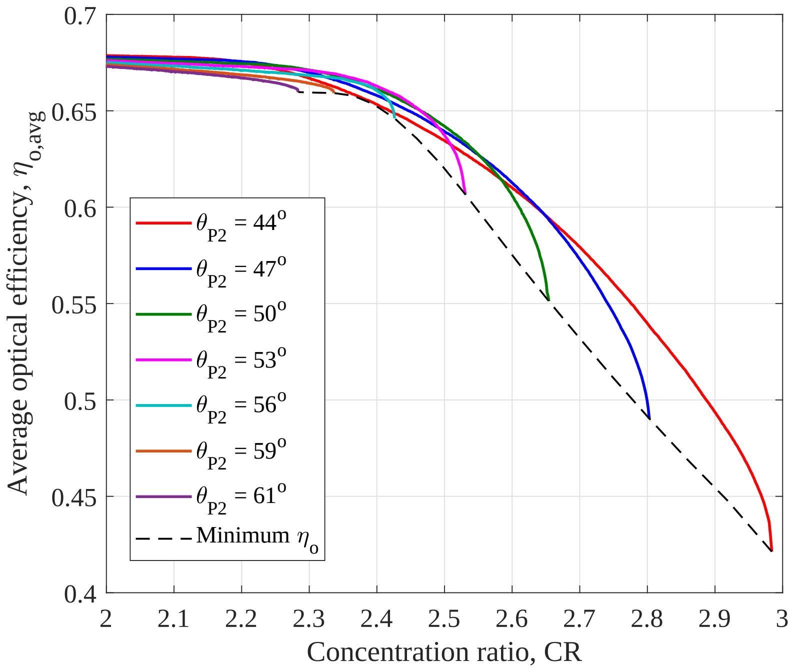

Figure 3.17: $\eta_{o,avg}$ matching particular CR for different shapes.

The average effective concentration ratio $C_{eff,avg}$ against CR and θ_{P2} is shown in Figure 3.18. Geometries of θ_{P2} below 56° have maximum values of $C_{eff,avg}$ above 1.55 at each particular level of CR. After these conditions, the graphs drop dramatically as CR is increased due to the optical efficiency fall discussed previously. The shape correspondent to the smallest $C_{eff,avg}$ is the one of maximum CR ($C_{eff,avg}$ = 1.3) for being the least optically efficient; and the shape of maximum $C_{eff,avg}$ is the one of θ_{P2} = 51° and CR = 2.5 although it is not able to accept direct solar radiation above 56° of a_s. Concentrators of CR = 2.0 are less effective in $C_{eff,avg}$ despite being the most optically efficient concentrators.

3.6.4.2 Optical performance by varying concentrator length

The values of $\eta_{o,avg}$ and $C_{eff,avg}$ were calculated as function of the dimensionless parameter L^* for two different concentrators: the most optically efficient (CR = 2.0) and one with highest $C_{eff,avg}$ (CR = 2.5). The results can be seen in Figure 3.19. The values of $\eta_{o,avg}$ assuming an infinite length were found to be 0.70 (CR = 2.0) and 0.662 (CR

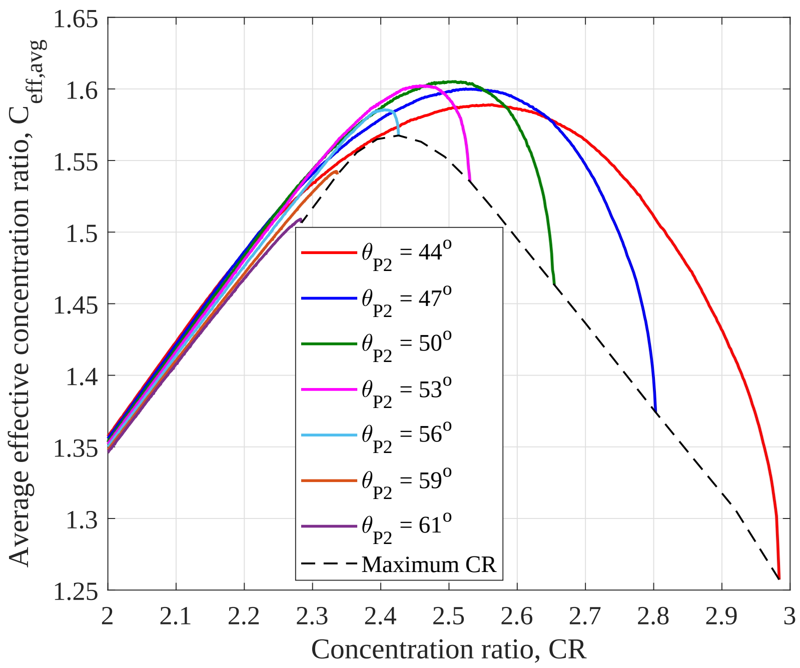

Figure 3.18: $C_{eff,avg}$ matching particular CR for different shapes.

= 2.5). The end losses are higher for shorter concentrators due to greater number of reflections. When length equals $3W_{abs}$, where $\eta_{o,avg}$ is more than 95% of the optical efficiency assuming infinite length. When $L_{col} = 10W_{abs}$, the values of $\eta_{o,avg}$ are more than 98% of those assuming infinite length. Hence, longer concentrator incurs in less reflections losses at the ends, thus leading to higher optical efficiencies. However the cost of additional reflective material and weight might not compensate the little significant gain in energy collection.

The end effect can be observed in more details when $\eta_{o,avg}$ for five different length ratios are plotted against time of operation. This is shown in Figure 3.20 specifically on 30^{th} of June for the smallest concentrator's performance (CR = 2.0). The end losses are higher in the beginning of the day due to higher values of the azimuth solar angles γ_s incurring in more reflections at the ends and therefore collectors collect less energy before noon, especially for shorter concentrators.

3.6.5 Selection of the collector to be fabricated

In this topic, a criterion was used to select the collector's geometry to be fabricated for tests. As mentioned in section 3.3, the collector must accept direct solar radiation with

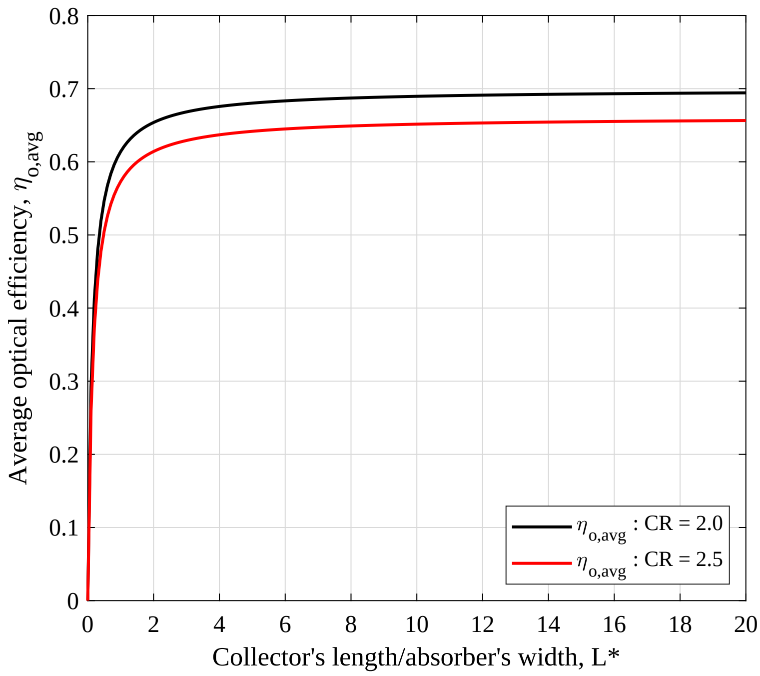

Figure 3.19: $\eta_{o,avg}$ matching particular L^* for two different concentrators.

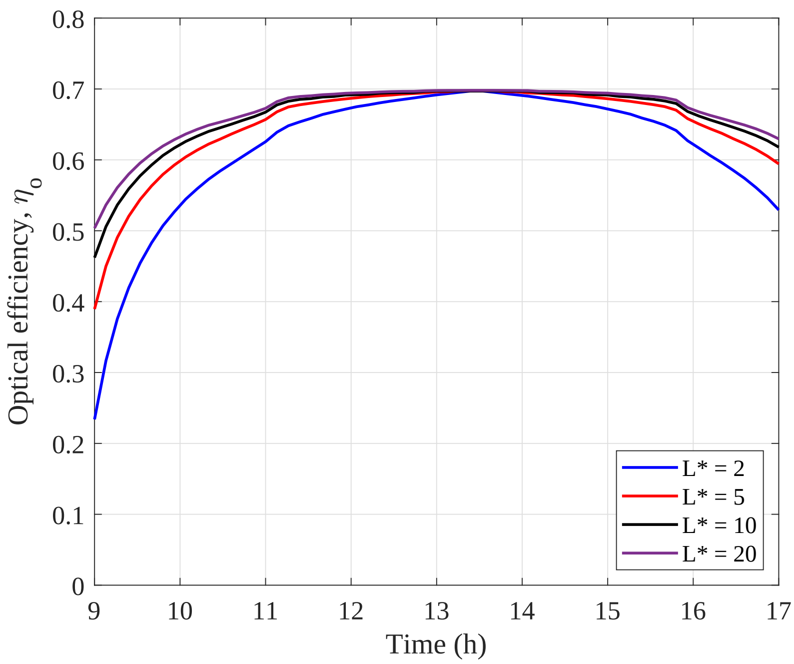

Figure 3.20: η_o vs. time for a collector at different length ratios.

altitude solar angles between 15° and 61°. Once these limits are set, an initial design of the collector was sketched of which the angles of both parabolic axes are coincident to those limits so that all direct radiation within this range is accepted. From the initial design (shown in Figure 3.21 in red), the absorber width was found with the aim of achieving the maximum concentration ratio, which is 2.284. The actual aperture width (W_{apt}) will be

330 mm in order to have three collectors stacked on every metre of wall height. Hence, the absorber width (W_{abs}) was calculated and found to be 145 mm.

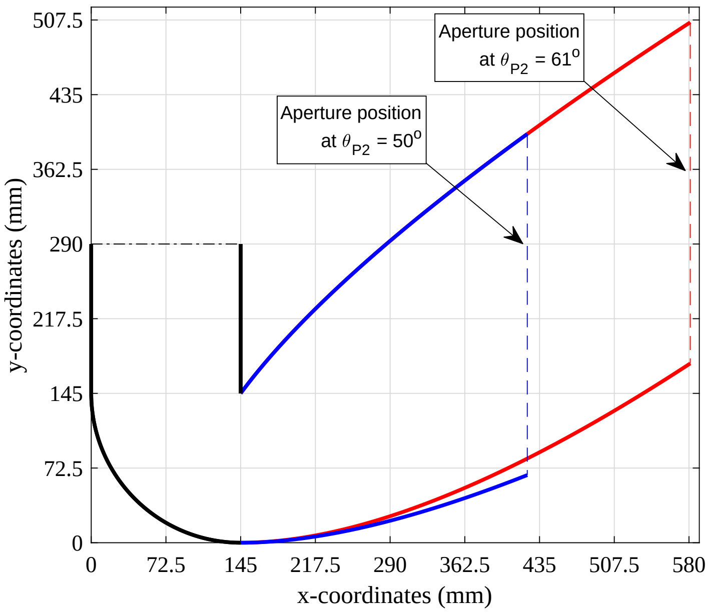

Figure 3.21: Comparison between the collector at 61° of θ_{P_2} (red) and the one at 50° of θ_{P_2} (blue).

As this collector is truncated, the range of angular acceptance may be broader than the limits previously defined. In order to validate this hypothesis, the ray tracing algorithm was used to check whether all the rays within this range are accepted. A graph of θ_{acc} vs. a_s was plotted and shown in Figure 3.22. The collector fully accepts direct radiation from 17° to 63° of a_s, which exceeds the upper limit. Therefore, the collector's optical performance can be enhanced by further modifications to the reflectors. In this particular case, it was done by decreasing the lower parabola axis angle (θ_{P_2}). As this change in shape affects the number of reflections, $\eta_{o,avg}$ was calculated at different values of θ_{P_2} and two graphs were plotted in Figure 3.23. Although there is no significant gain in the average effective concentration ratio ($C_{eff,avg}$ = 1.52) when both designs are compared, the parameter A* is reduced from 11.7 to 7.8, hence reducing the reflector area required by 33%.

Furthermore, by ray tracing, the collector's angular acceptance at θ_{P2} = 50° was calculated and shown in Figure 3.22 (in red). Although the full acceptance is up to 59°, θ_{acc} at 60° is above 90%, which poorly influences the optical efficiency. From this analysis,

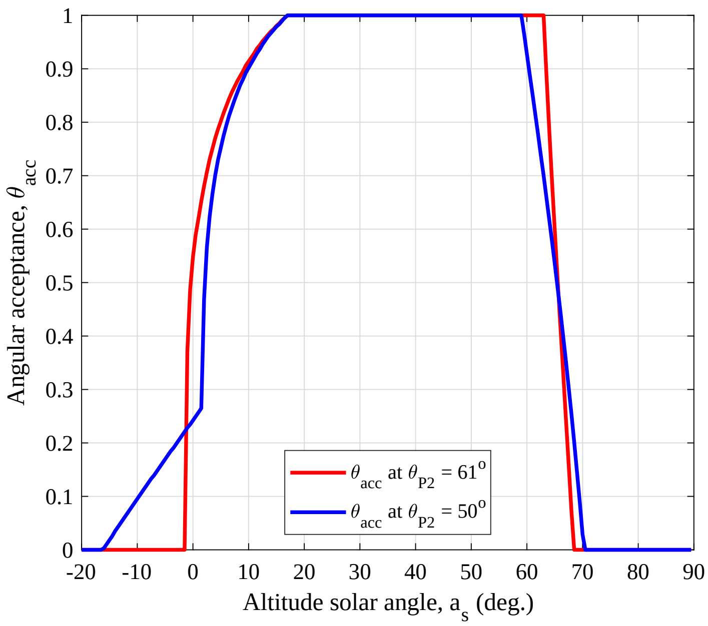

Figure 3.22: Angular acceptance vs. solar altitude angle for the collector at 61° of α_{P2} (red) and the one at 50° of α_{P2} (blue).

the angles of the upper and lower parabola axes was chosen to be 17° and 50° respectively.

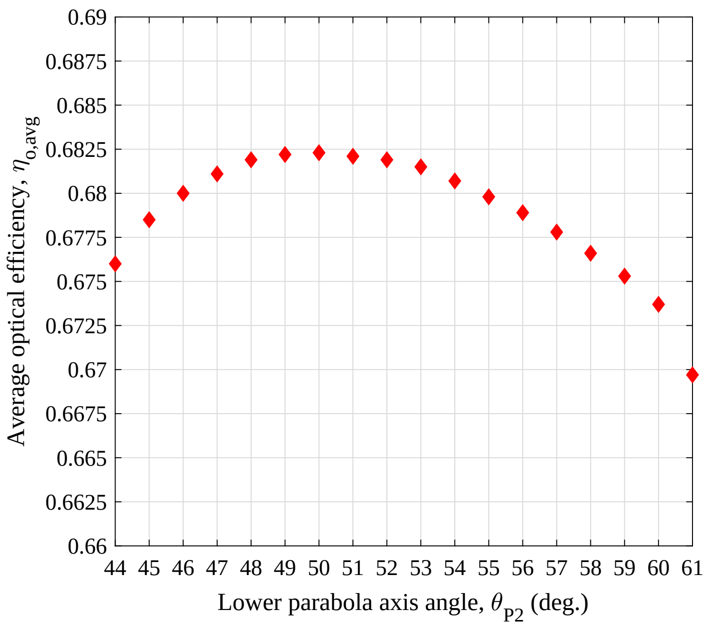

Figure 3.23: Average optical efficiency *versus* lower parabola axis angle.

For the selection of the collector's length, ray tracing technique was used to calculate the average optical efficiency as function of this geometric parameter. The graph of $\eta_{o,avg}$ versus L_{col} was plotted and shown in Figure 3.24. For lengths above 2 m, there is little gain in efficiency (above 0.68), whereas below this value, the reflection losses at the ends are higher, which worsens the optical performance. At L_{col} = 1.25 m, the collector's optical efficiency is 95% of the maximum theoretical efficiency ($\eta_{o,avg}$ = 0.67). Therefore, under the optical consideration, this length was chosen for the collector's fabrication.

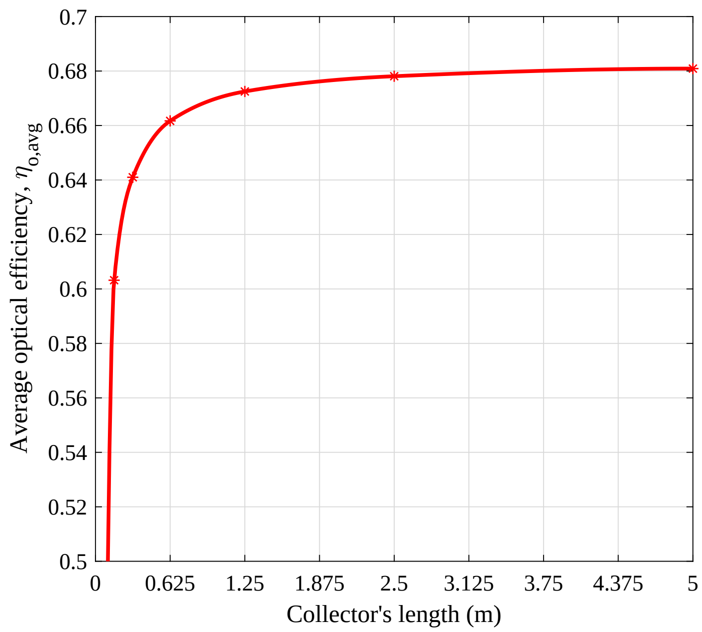

Figure 3.24: Average optical efficiency *versus* collector's length.

3.7 Optical characterisation of the proposed collector

3.7.1 Effect of the cavity height

To understand the effect of the cavity height in the analysis, the average optical efficiency was calculated and shown in Figure 3.25 as function of the tertiary section height. These results are straightforward, as the addition of a new reflective section will imply in more reflections, thus decreasing the average efficiency by approximately 3.5%.

To better illustrate the effect of the tertiary section height, the optical profile of the collector on 30th of June at three different heights was calculated and shown in Figure 3.26. From 09:00 to 10:30 and from 16:20 to 17:00 the three profiles impose nearly the same efficiency. The highest difference is at 12:00, where η_o with no tertiary height is 0.71 and η_o at $H_{TS} = W_{abs}$ is 0.61.

Although the optical efficiency is reduced by the increase of the tertiary section

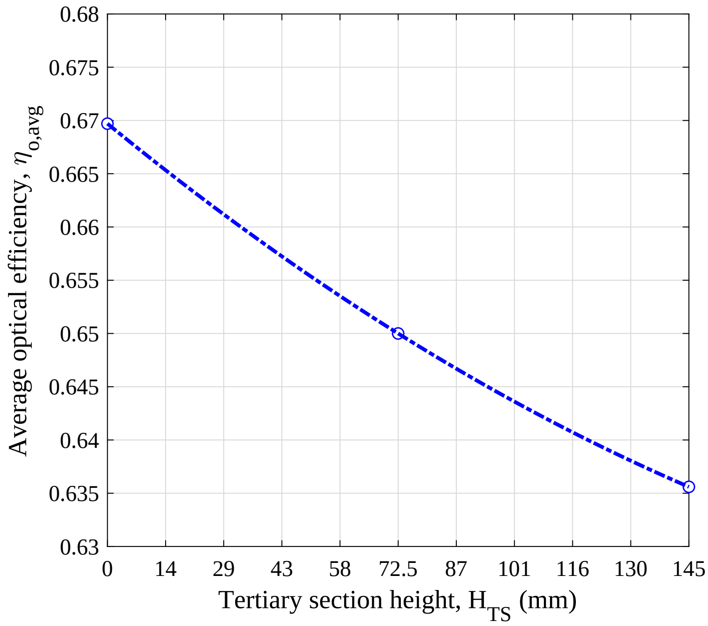

Figure 3.25: Average optical efficiency as function of the tertiary section height.

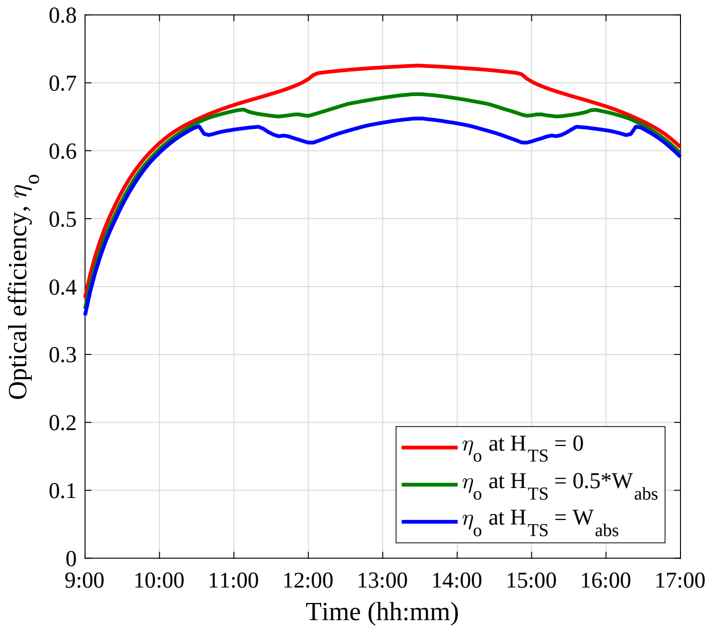

Figure 3.26: Optical efficiency profile for three tertiary section heights on 30th of June.

height, the cavity has a function of distributing the incoming energy uniformly along the absorber surface. To apply this function, the results of the simulation a_s at 54° was selected as an example and this can be seen in Figures 3.27, 3.28 and 3.29. From Figure 3.27, a high energy peak concentrated in one millimetre of absorber width is observed (12500 W/m^2) and all the energy is concentrated in 45 millimetres. From Figure 3.28 the energy flux is distributed through all the absorber area where the peak region of 980

W/m^2 is concentrated in 6 mm of width. From Figure 3.29, the energy is more distributed across the absorber surface, where the maximum energy flux is 740 W/m^2 across half the absorber width. Hence, the tertiary section helps to distribute the solar energy more uniformly over the absorber area, which is desirable for further heat transfer even though the reflection losses are higher. For this reason, the cavity height was set to be 145 mm.

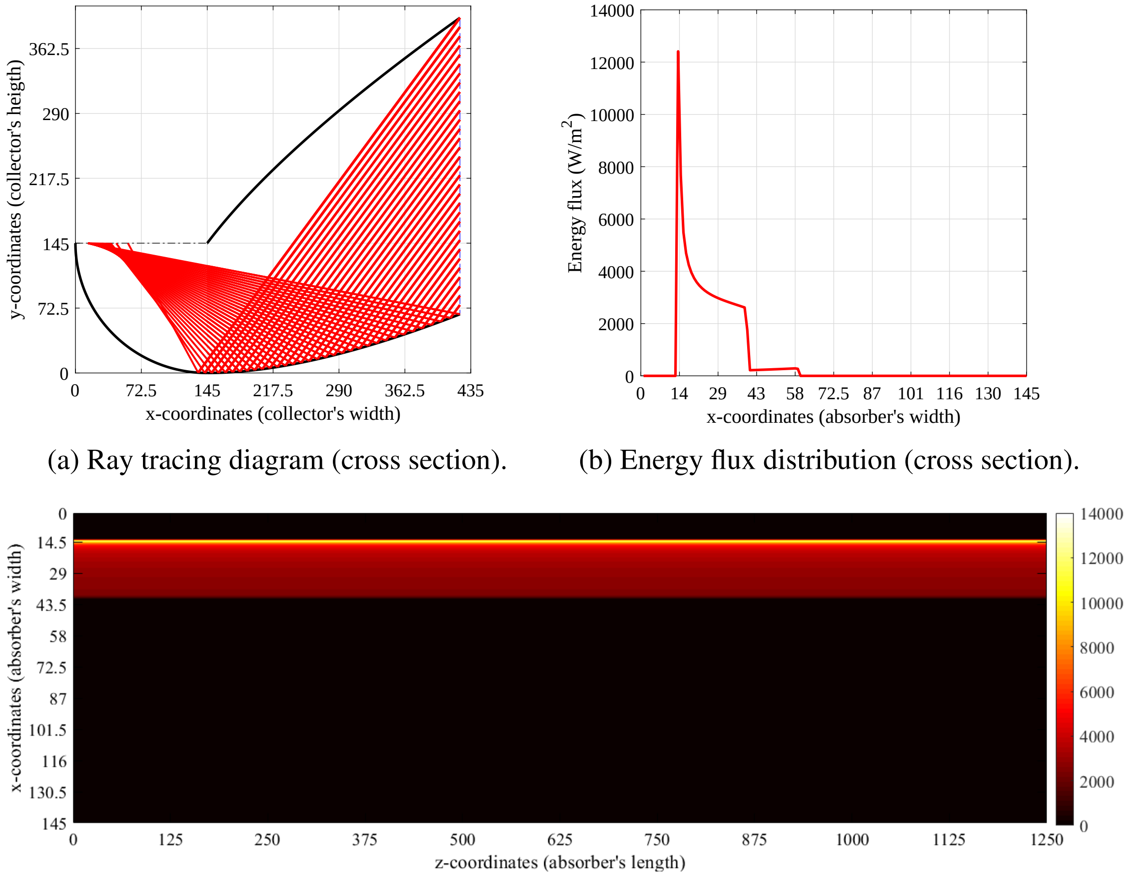

(a) Ray tracing diagram (cross section). (b) Energy flux distribution (cross section).

(c) Energy flux distribution over the absorber surface (top view).

Figure 3.27: Ray tracing diagram in 2D and energy flux distribution over the absorber width with no tertiary section.

3.7.2 Optical efficiency profile

After the optical analysis, the concentrator's design has been defined as shown in Figure 3.30 and the main geometric parameters are summarised in Table 3.3. The glazing inclination has been set at $\beta = 62°$ due to practical reasons related to its width.

It is also important to show the optical profile as in Figure 3.31, where the optical efficiency is presented as function of daytime and date during the summer. At early in

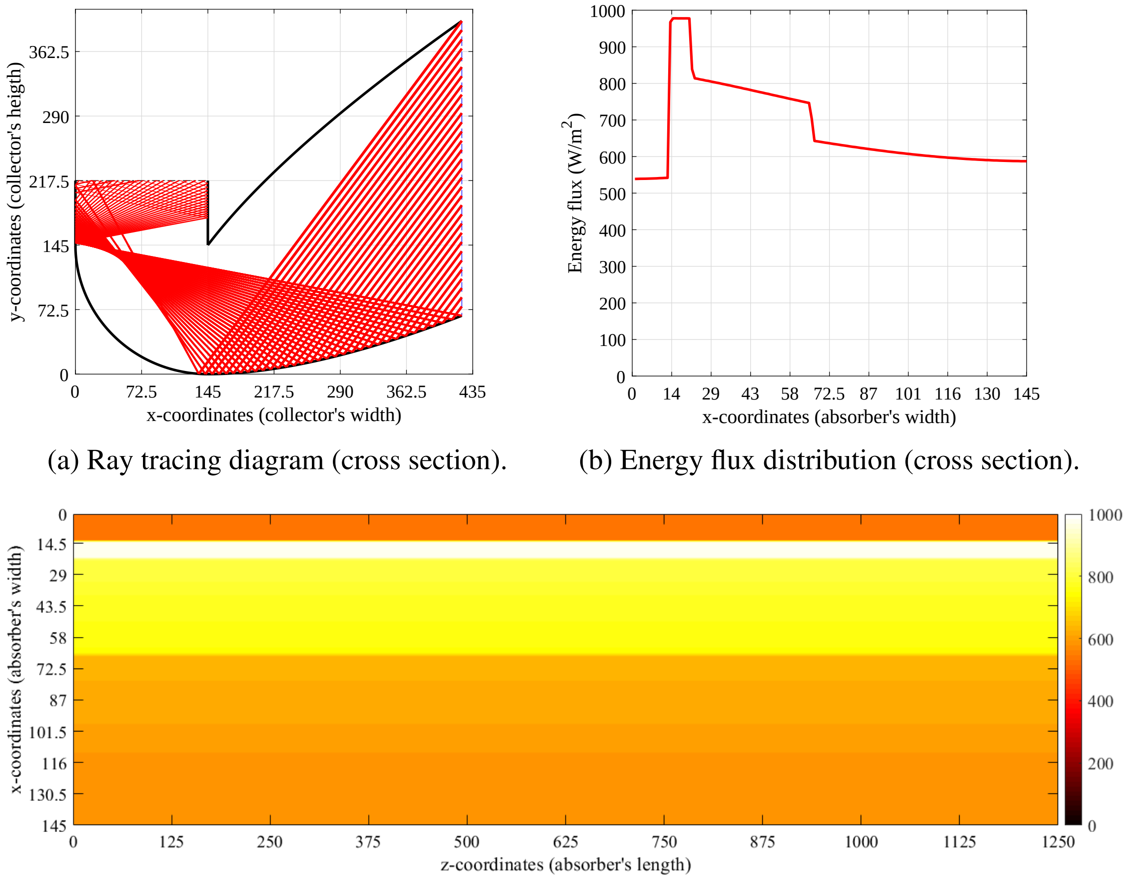

(a) Ray tracing diagram (cross section). (b) Energy flux distribution (cross section).

(c) Energy flux distribution over the absorber surface (top view).

Figure 3.28: Ray tracing diagram in 2D and energy flux distribution over the absorber width with tertiary section height of 72.5 mm.

Table 3.3: Geometric parameters of the concentrator to be fabricated.

Symbol	Geometric parameter	Value
L_{col}	Concentrator length	1.25 m
H_{col}	Concentrator height	0.40 m
W_{col}	Concentrator depth	0.43 m
W_{abs}	Absorber width	0.145 m
A_{abs}	Absorber area	0.18 m^2
W_{glaz}	Glazing width	0.27 m
A_{glaz}	Glazing area	0.34 m^2
β	Glazing inclination	62°
W_{apt}	Aperture width	0.33 m
A_{apt}	Aperture area	0.41 m^2
H_{TS}	Cavity height	0.145 m
CR	Concentration ratio	2.28
A_R	Reflector area	2 m^2

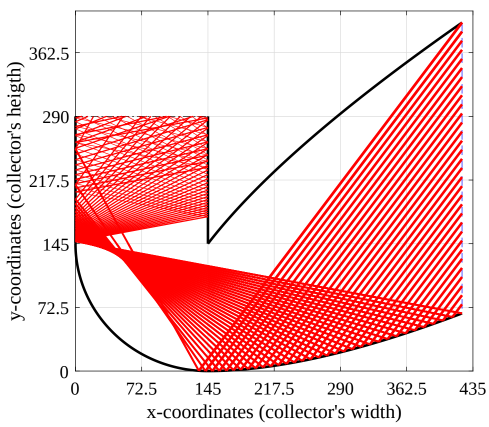

(a) Ray tracing diagram (cross section).

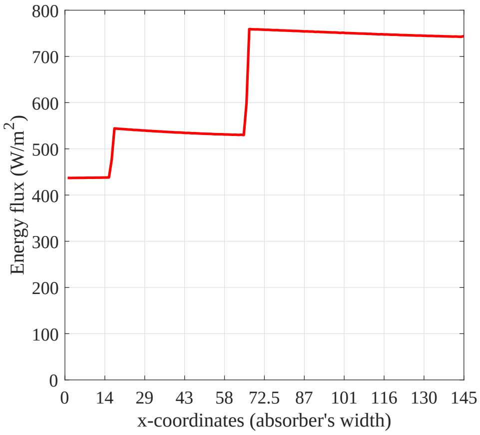

(b) Energy flux distribution (cross section).

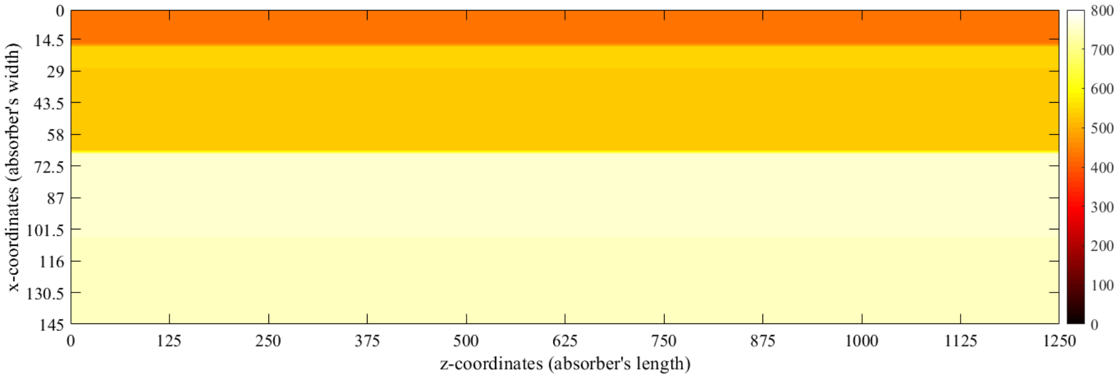

(c) Energy flux distribution over the absorber surface (top view).

Figure 3.29: Ray tracing diagram in 2D and energy flux distribution over the absorber width with tertiary section height of 145 mm.

the morning, the optical efficiency is lower due to larger number of reflections at one end of the collector and from 10:30 the efficiency keeps higher than 0.60 and the maximum value is 0.69 at noon one the last days of summer. The average optical efficiency for direct radiation of this collector is 0.67. It is worth noting that the optical profiles of multiple stacked collectors operating in connection are identical, which results in an equivalent quantity of energy available on the absorber surface in each collector. To determine the amount of energy absorbed by a flow of air, it is imperative to conduct experimental studies or utilize a valid energy balance calculation.

3.8 Chapter Summary

The selection of an air heater concentrator with the absorber horizontally facing downwards aims to concentrate solar thermal energy inside the cavity and suppress heat

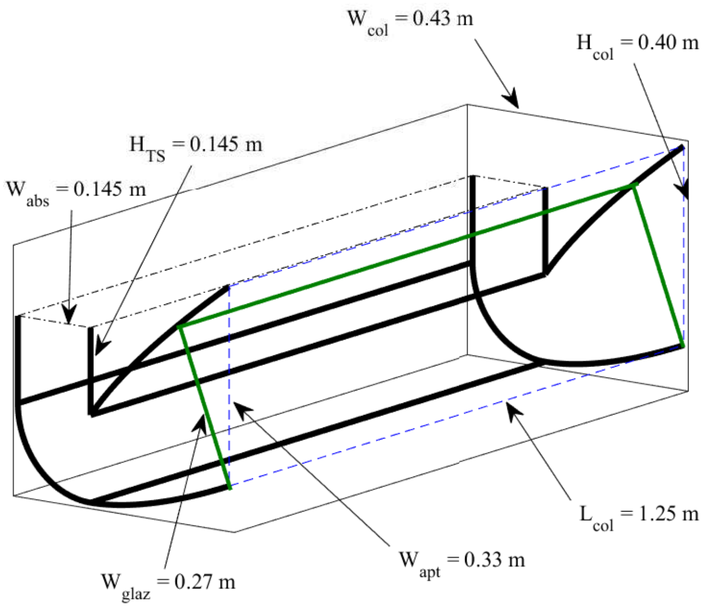

Figure 3.30: Cross section of the collector's final design.

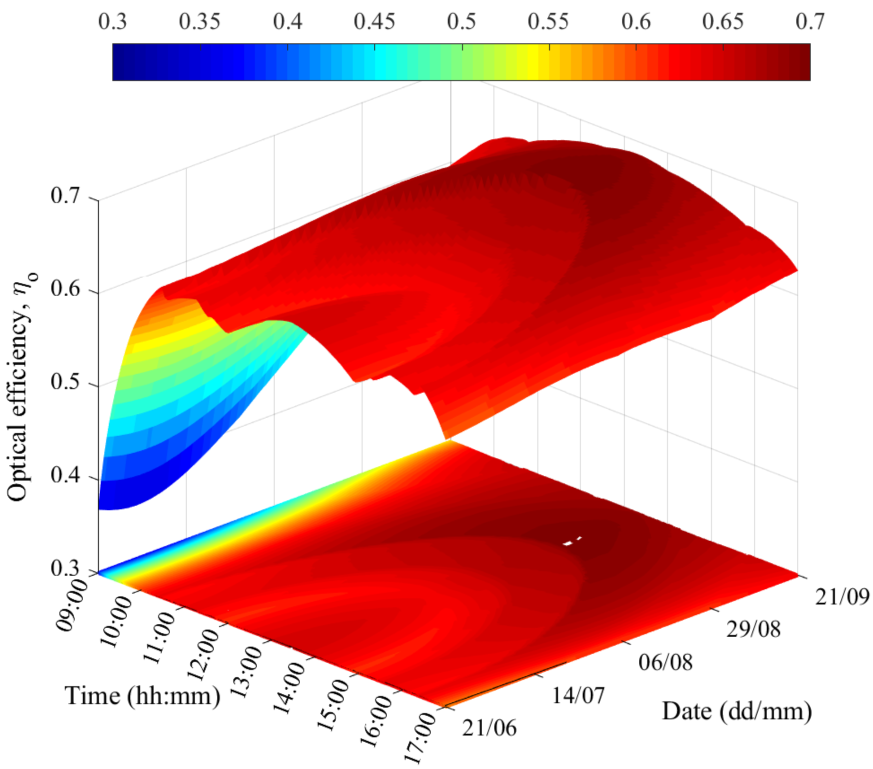

Figure 3.31: Optical efficiency profile throughout the whole period of operation.

losses. With the assistance of a ray tracing technique in 3D, an optical analysis has been undertaken to evaluate its optical efficiency considering factors as: glazing transmittance, truncation level, length and tertiary section height. The results show that there is a maximum value of optical efficiency for a particular parabolic reflector shape and a maximum value of glazing transmittance at different inclinations. It was also concluded that the energy distributed along the absorber area is more uniform with a tertiary section rather than without it even though the optical losses are higher. The effect of the tertiary section on the collector's performance needs to be further assessed, via thermal modelling and outdoor experiments. Finally, a solar concentrator design was proposed through optical analysis, and its 3D optical profile over time was presented at the end of the chapter. The proposed air heater concentrator is able to absorb in average 67% of direct solar radiation during most part of the day in the period evaluated.

CHAPTER 4

EXPERIMENTAL PERFORMANCE ANALYSIS

The aim of this chapter is to analyse the outdoor experimental performance of the solar air heater prototype fabricated using the concentrator designed in Chapter 3. This air heating system was fabricated and tested at Technological University Dublin, Ireland. The specific objectives are to:

✓ Present the materials and components for fabrication;

✓ Describe the data collection procedure and equipment used;

✓ Evaluate the thermal performance of the system in open loop configuration.

4.1 Materials for the prototype

4.1.1 Absorber surface selection

The function of the absorber surface in solar thermal systems is to retain thermal energy from incoming solar radiation. To meet this objective, carbon fibre weave fabric has been selected to be the absorbing material (Figure 4.1). Although it is not conventionally employed in solar air heating systems (Shams, 2013), its utilisation brings two advantages: i) it has natural perforations, and; ii) it reduces the system's weight – compared to an aluminium plate of same dimensions, the carbon fibre surface is 40% lighter.

Carbon fibre weave's physical properties are presented in Table 4.1. Absorptivity

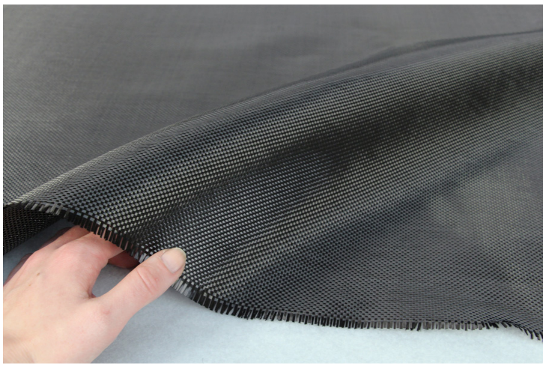

Figure 4.1: Carbon fibre weave fabric (Easy Composites, 2017).

data were reported by Wu et al. (2012), whereas thermal conductivity and specific heat were obtained from the material supplier Easy Composites (Easy Composites, 2017). Despite being a modest thermal conductor, Gawlik et al. (2005) reported that this factor poorly influences the thermal efficiency of an air heating system with perforated absorber.

Table 4.1: Carbon fibre weave properties.

Property	Value
Thickness	0.30 mm
Density	1790 kg/m^3
Thermal Conductivity	10.42 W/(m K)
Specific Heat	795 J/(kg K)
Absorptivity	0.85

The carbon fibre weave fabric is in the form of yarns, made of multi-filaments, where the type of weave is taken into consideration according to the application (Tourlonias and Bueno, 2016). The area between the woven yarns are the perforations where the flowing air passes through. This porosity was calculated from data of morphology image (Figure 4.2) by Shams (2013). The average values of perforation area and porosity are 0.147 mm^2 and 4.2%, respectively and will be input as parameters in the thermal modelling depicted in Chapter 5. The cost of this carbon fibre weave fabric was 24 €/m^2.

To assemble the carbon fibre fabric to the prototype, epoxy laminating resin was applied at the corners of the surface to avoid any splitting in the weave and to keep the surface stretched. These corners were attached to a thin wooden frame of specific absorber dimensions (0.145 m x 1.25 m).

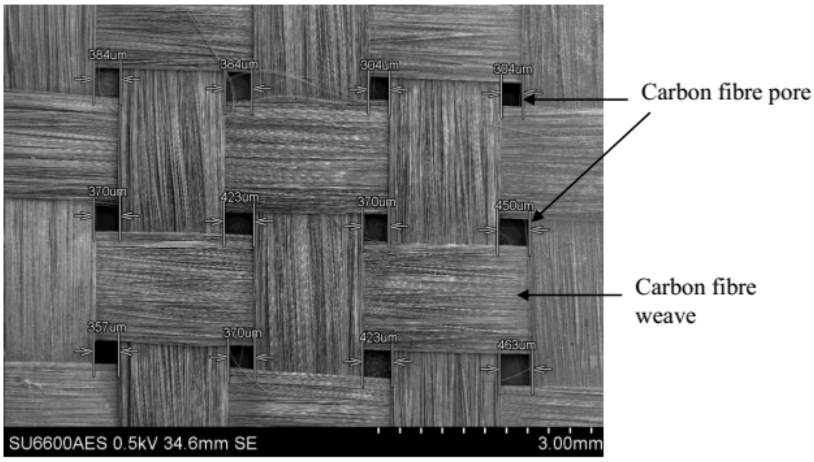

Figure 4.2: Morphology image of carbonfibre sample taken at magnification of 15x.

4.1.2 Glazing cover selection

The function of a glazing surface is to protect the interior of a thermal system from weather conditions (rain, wind, dust accumulation) and suppress thermal losses. However, the solar radiation effectively transmitted to the air heating system is reduced due to absorption and reflection at the glazing cover. Therefore, a glazing material that enhances light transmission and avoid losses is needed. For the task, the selected glazing material for this system is a 4-mm thick tempered clear glass slab. This tempered property enables the glass to be safer and more durable than ordinary glasses. It withstands 5 times more impact before shattering, and, if shattered, the fragments pose a reduced danger to the user, making it an attractive product for use in both commercial and domestic applications (First Glass Ltd, 2016). The glass properties, such as absorptivity and transmittance, are shown in Table 4.2. From the collector's design, the glazing dimensions are 0.27 m x 1.25 m. The cost of the glass was 70 €/m^2.

Table 4.2: Glazing cover properties.

Property	Value
Thickness	4 mm
Density	2500 kg/m^3
Absorptivity[1]	0.02
Transmittance[1]	0.90
Specific Heat	880 J/(kg.K)

4.1.3 Reflector surface selection

The reflective material employed is called *MiroSun* from the German company Alanod, its only product used for solar applications. This reflective aluminium sheet is manufactured using continuous physical vapour deposition (PVD) process applied for a super reflective layer to coil anodized material and afterwards the surface is protected by a nano-composite in a coil-coating process. Table 4.3 shows optical and physical properties of this material. From the concentrator's design, the total area of reflector sheet used was 1.25 m x 1.20 m. The cost of the Alanod reflector was 50 €/m^2.

Table 4.3: *MiroSun* reflector properties (Alanod, 2016).

Property	Value
Thickness	0.5 mm
Density	2700 kg/m^3
Total Reflectivity	0.95

4.1.4 Prototype's structure

The materials used to fabricate the prototype's structure are listed as follows:

✓ 0.7 m^2 of a 2-mm thick aluminium sheet to form the ends;

✓ 8 aluminium bars of 1.25 m in length to support and keep the reflectors in the desired position;

✓ 0.45 m^2 of 1-cm thick timber to form a cavity above the absorber surface in order to reduce heat losses;

✓ two 2.5-in diameter aluminium pipe of 10 cm in length for the airflow inlet and outlet;

✓ 1.8 m^2 of a 0.6-mm thick aluminium sheet to box the whole structure.

Figure 4.3 shows photographs of the assembled structure. The space between the reflectors and the outer aluminium sheet was filled by fibre glass wool to provide thermal insulation. The structure was wrapped with polyurethane foam board and sealed with waterproof tape.

[1] Values at near normal incident light

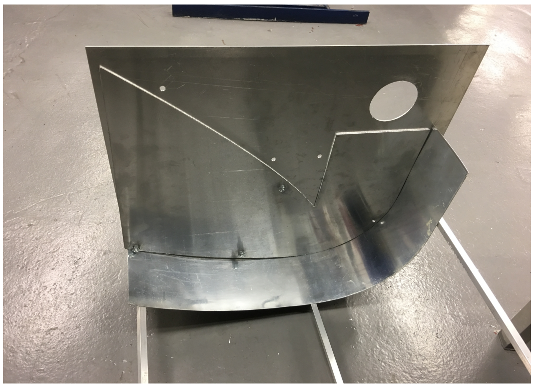

(a) One end assembled.

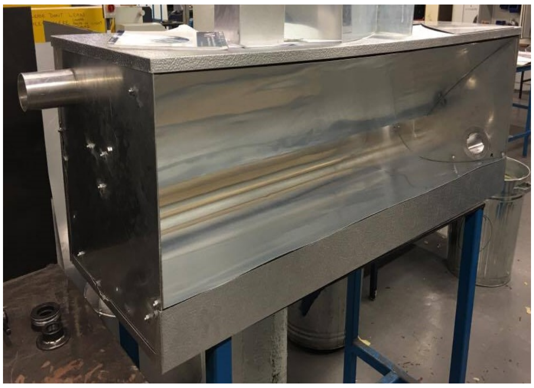

(c) Closed structure.

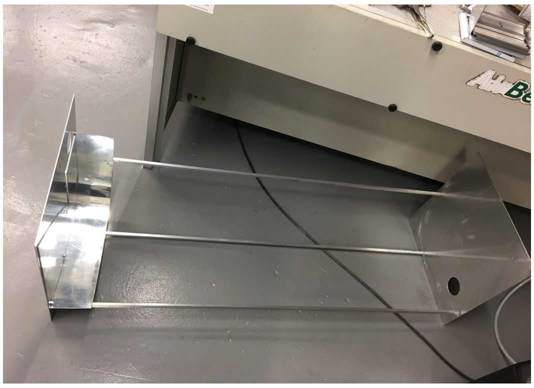

(b) Two ends and aluminium bars assembled.

(d) Closed structure with the glass.

Figure 4.3: Parts of the prototype's structure and assembled

4.2 Instrumentation of the experimental unit

Temperatures were measured at the inlet and outlet of air, absorber and glazing surfaces using type T (Cu-CuNi) PTFE insulated twist fine wire thermocouple sensors with accuracy of $\pm 0.5\ ^{o}C$. Figures 4.4 and 4.5 indicate the position of each thermocouples on the absorber and glazing surfaces, respectively. 18 thermocouples were used in total. As a matter of orientation, in both figures the side where the thermocouple 1 is placed is the closest to the outlet.

These temperature measurements were recorded at 1 minute intervals with a DL2e data logger connected directly to a computer where the temperature data were downloaded via USB port (Delta-T Devices, 2018). All thermocouples were labelled, inserted in a plug and connected to the data logger.

The airflow was provided by a 12-W fan, where the rate was varied by a voltage adaptor with five different voltage inputs. The air velocity at the air outlet (v_{out}) was mea-

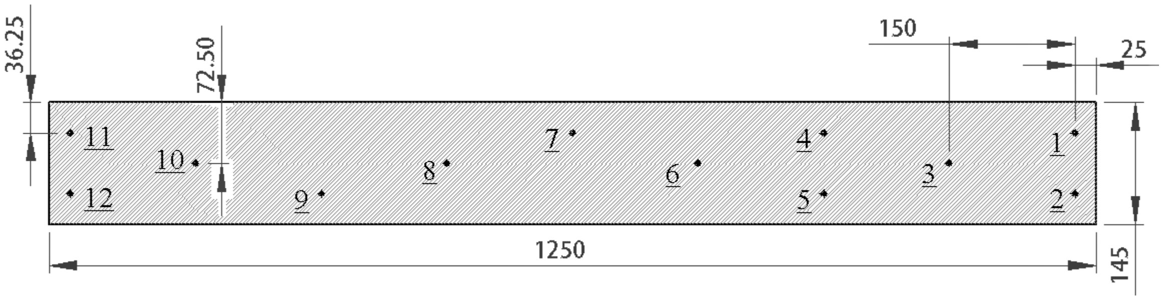

Figure 4.4: Positions of the 12 thermocouples numbered from 1 to 12 placed on the absorber surface (dimensions in mm).

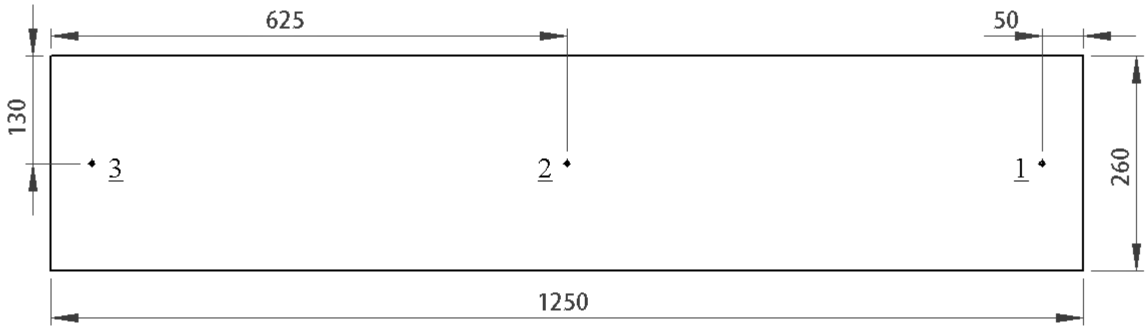

Figure 4.5: Position of the three thermocouples numbered from 1 to 3 placed on the glazing surface (dimensions in mm).

sured using a Testo 425 hot wire anemometer. These airflow conditions were converted to airflow values using Eq. (4.1).

$$G_{air} = \frac{v_{out} A_{out} d_{air}}{A_{abs}} \tag{4.1}$$

where A_{out} is the cross section area of the outlet pipe and A_{abs} is the absorber area.

The measured variables are subjected to systematic uncertainties due to instrumentation errors. It is thus necessary to calculate the standard uncertainty of each variable measured for the experimental work. Those measurements are temperature, air velocity and solar radiation. The accuracy of each instrument, taken from the manufacturer data, are shown in Table 4.4.

Table 4.5 shows the values of air velocity and airflow rate as function of the voltage input (V_a) in terms of mass per absorber area (G_{air}), volume and a category corresponding to each level. Systematic uncertainties were also calculated for the airflow rate (u_g).

Table 4.4: Measurements and standard uncertainty.

Measurement	Accuracy	Uncertainty
Temperature	$\pm 0.55^{o}C \pm 0.3^{o}C$	0.36 ^{o}C
Air velocity	$\pm(0.03 + 5\%$ of $v_{out})$	$0.0173 + 0.0289v_{out}$
Solar radiation	–	1% of I_T

Table 4.5: Mass and volumetric flow rates calculated at each voltage input.

Voltage (V)	v_{out} (m/s)	G_{air} (kg/m^2.s)	u_g (kg/m^2.s)	Code
4.92	1.83	0.038	0.0021	Low
5.82	2.59	0.054	0.0030	Low-med
7.20	3.43	0.071	0.0039	Medium
8.70	4.30	0.089	0.0048	Med-high
11.30	5.50	0.114	0.0060	High

A schematic diagram of the open loop experimental system is shown in Figure 4.6. A flexible duct was connected to the inlet of prototype. Air flowed through the air duct to the collector by the fan. The power supply unit provided voltage to the fan and energy to the data logger. Figure 4.7 presents the prototype's front view. It was fixed to the ground to prevent it from moving due to severe wind conditions. The fan was enclosed and protected from the environment during the experiments and the data logger was placed behind the prototype.

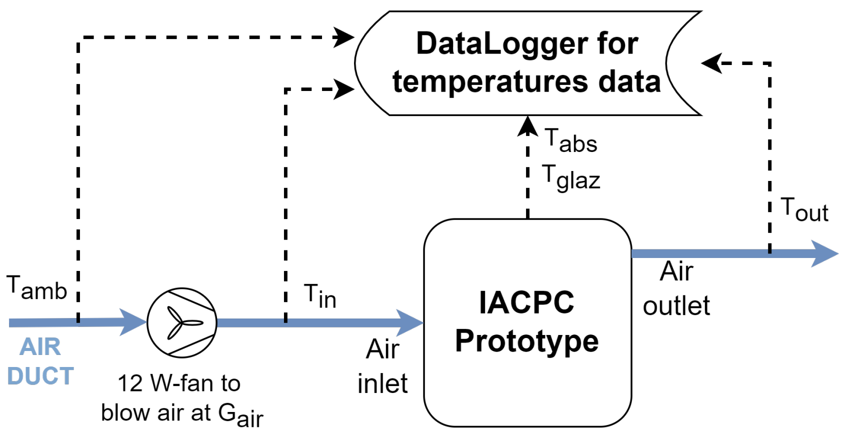

Figure 4.6: Schematic diagram of the experimental unit.

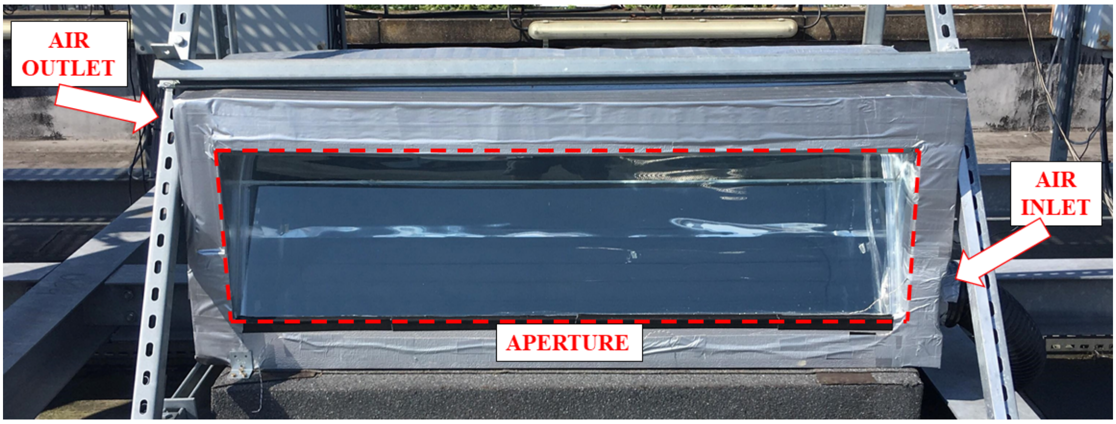

Figure 4.7: Open loop outdoor experimental unit.

4.3 Experimental results from the air heating prototype

This section presents the experimental results from tests conducted at the five airflow rates and also the ones with no flow. The thermal performance of the prototype focused on evaluating the useful energy rate (or energy delivered), collector thermal efficiency and outlet air temperature. The useful heat rate transferred to the airflow is estimated by Eq. (4.2) (Kalogirou, 2004) using temperature measurements from the inlet and outlet:

$$Q_u = G_{air} A_{abs} C_{p,air} (T_{out} - T_{in}) \tag{4.2}$$

The thermal efficiency, which is the ratio of useful heat rate to the incoming total solar radiation on the aperture, is calculated by Eq. (4.3). Such efficiency can be evaluated either instantaneously or as an average over a certain period of time (Goswami, 2015):

$$\eta_{th} = \frac{Q_u}{I_T A_{apt}} \tag{4.3}$$

where I_T is the total incoming solar radiation. The solar data used in the calculations were downloaded from the Met Eireann website (Met Eireann, 2018). Such data were measured by a solar pyranometer placed at the horizontal.

4.3.1 Experimental results at transient state

Experimental results of measured temperatures and solar radiation were used to calculate energies and thermal efficiency on hourly basis. One day of each level of airflow rate was taken for data treatment and discussion, from 9:00 to 17:00 in 2018.

4.3.1.1 Experimental results at zero airflow

The equilibrium temperature that the absorber approaches when no energy is removed from the collector is called stagnation temperature (Rabl, 1985). In order to verify this condition, the inlet and outlet of the system were closed and two tests at clear sky days were performed on 2nd and 3rd July as shown in Figure 4.8. The maximum stagnation absorber temperature reached 77 °C in both tests at an average I_T of 820 W/m^2 and T_{amb} of 22 °C.

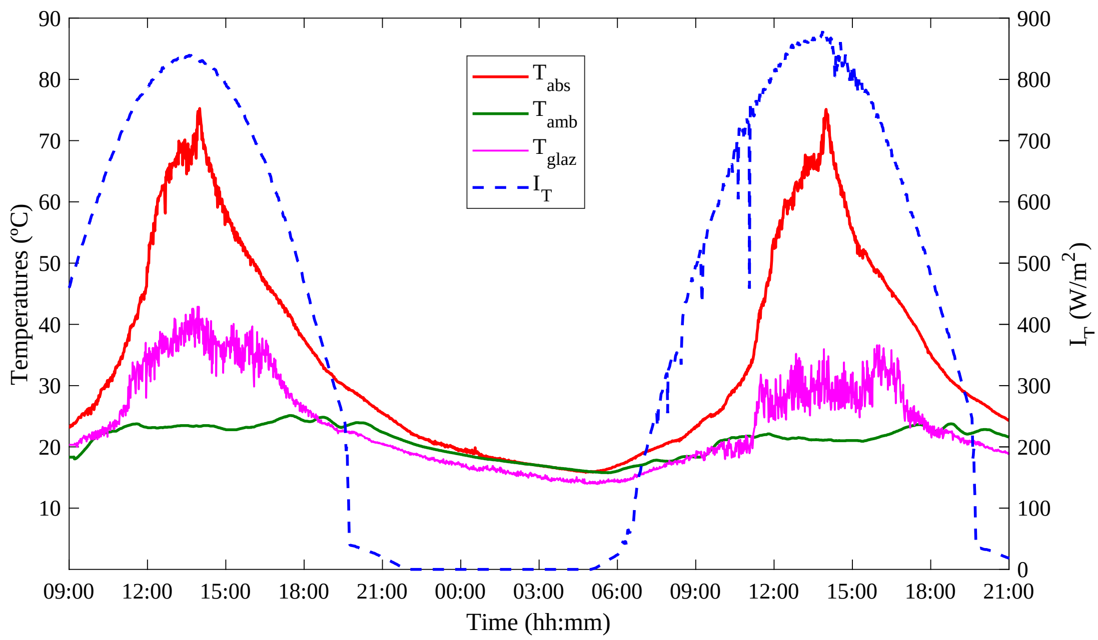

Figure 4.8: Experimental results from 2nd and 3rd July at zero airflow.

4.3.1.2 Experimental results with airflow

The findings of a low airflow rate (0.038 kg/m^2.s) experiment are presented in Figure 4.9. It was conducted on June 9th under clear sky conditions with highest values of solar radiation at the solar noon hour (13:00 – 14:00), where its peak is 860 W/m^2. During this hour, the average outlet airflow temperature T_{out}, ambient temperature T_{amb}, and thermal efficiency η_{th} were observed to have average values of 51 °C, 23 °C, and 0.53, respectively. At around the peak of solar radiation, the maximum T_{out} was found to be 51 °C, resulting in an airflow temperature rise of 28 °C and a corresponding η_{th} of 0.54. The total incident solar radiation received during the test was estimated to be 20.46 MJ/m^2, of which a total useful energy collected Q_u of 7.64 MJ/m^2 was calculated, resulting in a daily thermal efficiency of 0.35.

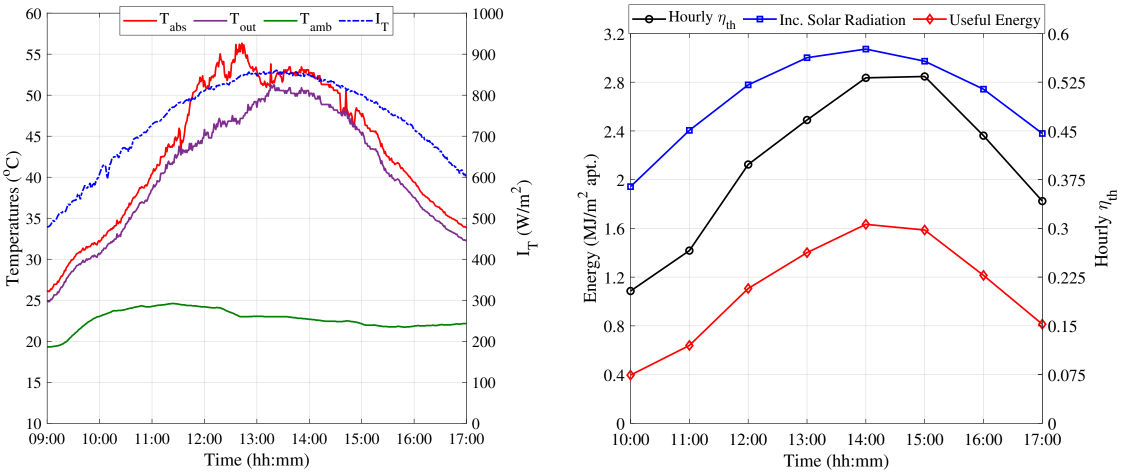

(a) Temperature results and solar data. (b) Hourly performance and solar data.

Figure 4.9: Experimental results from 9th June at 0.038 kg/(s m^2).

The results of an experiment conducted at a low-medium airflow rate (0.055 kg/m^2.s) under relatively clear sky conditions are depicted in Figure 4.10. During the solar noon hour (13:00 – 14:00), the airflow collected 1.7 MJ/m^2 of energy at an average outlet temperature of 43 °C and thermal efficiency of 55%. The highest outlet temperature (T_{out}) was recorded as 42 °C when the ambient temperature (T_{amb}) was 20 °C, resulting in the maximum temperature rise of 22 °C. The total solar energy available was 21.29 MJ/m^2, while the total useful energy collected was 9.56 MJ/m^2. The thermal efficiency obtained for this day was 43%.

The experimental results of the test operating at medium airflow (0.07 kg/m^2.s) is shown in Figure 4.11 on 29th May, in relatively clear sky condition. The highest T_{out} was measured to be 41 °C when T_{amb} was 21 °C. The maximum airflow temperature rise was 20 °C observed between 13:00 and 14:00. The thermal efficiency (η_{th}) on this same region

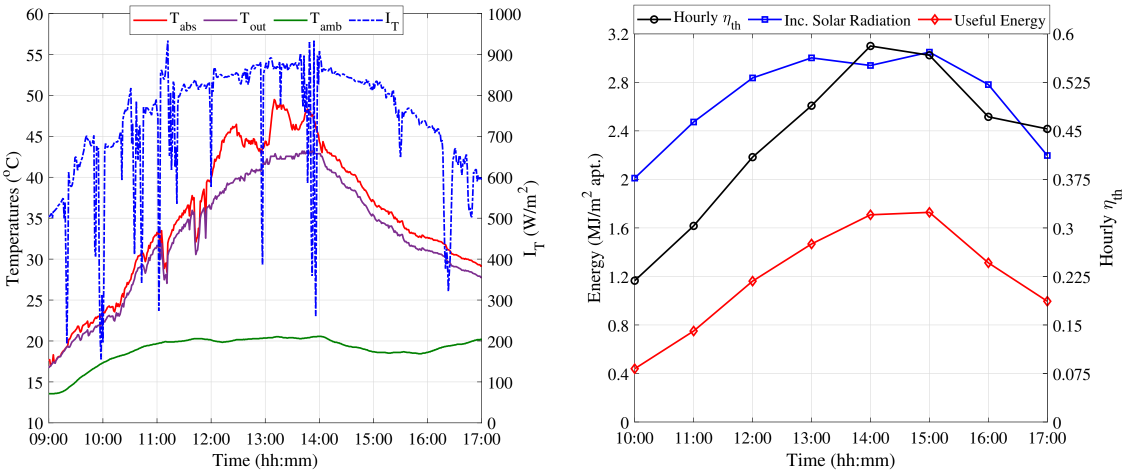

(a) Temperature results and solar data. (b) Hourly performance and solar data.

Figure 4.10: Experimental results from 22nd June at 0.054 kg/(s m^2).

was 58%. The total incident solar energy available on this day was 21.4 MJ/m^2; the total useful energy collected was 10.03 MJ/m^2; and the average thermal efficiency obtained was 46%. In the hour of highest solar radiation, the airflow collected 1.7 MJ/m^2 of energy at an average T_{out} of 40 °C.

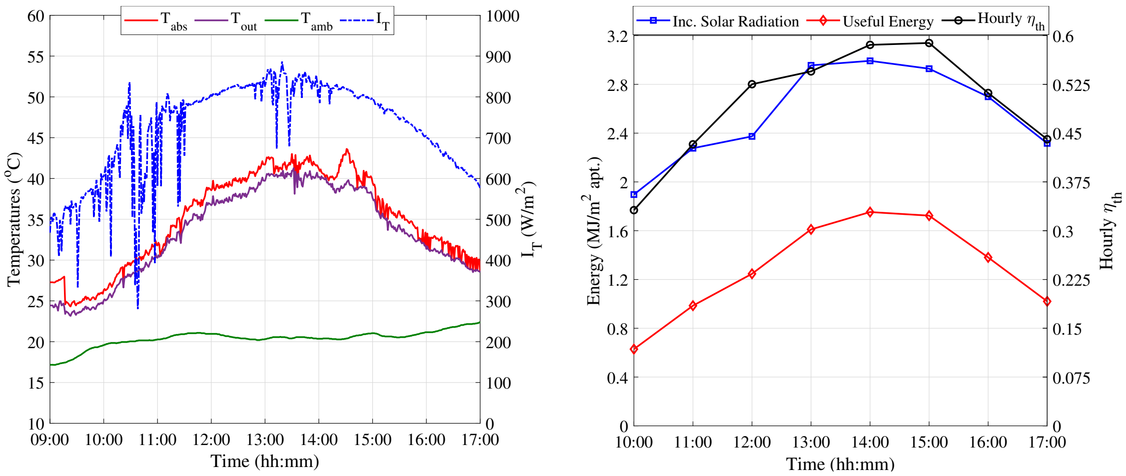

(a) Temperature results and solar data. (b) Hourly performance and solar data.

Figure 4.11: Experimental results from 29th May at 0.071 kg/(s m^2).

The results of the test at med-high airflow (0.089 kg/m^2.s) are shown in Figure 4.12 on 31st May. Although the solar data is very transient on this day, T_{out} kept constant around 39 °C when T_{amb} was 23 °C at solar noon hour. The maximum airflow temperature rise was 16 °C at the same hour. The thermal efficiency on this same region was 59%. The total solar radiation available was 15.6 MJ/m^2; Q_u was 7.18 MJ/m^2; and the average thermal efficiency obtained was 46%. In the hour of highest solar radiation, the airflow collected 1.6 MJ/m^2 of energy at an average T_{out} of 39 ^{o}C.

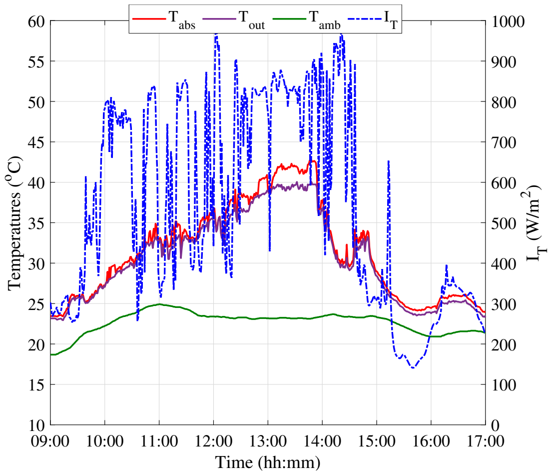

(a) Temperature results and solar data.

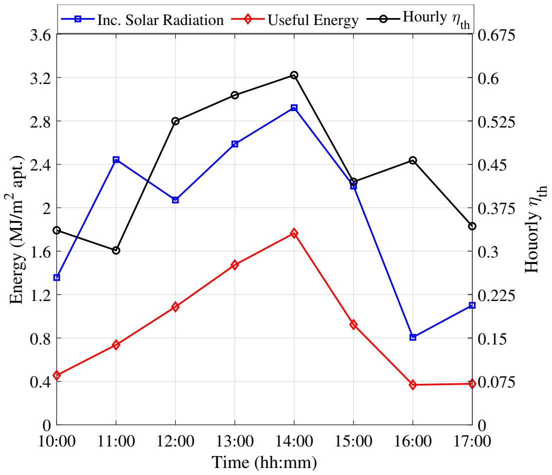

(b) Hourly performance and solar data.

Figure 4.12: Experimental results from 31st May at 0.089 kg/(s m^2).

The results of a high airflow rate (0.114 kg/m^2.s) experiment are presented in Figure 4.13. It was tested on June 28th under clear sky conditions with highest values of solar radiation at the expected solar noon hour, where its peak was 850 W/m^2. During this hour, the average values of T_{out}, T_{amb}, and η_{th} were 38 ^{o}C, 27 ^{o}C, and 0.62, respectively. At around the peak of solar radiation, the maximum T_{out} was found to be 39 ^{o}C, resulting in the maximum airflow temperature rise of 12 ^{o}C and a corresponding η_{th} of 0.65. The total incident solar radiation during the test was estimated to be 21.07 MJ/m^2, of which a total useful energy collected Q_u was 9.8 MJ/m^2, resulting in a daily thermal efficiency of 0.47.

4.3.2 Experimental characterisation at nearly steady state

The thermal characterisation of a solar air heating relates the thermal efficiency under steady state to each temperature rise normalised by the corresponding solar radiation according to the Hottel-Whillier-Bliss equation, expressed by Eq. (4.4).

$$\eta_{th} = F_R \eta_o - F_R U_L \frac{(T_{out} - T_{amb})}{I_T} \tag{4.4}$$

where U_L is the system's overall heat loss coefficient and F_R is the heat removal factor. From this equation, η_{th} can be plotted against $(T_{out} - T_{amb})/I_T$, resulting in a linear curve,

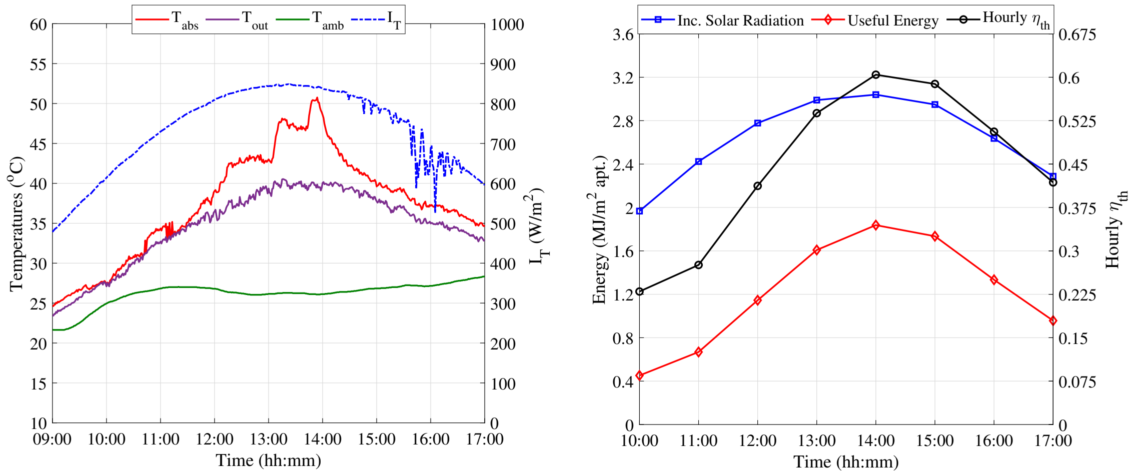

(a) Temperature results and solar data. (b) Hourly performance and solar data.

Figure 4.13: Experimental results from 28$^{\text{th}}$ June at 0.114 kg/(s m^2).

with $F_R\eta_o$ and $-F_R U_L$ as the linear coefficient and the slope, respectively (Goswami, 2015).

The experimental data collected for this analysis were during 10 minutes of tests around the solar noon period of clear days (nearly steady state condition), including all the five airflow rates. This is the period where the direct radiation range is at maximum, which was 800 – 900 W/m^2. To minimise the effects of the system's heat capacity, the data were taken in nearly symmetrical pairs, one before and one after noon, thus resulting in five averaged pairs for each day of experimental tests (Duffie and Beckman, 2013). Thermal efficiency was calculated by Eq. (4.3). With all the data collected, the thermal efficiency curve was plotted in Figure 4.14.

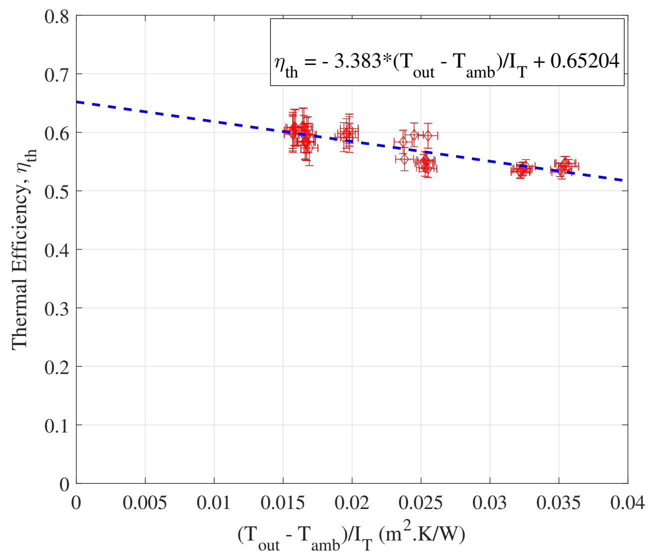

Figure 4.14: Hottel-Whillier-Bliss collector characterisation.

From these results, the parameters of Eq. (4.4) were calculated: $F_R\eta_o$ and F_RU_L are 0.652 ± 0.008 and -3.383 ± 0.328 respectively, and the coefficient of correlation is 0.8. It is important to state that U_L is assumed to be weakly dependent on the absorber temperature in this operational range, where $(T_{out} - T_{amb})/I_T$ is between 0.015 and 0.037 $m^2.^oC/W$, so that the heat loss coefficient is constant (Rabl, 1985). Comparing to other work, Shams et al. (2016) characterised experimentally a solar air heating system with a similar geometry. For this, they calculated the instantaneous thermal efficiency when the solar radiation varied between 937.6 and 1,085.4 W/m^2. This resulted in a linear coefficient ($F_R\eta_o$) of 0.73 and slope (F_RU_L) of -3.25 W/$m^2.^oC$.

Next, Figure 4.15 shows thermal efficiency and outlet air temperature as functions of the mass airflow rate. From the thermal efficiency graph, it is possible to view a smooth increase in η_{th} when G_{air} becomes higher. The opposite behaviour is observed in the airflow temperature rise $(T_{out} - T_{in})$, where this variable drops dramatically when G_{air} varies from 0.04 to 0.09 kg/m^2.s and then falls smoothly by 2 ^oC.

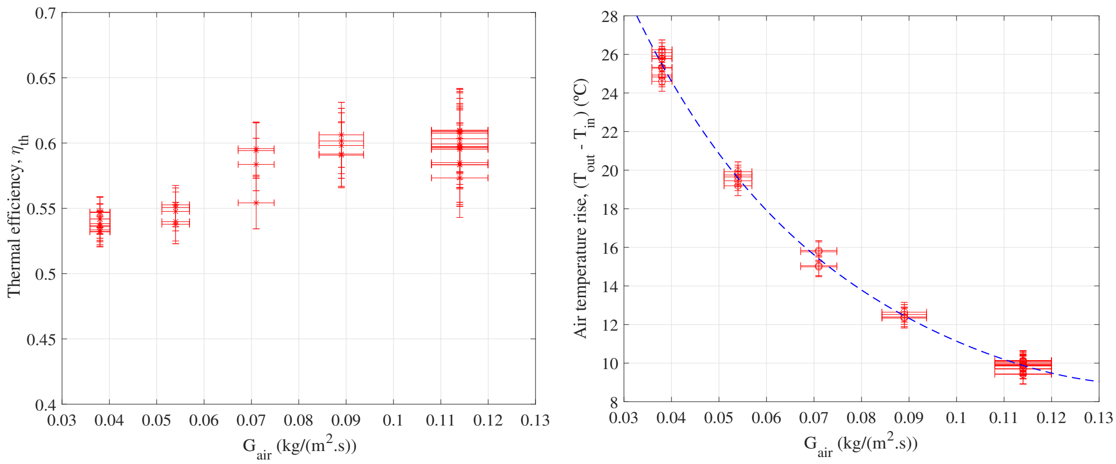

(a) η_{th} vs. G_{air}. (b) $(T_{out} - T_{in})$ vs. G_{air}.

Figure 4.15: Graphs of thermal efficiency (a), and airflow temperature rise (b) at different airflow rates at nearly steady state condition.

4.4 Chapter summary

The fabrication of a solar air heating prototype for outdoor experimental tests has been detailed in this chapter. This chapter outlined the selection of materials, fabrication process of the system and the data collection apparatus. Carbon fibre weave with 85% absorptivity was selected as the absorber material for the collector considering its properties of the material and the inherent perforation. 95% reflectivity *Mirosun* reflector sheet from the company ‘Alanod’ was selected as the reflector material. Tempered clear glass of 4 mm in thickness with 90% transmittance was selected as the glazing cover.

The experiments were carried out in open loop configuration, where the air was blown by a 12-W fan with a voltage adaptor to vary the airflow rate. Experimental results were analysed for different airflow rates ranging between 0.04 and 0.115 kg/m^2.s. Results show that the maximum outlet air temperatures at solar noon (13:00 to 14:00) varied from 40 ^{o}C at the highest airflow to 52 ^{o}C at the lowest and the thermal efficiency varied from 52% to 62%.

Results were also evaluated at nearly steady state condition, period where the direct radiation range is at maximum at solar noon, which was 800 – 900 W/m^2. It was possible to plot the thermal efficiency curve in order to characterise the system. The parameters of the Hottel-Whillier-Bliss equation were calculated, where $F_R\eta_o$ and F_RU_L are 0.65 and -3.39 respectively. The air temperature rise varied from 10 ^{o}C at the highest airflow rate to 26 ^{o}C at the lowest.

CHAPTER 5

HEAT TRANSFER MODELLING AND SIMULATION

It is desirable to analyse theoretically a new solar energy, any given system before the prototype fabrication (Tchinda, 2008). A thermal model for simulation of a solar air heater is an important tool to predict its long-term performance under different weather conditions (Shams, 2013). Therefore, this chapter aims to:

1. develop a heat transfer model to simulate the thermal performance of the proposed solar air heater, when in operation;
2. validate the model against experimental data from the tests described in Chapter 4.
3. determine how to operate and control the collector based on model.

Consequently, the specific objectives of this chapter are to:

✓ simulate the collector under different solar radiation levels and airflow rates;

✓ estimate outlet airflow temperatures;

✓ evaluate the system's thermal efficiency;

✓ determine useful energy delivered to the airflow;

The model will be employed to gain an insight and understanding of the interactions between system inputs and outputs shown in Figure 5.1. The model algorithm implemented for simulation was created to predict behaviour under transient state conditions.

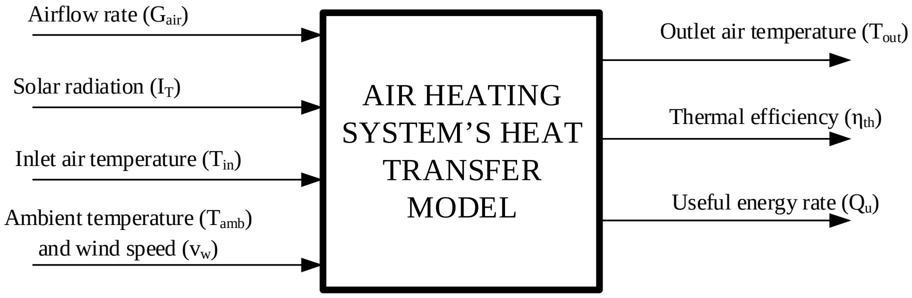

Figure 5.1: Block diagram of the heat transfer model.

5.1 Solar air heating collector's heat transfer modelling

The first step for modelling the solar air heating system is to establish what are the collector's components to be modelled for simulation. In this case there are three: the first one is the absorber surface, the second one is the glazing cover, and the last one is the airflow inside the collector. The next step is to state assumptions in order to simplify the model, which are listed as follows:

✓ Solar radiation is incident uniformly over the components' surfaces;

✓ Absorber and glazing temperatures are uniform;

✓ Thermal and physical properties of the components are independent of temperature;

✓ Heat transfer at the reflectors and wooden cavity, and conduction losses are neglected;

✓ Airflow rate is uniform through all the absorber holes;

The following step of the modelling depicts how the energy balance in the components are evaluated according to the following statements:

$$\begin{pmatrix} \text{Rate of} \\ \text{internal energy} \\ \text{in the absorber} \end{pmatrix} = \begin{pmatrix} \text{Absorbed solar} \\ \text{radiation in} \\ \text{the absorber} \end{pmatrix} - \begin{pmatrix} \text{Heat losses} \\ \text{from absorber} \end{pmatrix} - \begin{pmatrix} \text{Useful heat} \\ \text{rate to airflow} \end{pmatrix}$$

$$\begin{pmatrix} \text{Rate of} \\ \text{internal energy} \\ \text{in the glazing} \end{pmatrix} = \begin{pmatrix} \text{Absorbed solar} \\ \text{radiation in} \\ \text{the glazing} \end{pmatrix} + \begin{pmatrix} \text{Heat losses} \\ \text{from absorber} \end{pmatrix} - \begin{pmatrix} \text{Heat losses} \\ \text{from glazing} \end{pmatrix}$$

$$\begin{pmatrix} \text{Rate of} \\ \text{useful energy} \\ \text{in the airflow} \end{pmatrix} = \begin{pmatrix} \text{Convective heat} \\ \text{transfer from the} \\ \text{absorber plate} \end{pmatrix} - \begin{pmatrix} \text{Heat losses} \\ \text{from airflow} \\ \text{to the glazing} \end{pmatrix}$$

where the heat losses are convective and radiative. In order to visualise how these heat rates are placed, Figure 5.2 presents the collector's thermal network as an analogy to an electric circuit, where absorber, glazing and air inside the collector are nodes. The energy input here is the total solar radiation I_T, and mathematical expressions above each resistor were used to calculate the thermal resistances.

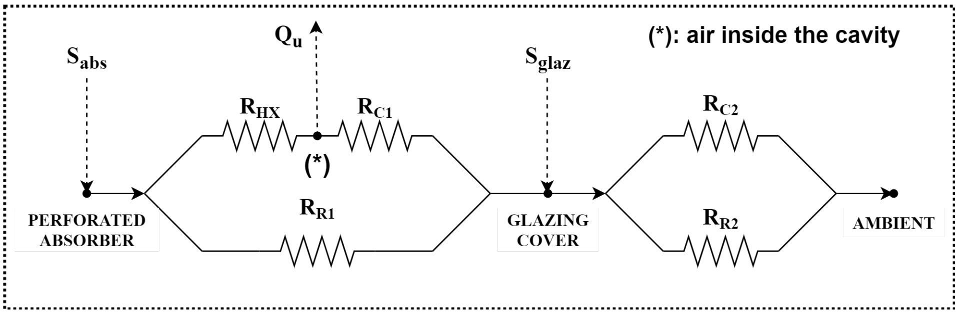

Figure 5.2: Thermal network to illustrate heat flows in the air heater, where the subscripts C and R refer to convection and radiation, respectively.

From the absorber node, the circuit path to the the right is the path of heat transfer to the airflow (upper path) and radiative (lower path) heat losses. At the upper path there is also the convective resistance from the airflow to the glazing indicating that there is convective loss inside the collector. Similarly there are losses from glazing to the ambient indicated by the thermal resistances to the right of its node. These heat transfer types will be addressed later. Applying the concept of heat loss rate as the ratio of temperature difference to the corresponding thermal resistance:

$$M_{abs}C_{p,abs}\frac{dT_{abs}}{dt} = S_{abs} - \left(\frac{T_{abs}-T_{air}}{R_{HX}} + \frac{T_{abs}-T_{glaz}}{R_{R1}}\right) \tag{5.1}$$

$$M_{glaz}C_{p,glaz}\frac{dT_{glaz}}{dt} = S_{glaz} + \left(\frac{T_{air}-T_{glaz}}{R_{C1}} + \frac{T_{abs}-T_{glaz}}{R_{R1}}\right) - \frac{T_{glaz}-T_{amb}}{\left(\frac{1}{R_{C2}}+\frac{1}{R_{R2}}\right)^{-1}} \tag{5.2}$$

$$G_{air}A_{abs}C_{p,air}\frac{dT_{air}}{dt} = \frac{(T_{abs} - T_{air})}{R_{HX}} - \frac{(T_{air} - T_{glaz})}{R_{C1}} \tag{5.3}$$

Substituting the thermal resistances by the mathematical expressions properly and isolating the derivative terms, Eqs. (5.4), Eq. (5.5) and Eq. (5.6) are obtained.

$$\frac{dT_{abs}}{dt} = \frac{1}{M_{abs}C_{p,abs}}\left[S_{abs} - h_{R1}A_{abs}(T_{abs} - T_{glaz}) - h_{HX}A_{abs}(T_{abs} - T_{air})\right] \tag{5.4}$$

$$\frac{dT_{glaz}}{dt} = \frac{1}{M_{glaz}C_{p,glaz}}\begin{bmatrix} S_{glaz} + h_{R1}A_{abs}(T_{abs} - T_{glaz}) + h_{C1}A_{abs}(T_{air} - T_{glaz}) \\ -(h_{R2} + h_{C2})A_{glaz}(T_{glaz} - T_{amb}) \end{bmatrix} \tag{5.5}$$

$$G_{air}A_{abs}C_{p,air}\frac{dT_{air}}{dt} = h_{HX}A_{abs}(T_{abs} - T_{air}) - h_{C1}A_{abs}(T_{air} - T_{glaz}) \tag{5.6}$$

The next subsections describe how the absorbed solar radiation terms, convective and radiative heat transfer coefficients, useful energy rate and outlet air temperature from the thermal model were determined.

5.1.1 Absorbed solar radiation terms

The portion of total solar radiation undergoes optical losses before it reaches the absorber – expressed in terms of η_0 and previously discussed in Chapters 2 and 3. Hence, S_{abs} is given by Eq. (5.7).

$$S_{abs} = I_T\xi A_{apt}\eta_0 \tag{5.7}$$

The absorbed solar radiation by the glazing, which is based on the capacity of this component to retain the incoming radiation incident on the aperture, can be expressed as:

$$S_{glaz} = I_T A_{apt}\alpha_{glaz} \tag{5.8}$$

where the glazing absorptivity α_{glaz} was also estimated in Chapter 3.

5.1.2 Radiative heat transfer coefficients

The radiative heat transfer coefficient from the absorber to the glazing h_{R1} can be evaluated by Eq. (5.9):

$$h_{R1} = \varepsilon_{\text{eff}}\sigma\left(T_{\text{abs}}^2 + T_{\text{glaz}}^2\right)\left(T_{\text{abs}} + T_{\text{glaz}}\right) \tag{5.9}$$

where ε_{eff} is the effective emissivity, a radiative property developed by Rabl (1976b) for a CPC comprised by specular reflectors. Although the solar air heater to be modelled here is not a simple CPC, such methodology of assessing h_{R1} was used, given the similarity of both geometries. The calculation of ε_{eff} takes into account: the radiative properties of the absorber, reflector and glazing, such as emissivity and reflectivity, and the concentrator's geometric concentration ratio.

The radiative heat transfer coefficient from the glazing to the ambient h_{R2} was evaluated by Eq. (5.10):

$$h_{R2} = \varepsilon_{\text{glaz}}\sigma\left(T_{\text{glaz}}^2 + T_{\text{amb}}^2\right)\left(T_{\text{glaz}} + T_{\text{amb}}\right) \tag{5.10}$$

where the glazing is considered to emit radiation to the ambient only, which absorbs all the emitted energy from that, thus acting as a blackbody (Duffie and Beckman, 2013).

5.1.3 Convective heat transfer coefficients

In order to calculate the heat transfer coefficient from airflow to glazing h_{C1}, it is assumed that the airflow circulating within the collector loses part of its thermal energy to the glazing by convection. Therefore, the estimation of h_{C1} is given by Eq. (5.11) (Zheng et al., 2016):

$$h_{C1} = \frac{k_{\text{air}}}{L_{\text{col}}}Nu_{C1} = \frac{k_{\text{air}}}{L_{\text{col}}}\left(0.664Re_{C1}^{1/2}Pr^{1/3}\right) \tag{5.11}$$

where it is assumed that the air thermal properties are evaluated at the average between T_{abs} and T_{in}; the Reynolds number based on the air velocity at the inlet (v_{in}) is:

$$\mathrm{Re}_{C1} = \frac{v_{in} L_{col}}{\nu_{air}} \tag{5.12}$$

In order to calculate the heat transfer coefficient from glazing to ambient h_{C2}, it is assumed that the convection loss is forced by the wind. Therefore, the estimation of it is given by Eq. (5.13) (Tchinda, 2008):

$$h_{C2} = 2.8 + 3 v_w \tag{5.13}$$

The convective heat transfer coefficient for the air flowing through a perforated plate (h_{HX}) is calculated by the correlation developed by Kutscher (1994) for a normal flow:

$$h_{HX} = \frac{k_{air}}{\varphi_h} \mathrm{Nu}_h = \frac{k_{air}}{\varphi_h}\left[2.75\left(\frac{\ell}{\varphi_h}\right)^{-1.2} \mathrm{Re}_h^{0.43}\right] \tag{5.14}$$

where the hole pitch and the hole diameter at the absorber are calculated based on the hole area A_h in Eqs. (5.15) and (5.16), respectively, whereas Figure 5.3 illustrates a drawing of carbon fibre fabric to indicate the geometry parameters used in the modelling.

$$\ell = \sqrt{\frac{A_h}{\varphi_p}} \tag{5.15}$$

$$\varphi_h = \sqrt{A_h} \tag{5.16}$$

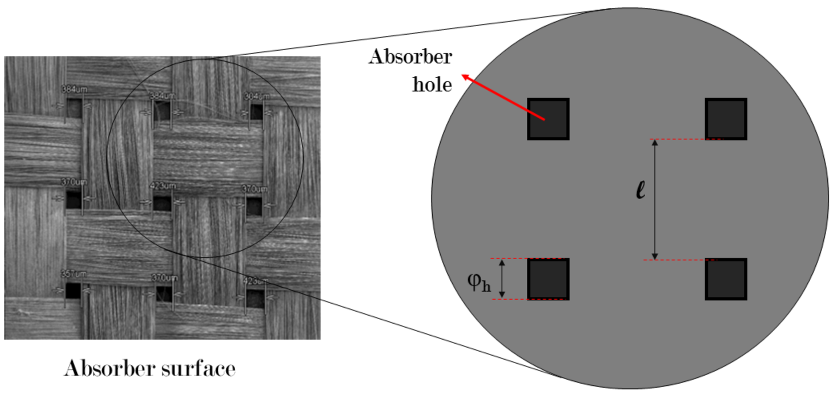

Figure 5.3: Carbon fibre magnified image and drawing for indication of geometric parameters.

Furthermore, the Reynolds number in the holes is:

$$Re_h = \frac{v_h \varphi_h}{\nu_{air}} \tag{5.17}$$

with the average air velocity in the holes as:

$$v_h = \frac{G_{air}}{d_{air} \varphi_p} \tag{5.18}$$

where the air physical properties d_{air}, k_{air} and ν_{air} were evaluated at a temperature assumed to be the average between T_{in} and T_{out} so the value of h_{HX} could be estimated.

The useful energy rate Q_u was given in Eq. (4.2). It should be noted that the outlet air temperature is unknown in the modelling. Therefore, understanding heat transfer from the absorber to the airflow becomes necessary to estimate T_{out}. One way of assessing this temperature is finding T_{air} by solving the energy balance equations and assuming that as the average between inlet and outlet temperatures.

5.2 Simulation results and model validation

5.2.1 Simulation settings

After describing all the variables and parameters, the method for solving the system of two ordinary differential equations (ODEs) must be defined, which is the explicit Euler method for initial condition. It derives from the Taylor series truncated at the second term where the solution of the model is fairly accurate for small values of time step Δt (Hoffman, 2001). The ODEs system is then shown in Eq. (5.19):

$$\begin{cases} T_{abs}(t_{m+1}) = T_{abs}(t_m) + \Delta t \cdot f_1(T_{abs}(t_m), T_{glaz}(t_m), T_{air}(t_m)) \\ T_{glaz}(t_{m+1}) = T_{glaz}(t_m) + \Delta t \cdot f_2(T_{abs}(t_m), T_{glaz}(t_m), T_{air}(t_m)) \\ T_{air}(t_{m+1}) = T_{air}(t_m) + \Delta t \cdot f_3(T_{abs}(t_m), T_{glaz}(t_m), T_{air}(t_m)) \end{cases} \tag{5.19}$$

where the functions f_1, f_2 and f_3 are the right hand sides of Eqs. (5.4), (5.5) and (5.6), respectively. The initial conditions are the data collected at 9 am of each day of experiment and the time step Δt was set as 1 s. The algorithm used for modelling and simulation was implemented in Matlab® and it followed the steps depicted as follows:

Step 1: Input geometric parameters, optical efficiency data (η_0) and the components' physical properties;

Step 2: Input solar radiation (I_T), ambient temperature (T_{amb}), inlet air temperature (T_{in}) and wind speed (v_w) data;

Step 3: Set time step (Δt), simulation time (t_s = 8h), initial conditions and initiate time index m = 1;

Step 4: Run current time (t_m);

Step 5: Calculate the terms S_{abs}, S_{glaz}, h_{R1}, h_{R2}, h_{C1}, h_{C2} and h_{HX};

Step 6: Calculate $T_{abs}(t_{m+1})$, $T_{glaz}(t_{m+1})$ and $T_{air}(t_{m+1})$;

Step 7: Calculate $T_{out}(t_{m+1})$ and $Q_u(t_m)$;

Step 8: Check if t_{m+1} is the final time. If so, end the simulation. If not, do m = m + 1 and go back to step 4.

Table 5.1: Model parameters values used in the heat transfer modelling.

Symbol	Model parameter	Value
$C_{p,abs}$	Absorber heat capacity	1000 J/(kg K)
M_{abs}	Absorber mass	0.075 kg
A'_{abs}	Absorber area without holes	0.17 m^2
φ_p	Carbon fibre porosity	4.19%
A_h	Hole area	0.147 mm^2
ℓ	Hole pitch	1.87 mm
φ_h	Hole diameter	0.383 mm
$C_{p,glaz}$	Glazing heat capacity	880 J/(kg K)
M_{glaz}	Glazing mass	3.7 kg
n_{glaz}	Glazing refraction index	1.526
K_{ext}	Glaz. extinction coefficient	4 m^{-1}
$\overline{W}_{glaz}$	Glaz. characteristic length	0.11 m
ε_{eff}	Effective emissivity	0.68
$C_{p,air}$	Air heat capacity	1000 J/(kg K)
Pr	Prandtl number	0.72
ξ	Intercept factor	0.93
Δt	Time step	1 s

The experimental data were used to validate the heat transfer model. The purpose of validation is to determine if the model is an accurate representation of this air heating system (Banks and Carson, 1987). In order to measure the model accuracy in predicting experimental data, an error estimator was used: the mean absolute error (MAE), defined as the percentage mean of absolute errors relative to individual observations. Such estimator is calculated by Eq. (5.20)(Pujol-Nadal et al., 2015):

$$\mathrm{MAE}(\%) = \frac{100}{N_{obs}} \sum_{i=1}^{N_{obs}} \left| \frac{X_{exp,i} - X_{sim,i}}{X_{exp,i}} \right| \tag{5.20}$$

where $X_{exp,i}$ is the experimental (observed) value and $X_{sim,i}$ is the simulated (estimated) value of the same variable. Another way to measure accuracy is to assess the frequency and magnitude of residues (difference between experimental and simulated values) generated by the mathematical model. A positive residue indicates model underestimation while a negative one indicates overestimation.

5.2.2 Model validation

The model validation consisted of comparing the simulated variables T_{out} and Q_u to the experimental ones under the same conditions of the experimental results presented in Chapter 4.

5.2.2.1 Validation of results at low airflow rate

Figure 5.4(a) shows the graphs of solar radiation data, experimental and simulated results of the test on 9th June (G_{air} = 0.04 kg/m^2.s), whereas Figures 5.4(b) and 5.4(c) present the residue plot in relation to the simulated values. On this clear sky day the calculated MAE for T_{out} and Q_u are 1.9% and 5.3%, respectively. During the hour of highest solar radiation (13:00 – 14:00) the residues are mostly between ±1 ^{o}C and ±20 W/m^2. It was found that 70% of the residues have magnitude of ±1 ^{o}C; 80% are between ±20 W/m^2 and 60% of the predictions are underestimated (positive residues).

5.2.2.2 Validation of results at low-med airflow rate

Figure 5.5(a) shows solar radiation, experimental and simulated data of the test on 22nd June (G_{air} = 0.055 kg/(s m^2)). On this clear sky day with intermittent clouds, the calculated MAE regarding T_{out} and Q_u are 2.2% and 6.0%, respectively. Although it was

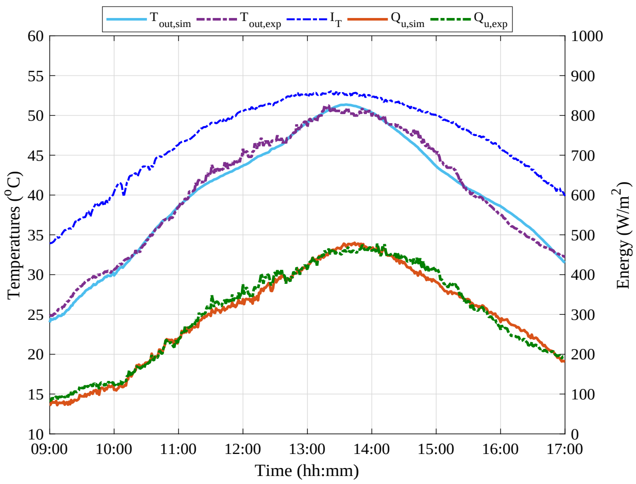

(a) Experimental and simulated results over time.

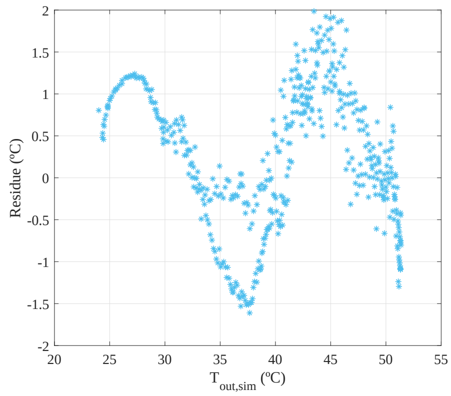

(b) Residue vs. simulated T_{out}.

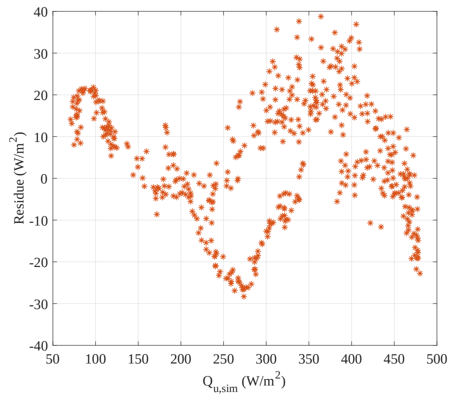

(c) Residue vs. simulated Q_u.

Figure 5.4: (a) Experimental and simulated results, (b) residues of T_{out}, and (c) residues of Q_u from 09th June at 0.04 kg/(s m^2).

a day with sudden variation in solar radiation at different moments, the model predicted the outputs which most of the residues are between -0.5 and 1 °C, and -10 and 30 W/m^2, except in two periods: after 16:00, when the decay of I_T lasted 10 minutes before rising to the natural trend; and shortly before 14:00, when I_T became highly unstable. These events might explain why the model underestimated the outputs by more than 1.5 °C and 30 W/m^2. From Figures 5.5(b) and 5.5(c), 85% of the residues have magnitude of ±1 °C; 90% of the residues are between ±30 W/m^2 and 88% of the predictions are underestimated.

5.2.2.3 Validation of results at medium airflow rate

Figure 5.6(a) shows the graphs of solar radiation data, experimental and simulated results of the test on 29th May (G_{air} = 0.07 kg/m^2.s), whereas Figures 5.6(b) and 5.6(c) present the residue plot in relation to the simulated values. On this clear sky day with

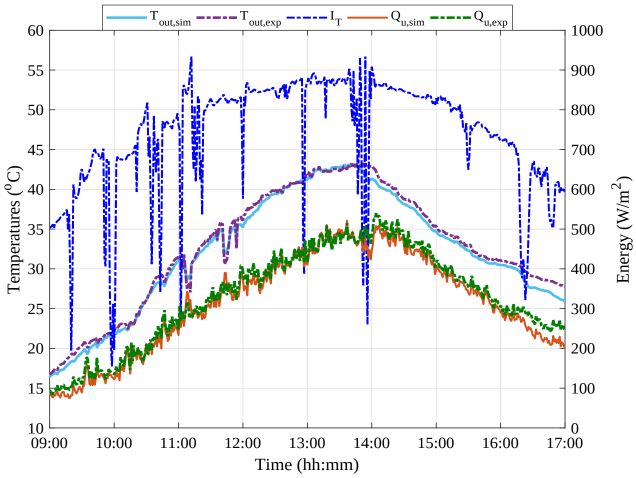

(a) Experimental and simulated results over time.

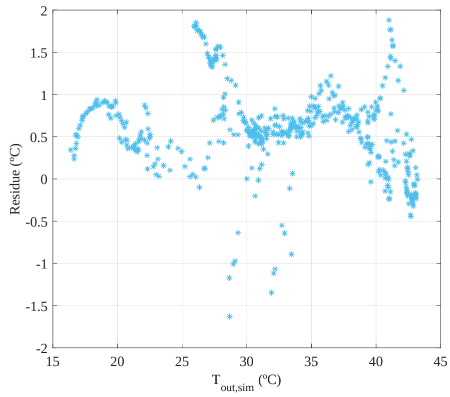

(b) Residue vs. simulated T_{out}.

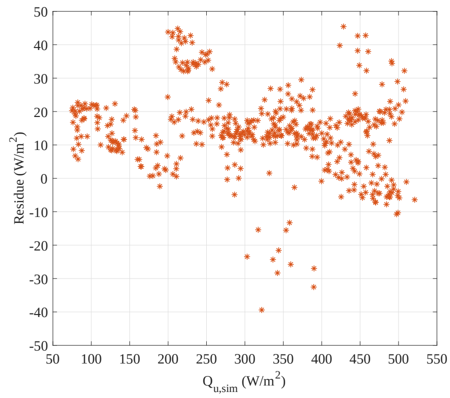

(c) Residue vs. simulated Q_u.

Figure 5.5: (a) Experimental and simulated results, (b) residues of T_{out}, and (c) residues of Q_u from 22nd June at 0.055 kg/(s m^2).

intermittent clouds mainly before 12:00, the calculated MAE for T_{out} and Q_u are 1.6% and 4.9%, respectively. The outputs also did not fall substantially due to the solar radiation's sudden variation. In this case, the model underestimated 88% of the predictions, where 95% of the residues are between ±1 °C and 93% are between ±30 W/m^2. It is also noted that the maximum residue is less than 1.2 °C and less than 40 W/m^2.

5.2.2.4 Validation of results at medium-high airflow rate

Figure 5.7(a) shows solar radiation, experimental and simulated data of the test on 29th May (G_{air} = 0.09 kg/m^2.s). The calculated MAE for T_{out} and Q_u are 2.5% and 13.7%, respectively. The model prediction is the least accurate in this case due to high variations in I_T throughout the day. From 14:00 to 15:00 the model overestimated the experimental data by more than 2 °C and more than 56 W/m^2 and up to 130 W/m^2. This large difference can be due to any unknown experimental fluctuation during the test. From Figures 5.7(b)

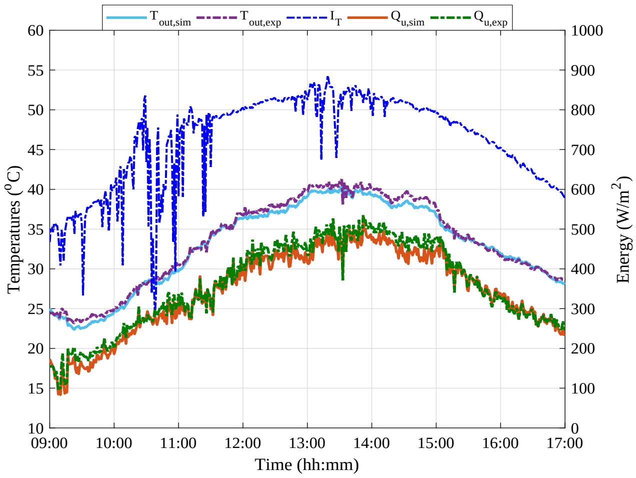

(a) Experimental and simulated results over time.

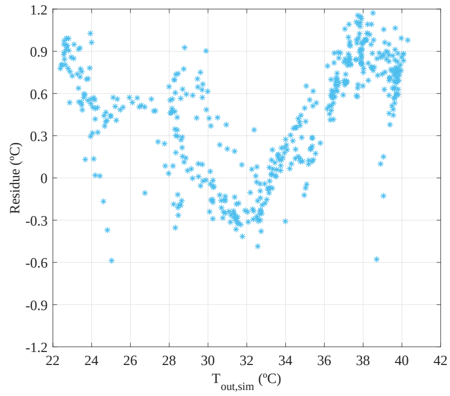

(b) Residue vs. simulated T_{out}.

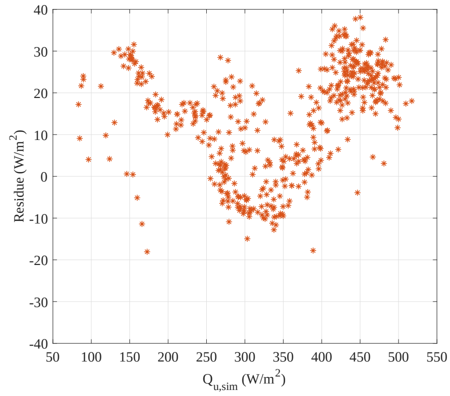

(c) Residue vs. simulated Q_u.

Figure 5.6: (a) Experimental and simulated results, (b) residues of T_{out}, and (c) residues of Q_u from 29th May at 0.07 kg/(s m^2).

and 5.7(c), the simulated outputs were also underestimated compared to the experimental results in 79% of the cases. It was found that 70% of the residues have magnitude of ±1 °C and 75% are between ±40 W/m^2.

5.2.2.5 Validation of results at high airflow rate

Figure 5.8(a) shows the graphs of solar radiation data, experimental and simulated results of the test on 28th June (G_{air} = 0.115 kg/(s m^2)), whereas Figures 5.8(b) and 5.8(c) present the residue plot in relation to the simulated values. On this clear sky day the calculated MAE for T_{out} and Q_u are 1.1% and 7.0%, respectively. In this case, the model underestimated 78% of the predictions, where 83% of the residues are between ±0.6 °C and 83% are between ±30 W/m^2. After 14:00 the model mostly underestimated Q_u by 20 to 40 W/m^2. It is also noticed that the maximum residue is less than 1.0 °C and less than 40 W/m^2.

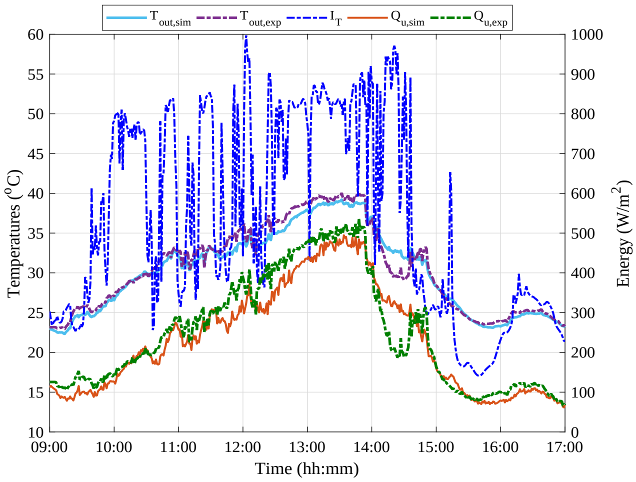

(a) Experimental and simulated results over time.

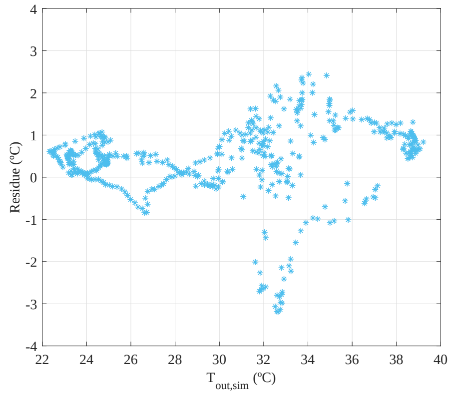

(b) Residue vs. simulated T_{out}.

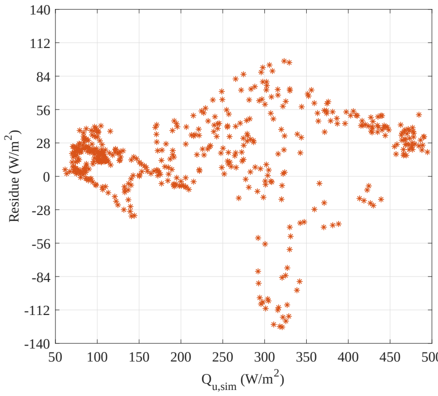

(c) Residue vs. simulated Q_u.

Figure 5.7: Experimental and simulated results from 31st May at 0.09 kg/(s m^2).

Hence, from the calculated MAE and residue plots, there was no effect of the airflow rate and time of operation on the model prediction. To check if solar radiation has influence on the model prediction, all residues were plotted against I_T and shown in Figure 5.9. It can be seen that the residues are concentrated on the region of I_T above 600 W/m^2 and most of them are between ±2.0 °C and ±50 W/m^2. The highest residues were observed for days with high intermittent clouds.

Another way to analyse these residue data is by plotting the cumulative frequency distribution of each simulated output, as shown in Figure 5.10. From the cumulative distributions, 95% of the data predicted have residues between ±2 °C and ±50 W/m^{2}C. It was also found that 65% of the predictions are underestimated, which highlights the underestimation of the simulation results at most of the time.

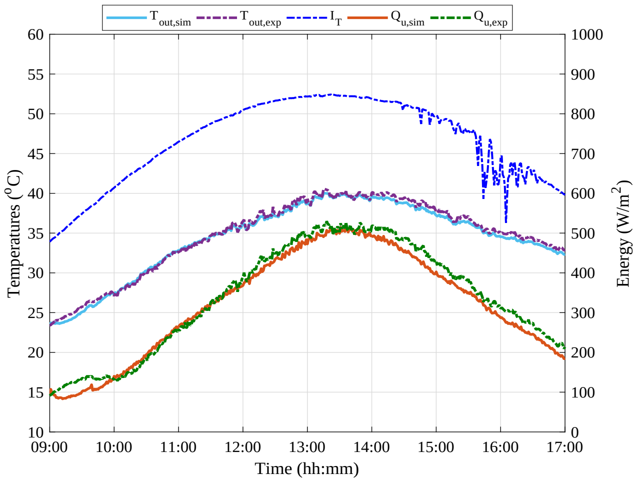

(a) Experimental and simulated results over time.

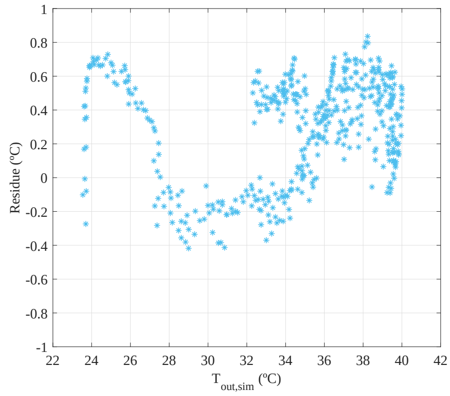

(b) Residue vs. simulated T_{out}.

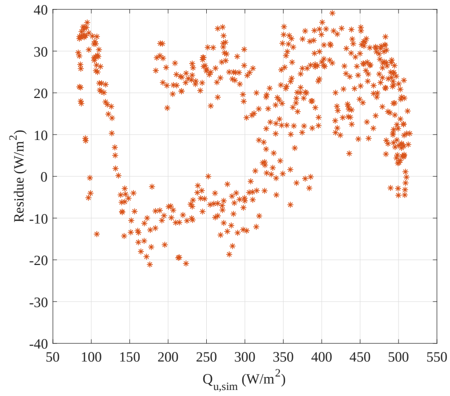

(c) Residue vs. simulated Q_u.

Figure 5.8: (a) Experimental and simulated results, (b) residues of T_{out}, and (c) residues of Q_u from 28th June at 0.115 kg/(s m^2).

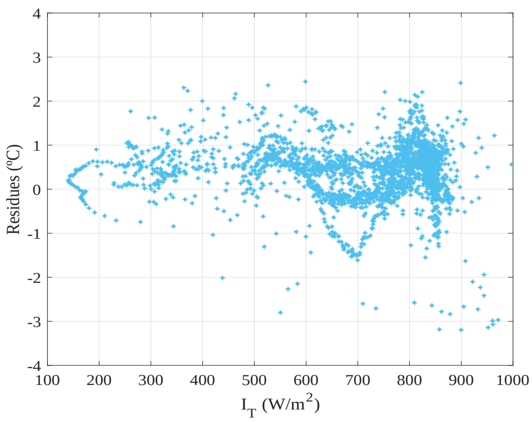

(a) Residue vs. solar radiation for T_{out}.

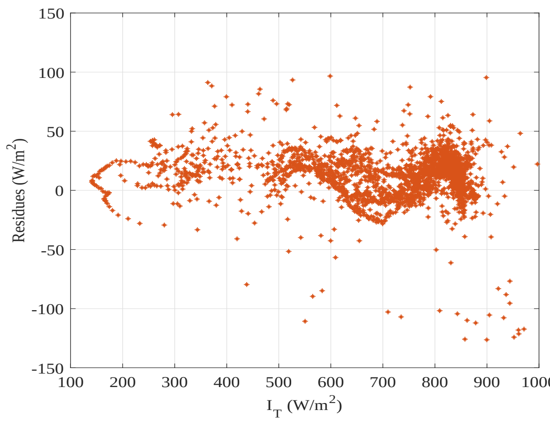

(b) Residue vs. solar radiation for Q_u.

Figure 5.9: Residues vs. solar radiation for (a) T_{out}, and (b) Q_u.

5.3 Thermal characterisation from simulation results

After validation, the heat transfer model was used to characterise the system's thermal performance under the conditions of clear sky days at transient state. The inputs

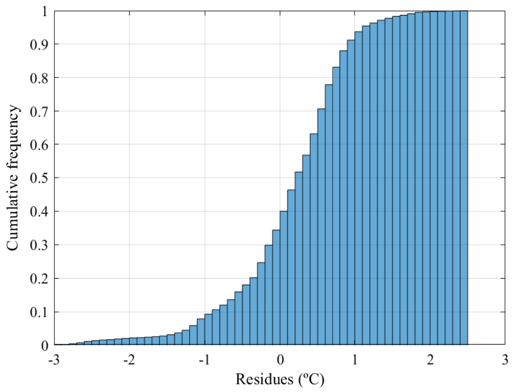

(a) Cumulative frequency of residues from T_{out}.

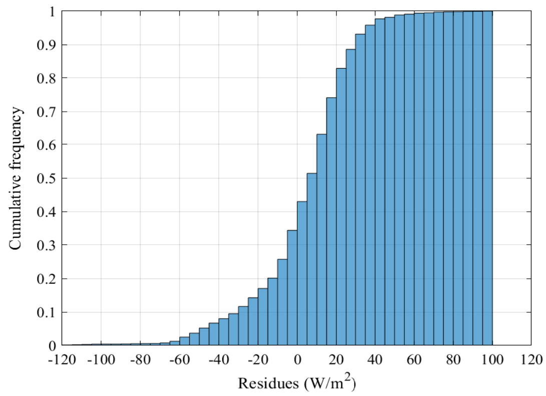

(b) Cumulative frequency of residues from Q_u.

Figure 5.10: Residual cumulative frequency distribution of (a) T_{out}, and (b) Q_u.

ranges, of which this system can be modelled, are depicted as follows:

Solar radiation: 500 – 1000 W/m^2, where the lowest limit corresponds to the airflow temperature increase at the beginning of the operation;

Mass airflow rate: 0.04 – 0.12 kg/(s m^2), where the limits are coincident to the ones of the tests;

Ambient temperature: 20 – 30 °C, which includes all the measured data on clear sky days;

Wind speed: 0 – 10 m/s, to include all the data taken from Met Eireann website.

5.3.1 Thermal performance of a single collector

To characterise this air heating system with one concentrator, a particular clear sky day (30th June) was taken to represent the results. The simulation was performed at the five different airflow rates and the correspondent graphs of T_{out} were plotted in Figure 5.11. All the temperature profiles reached their maximum levels in the hour of highest solar radiation (I_T = 860 W/m^2).

With the simulation data obtained, Figure 5.12 presents the surface and contour plot to fit the air temperature rise (ΔT) as function of the solar radiation and airflow rate. In overall, the air temperature rise is observed from I_T above 500 W/m^2 and increases in a nearly linear was as more energy is coming into the system. The opposite effect is noticed as the airflow is increased because ΔT is inversely proportional to G_{air}. Temperature rises

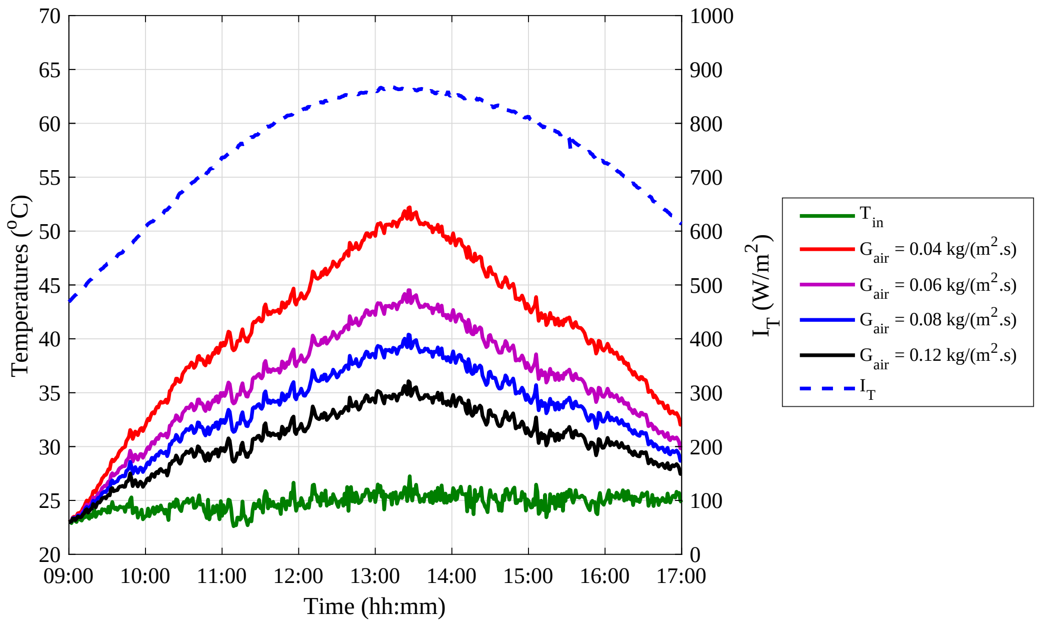

Figure 5.11: Simulated T_{out} at the five different airflow rates used in the tests, under conditions of 30th June.

above 27 °C can be obtained at airflow rate of 0.04 kg/(s m^2) when I_T is above 860 W/m^2.

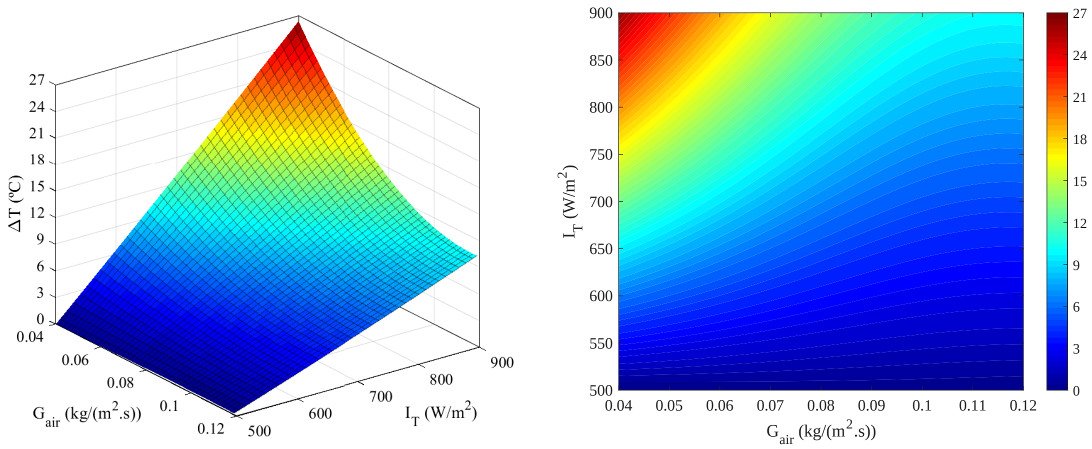

(a) Surface plot. (b) Contour plot.

Figure 5.12: (a) Surface and (b) contour plot of air temperature rise vs. solar radiation and airflow rate.

To express these results in terms of useful energy, Figure 5.13 shows surface and contour plot of this output against air temperature rise and airflow rate. Q_u increases as G_{air} and ΔT become higher as it is directly proportional to both inputs. The temperature increases more at lower airflow rates but at the cost of delivering low useful energy rate, which highlights the trade-off between energy collected and outlet air temperature.

Figure 5.14 shows simulated data takes under the same conditions depicted in Chap-

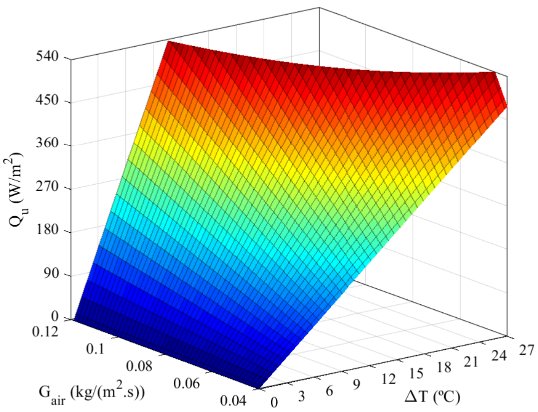

(a) Surface plot.

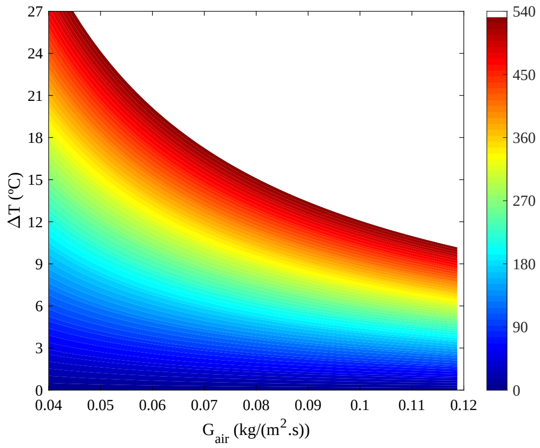

(b) Contour plot.

Figure 5.13: (a) Surface and (b) contour plot of useful energy vs. air temperature rise and airflow rate.

ter 4 at nearly steady state. Comparing the parameters of the Hottel-Whillier-Bliss equation, $F_R\eta_o$ and $F_R U_L$ calculated by the thermal model are 0.64 and -3.02, respectively, with relative difference of 2% and 10% in relation to the parameters of the experimental data. The coefficient of correlation of the simulated curve is 0.9.

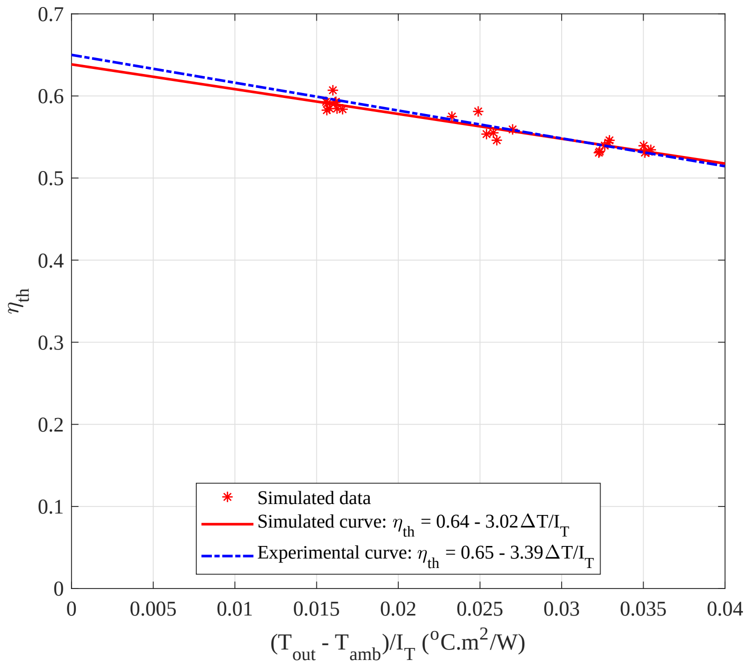

Figure 5.14: Experimental and simulated thermal efficiency curves.

5.3.2 Simulation of three connected collectors

The thermal performance of three collectors that are interconnected was analysed with regard to their connection in series and parallel configurations. The reason for selecting three collectors in this simulation is due to their collective total aperture height of approximately 1 meter when stacked above one another on a wall.

5.3.2.1 Connection in series

Figure 5.15 illustrates the frontal view drawing of the collectors arranged in series. In this configuration, the airflow enters the system through the labeled inlet duct and exits through the indicated outlet duct. The drawing indicates that the airflow leaving the first collector (IACPC 1) immediately enters the second collector (IACPC 2) at its right end, while the airflow leaving IACPC 2 enters the third collector (IACPC 3) at its left end.

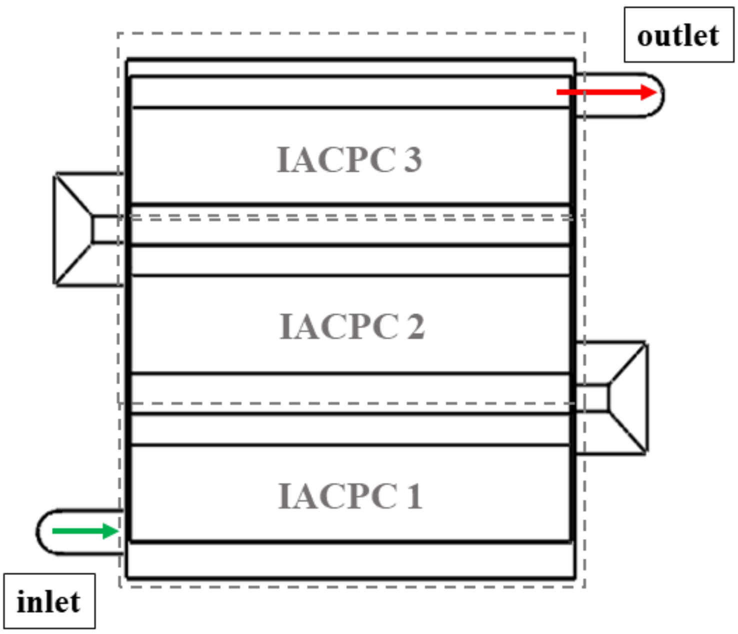

Figure 5.15: Frontal view of three collectors connected in series.

The outlet air temperature profiles at four different airflow levels throughout time of operation for the other two collectors are shown in Figure 5.16, where the results are for (a) the second collector and (b) for the third one.

Figure 5.17 shows the useful heat and the mean air temperature at noon hour as function of the airflow rate leaving each collector. The maximum mean T_{out} of the system

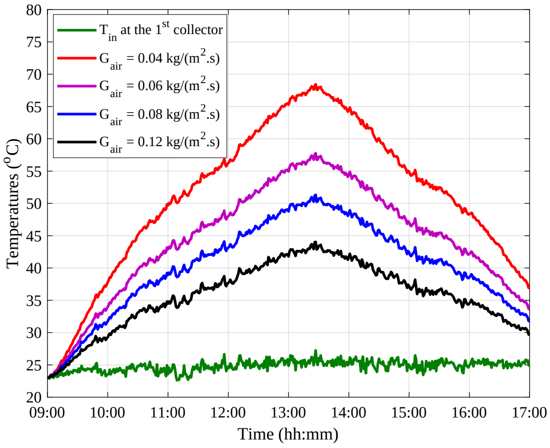

(a) Simulation results for the second collector.

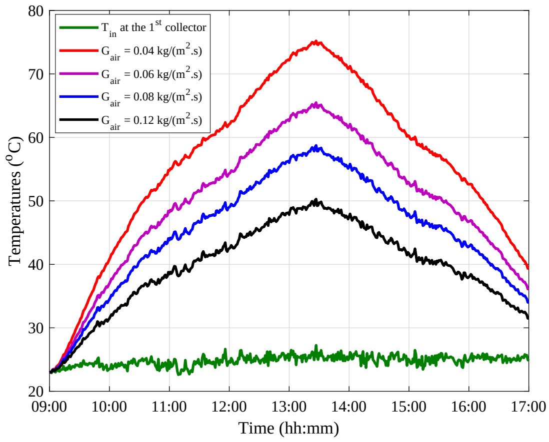

(b) Simulation results for the third collector.

Figure 5.16: Simulated T_{out} at four different airflow rates, for connection in series.

is 72 °C for the lowest level of G_{air}. On the other hand, the highest G_{air} is able to collect the highest Q_u value of 21.5 MJ/m^2 in total and delivering a mean temperature at noon of 48 °C. It is important to mention that the highest airflow rate can deliver approximately the same outlet air temperature as the the system consisting of a standalone collector at the lowest airflow rate. However the three-collector system collects 3 times more useful heat.

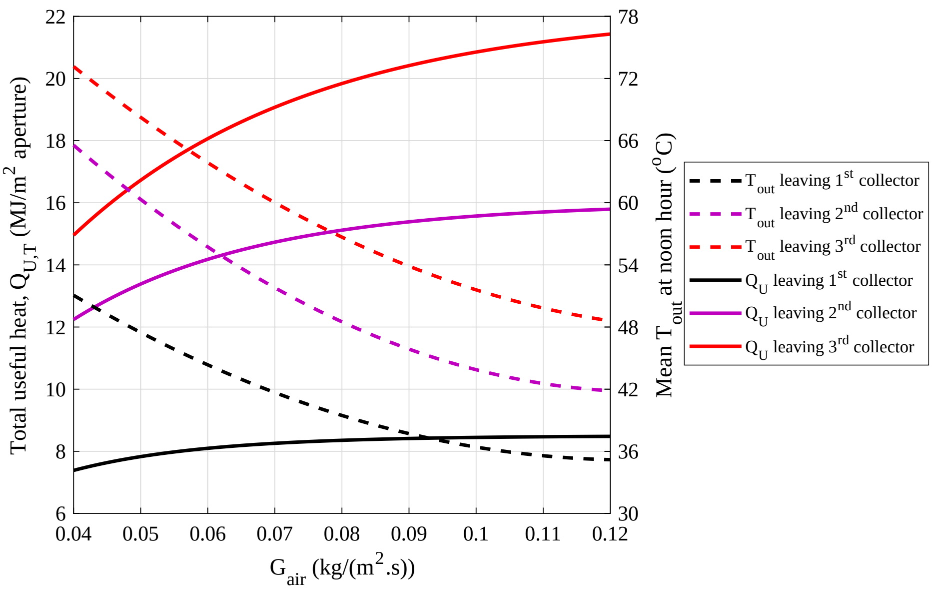

Figure 5.17: Total useful heat and mean T_{out} as function os the airflow rate level for connection in series.

5.3.2.2 Connection in parallel

In Figure 5.18 is shown the drawing of the collectors in frontal view connected in series, where the airflow is fed through the duct labelled as inlet. The main airflow is split into three equal airflows, each one coming into each collector on the left end. After leaving them on the right end, the small airflows are gathered and leave the system by the outlet duct.

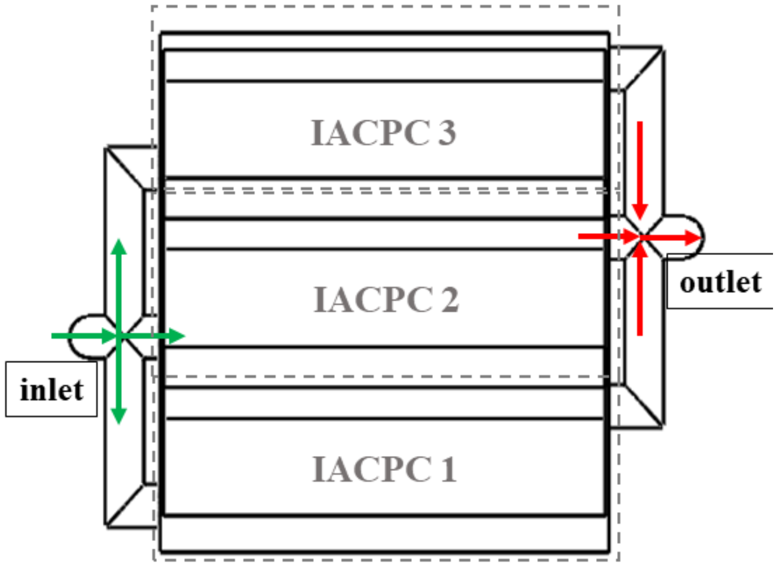

Figure 5.18: Frontal view of three collectors connected in parallel.

In Figure 5.19 is shown the graph of useful heat and outlet air temperature versus airflow rate for connection in parallel. In this case there is no increase in T_{out} but only for energy collection. This is the reason why the T_{out} graph is the profile leaving the first collector from Figure 5.17. However the useful heat collection was found to be higher than for the system in series if the same level of G_{air} is considered. For instance, at G_{air} = 0.12 kg/(m^2.s), Q_u = 22.5 MJ/m^2. This type of connection is useful if the operator needs to deliver more thermal energy with a considerable increase in T_{out}.

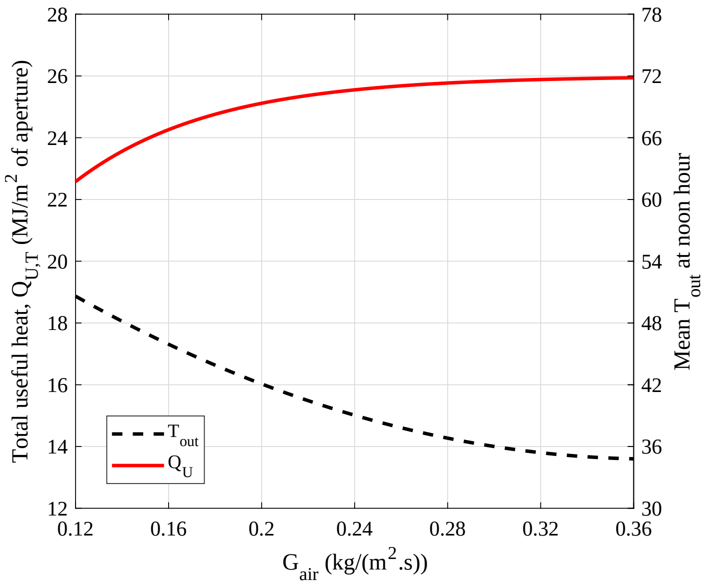

Figure 5.19: Total useful heat and mean T_{out} as function os the airflow rate level for connection in parallel.

5.4 Case study: barley drying

Drying is a thermal process involving the evaporation of moisture from grains in order to maintain their quality during storage and prevent the proliferation of bacteria, fungi, and pests. Drying also enables farmers to produce higher quality products that are suitable for both personal consumption and commercial purposes. For cereal grain, the recommended safe moisture content is typically within the range of 13 – 16% on a dry basis. Heated air is employed to dry, being the most common means of heat transfer. As a result of the heat application, a concentration gradient is established, creating a vapour pressure differential that causes moisture to move from the interior of the kernel towards the surface; the moisture is then evaporated and carried away from the product by the circulating air (Bala, 2017).

Barley is a versatile crop used for the production of malted products, flour, flakes for bakery, dietary formulations, and animal feed. The majority of barley production, approximately 90%, is intended for malting purposes due to the grain's firm texture, the presence of a protective hull during the germination process, and traditional use in brewing. The malting process involves hydration, germination, and drying, which convert the starch and protein in barley seeds into amino acids and fermentable carbohydrates. These components are utilized by yeast during the fermentation process and contribute to the sensory characteristics of the malt. It is essential that the metabolic activity and germination index of barley are preserved following processing, drying, and storage to facilitate effective germination (Soares et al., 2016).

In order to dry barley for malting, it is advised to maintain the maximum temperature in the grains at 45 ^{o}C, which can typically be achieved by using inlet air temperatures of approximately 60 – 65 ^{o}C (Embrapa, 2021; Syngenta, 2020). These temperature parameters are crucial to achieve proper drying of barley grains without harming their cell structure, which in turn preserves their ability to germinate successfully. (Soares et al., 2016).

Mathematical models can be employed to describe the process of drying. The thermal energy demand to dry a certain mass of product M_{bar} is described by Eq. (5.21) (McCabe et al., 1993):

$$Q_{dryer} = M_{bar}\left[\begin{array}{l} C_{p,bar}(T_{bar,out} - T_{bar,in}) + X_{in}C_{p,wl}(T_v - T_{bar,in}) + (X_{in} - X_{out})\lambda_v \\ +X_{out}C_{p,wl}(T_{bar,out} - T_v) + (X_{in} - X_{out})C_{p,v}(T_{bar,out} - T_v) \end{array}\right] \tag{5.21}$$

where it takes into account: i) the initial and final barley's moisture content X_{in} and X_{out}; ii) the initial barley temperature $T_{bar,in}$; iii) the air temperature at the dryer's inlet; iv) implicitly, the air humidity, and; v) specific heat of barley, liquid and vapour water, and latent heat of vaporization. The inlet air temperature at the dryer is the outlet temperature at the solar heating system T_{out}. The estimation of the temperature of vaporization T_v considers the ambient relative humidity and ambient temperature, and can be found using a numerical algorithm.

This energy demand is provided by an airflow pre-heated by gas burner, electric resistance or, partially, by solar air heaters to offset any other source of heating. Therefore, this topic aims at simulating the use of the solar air heating system previously validated to provide heated air to partially meet the energy required to dry barley. The assumptions for the simulation are depicted as follows:

✓ Initial moisture content of barley is 20% to be dried until it reaches 15%;

✓ The source of heating is obtained by burning natural gas whose calorific value is 40

MJ/m^3 (GOV-UK, 2022);

✓ The airflow temperature set to dry barley is 60 ^{o}C so that it speeds up the drying process while it does not hinge metabolic activity;

✓ The dryer is adiabatic.

The present topic considered three scenarios:

1. Simulating only a gas burner to heat the airflow up to 60 ^{o}C to meet the energy demand;
2. Simulating the solar heating system and a gas burner to heat the airflow up to 60 ^{o}C to meet the energy demand;
3. Simulating only the solar heating system to heat the airflow with no air temperature limit to meet the energy demand.

Figure 5.20 illustrates the schematic diagram of the drying process discussed in this study. The system comprises several key components: the Solar Air Heating System (SAHS), a gas burner, a control system, and a barley dryer. The role of the control system is to regulate the airflow rate, maintaining the airflow temperature at or below 60 ^{o}C. When this temperature falls below that threshold, the valve adjusts to introduce natural gas (NG) into the gas burner, raising the airflow temperature to 60 ^{o}C. In Scenario 1, the SAHS is inactive, allowing ambient air to enter the gas burner directly. In Scenario 2, both the SAHS and the gas burner operate simultaneously. Finally, in Scenario 3, the valve is closed, relying solely on the SAHS to heat the incoming fresh air.

All the scenarios considered the calculation of the barley mass dried and the amount of CO_2 released to atmosphere by burning natural gas in 8h of operation to match the solar heating system working hours (9:00 to 17:00). The airflow rate levels used were the ones used previously in the model simulation. The solar radiation levels used was the real solar data presented in Figure 5.11 of 30th June 2018 (clear sky day).

To illustrate in terms of energy, the SAHS is considered to be operating in series with the lowest and highest evaluated flow rates, as shown in Figures 5.21, 5.22, and 5.23. In these Figures, the red line represents the energy required for heated air to enter the dryer at 60 ^{o}C, while the blue line represents the energy supplied by the SAHS. In Figure 5.21, which represents the energy at the output of the first solar collector, for both flow

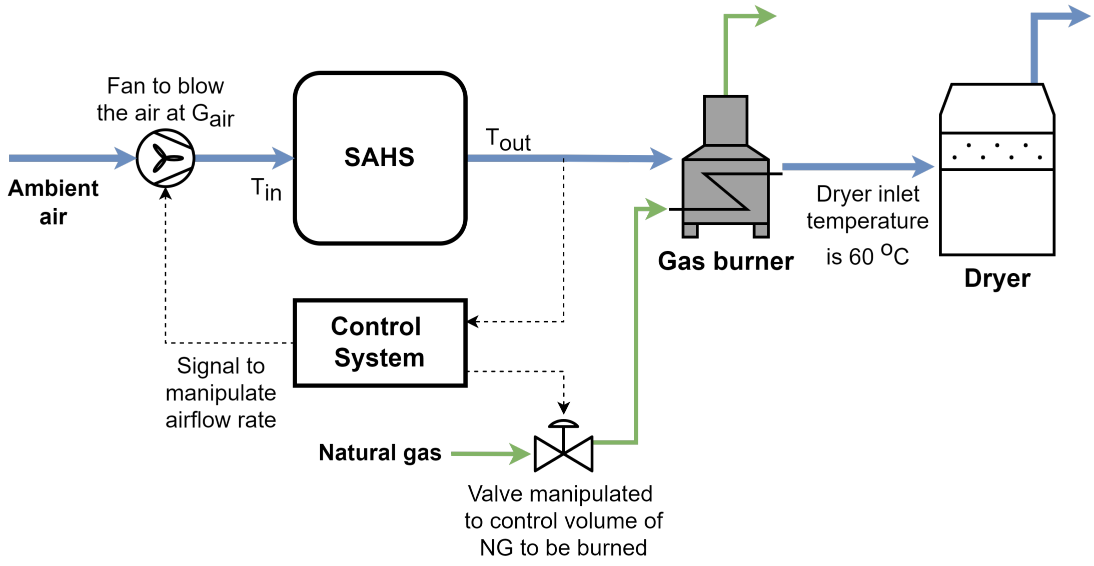

Figure 5.20: Block diagram of the simulated process of solar drying.

rates, there is an energy deficit between the supplied and required energy, necessitating the activation of the gas burner to bridge this gap. In Figure 5.22, illustrating the energy at the output of the second collector, for the lowest airflow rate, there is a period of operation (between 12:20 and 14:30) where the energy from the SAHS surpasses the required energy, resulting in a surplus, and thus, the burner does not need to operate. Conversely, in Figure 5.23, at the output of the third collector, the period of surplus energy extends (between 11:30 and 15:00), requiring less from the burner. In the simulation with the highest airflow rate, the energy deficit naturally decreases.

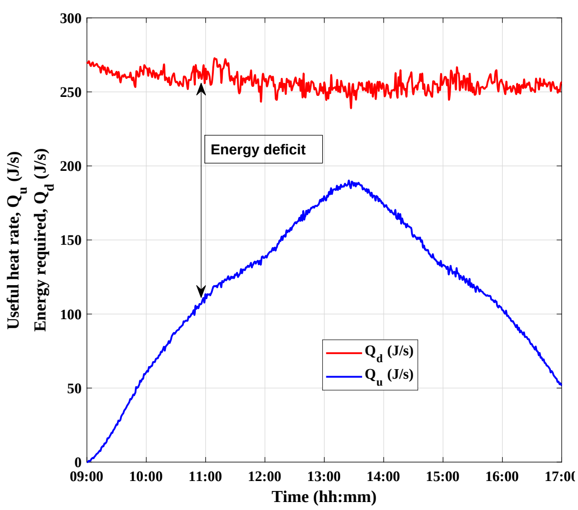

(a) Energy results at G_{air} = 26.10 kg/h.

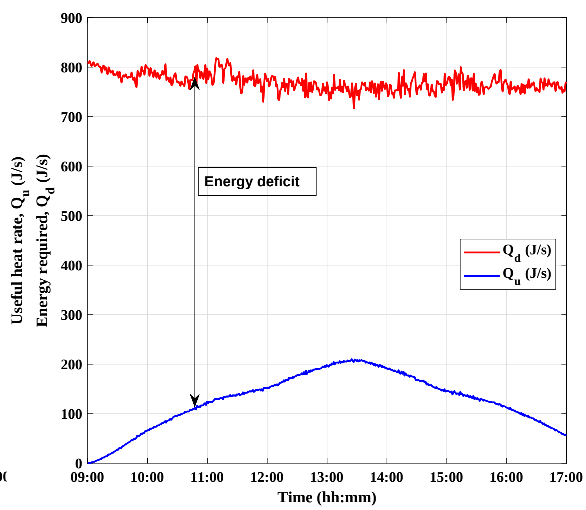

(b) Energy results at G_{air} = 78.30 kg/h.

Figure 5.21: Simulated energies for two different airflow rates at the first collector in series.

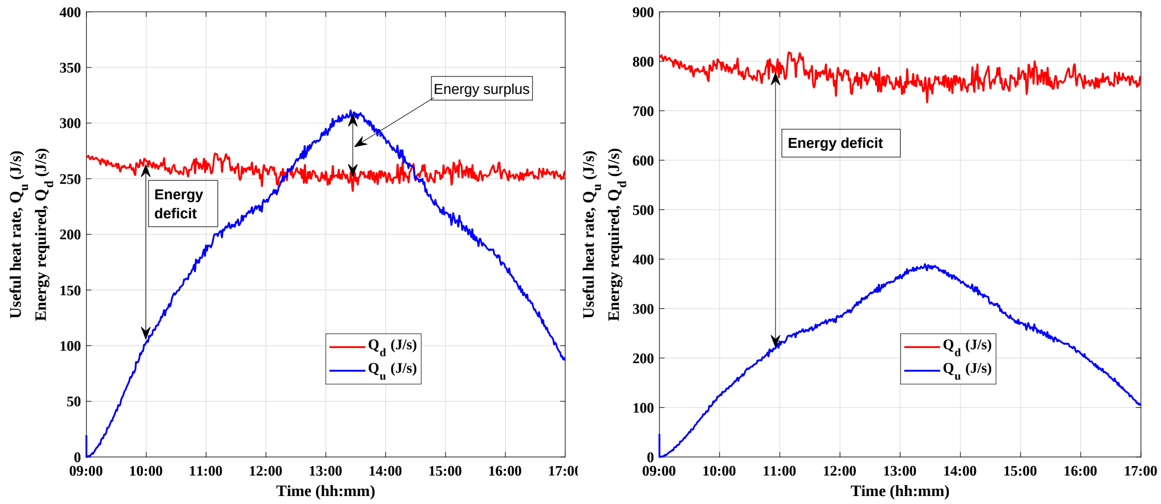

(a) Energy results at G_{air} = 26.10 kg/h. (b) Energy results at G_{air} = 78.30 kg/h.

Figure 5.22: Simulated energies for two different airflow rates at the second collector in series.

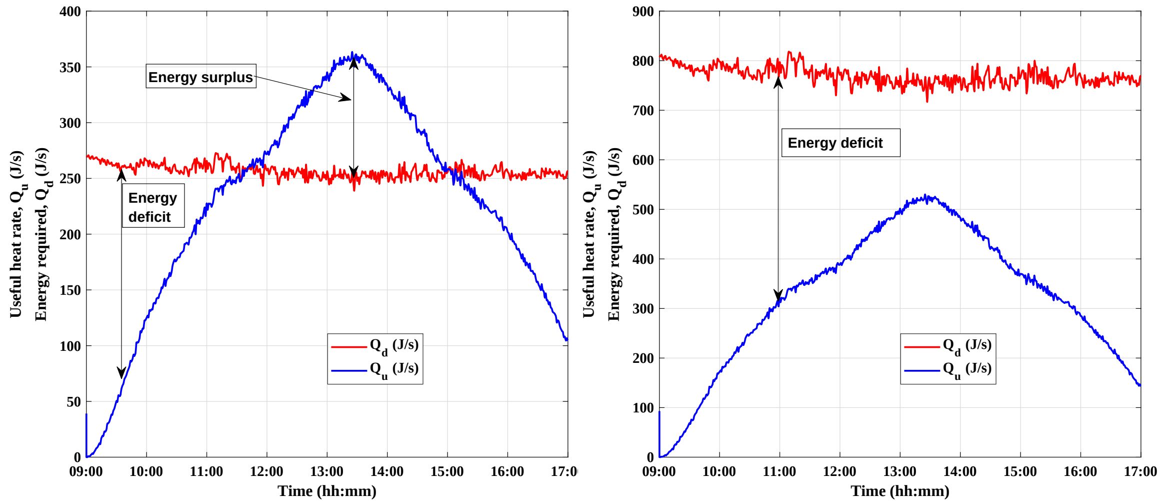

(a) Energy results at G_{air} = 26.10 kg/h. (b) Energy results at G_{air} = 78.30 kg/h.

Figure 5.23: Simulated energies for two different airflow rates at the third collector in series.

5.4.1 Scenario 1 – Air heating by gas burner alone

The required heat rate transferred to the airflow by the gas burner is calculated by Eq. (4.2). At an average ambient temperature of 25 ^{o}C and average relative humidity of 55% on a clear sky day, the energy demand Q_{dryer} calculated is 0.05 kWh/kg of dried barley. Table 5.2 shows the values of energy required, mass dried, volume of natural gas burned and mass of CO_2 released for each airflow level.

Table 5.2: Quantity of barley dried and amount of CO_2 released for 8h of operation as function of the airflow rate only using gas burner for air heating.

G_{air} (kg/h)	Q_{req} (kWh)	$M_{bar,dried}$ (kg)	Gas volume (L)	M_{CO2} (kg)
26.10	2.053	41	184.75	0.364
39.15	3.083	61	277.50	0.547
52.20	4.108	81	369.75	0.728
78.30	6.161	122	554.50	1.092

At this airflow rate range and operating for 8 hours, 41 – 122 kg of barley can be dried to reduce its moisture content from 20 to 15% in dry basis.

5.4.2 Scenario 2 – Air heating using gas burner and solar system

In this scenario, the energy required to heat the airflow to 60 ^{o}C is partially provided by the solar heating system and the complementary is by the gas burner. The connection between solar collectors in the system is also considered. Table 5.3 shows the values for a connection of up to 3 collectors in series of energy required and energy provided by each mode, volume of natural gas burned, mass of CO_2 released and the solar fraction for each airflow level. The solar fraction is defined as the ratio of the energy provided by the solar system (Q_u) and the energy required (Q_{req}). Additionally, Table 5.4 shows values for a connection of 3 collectors operating in parallel, where the total airflow rates are triple the values for the range in series (78.30 – 235 kg/h).

The amount of barley dried is the same as shown in Table 5.2 because the air temperature is set to 60 ^{o}C to enter the dryer. For a connection of 3 collectors in series, this solar heating system can offset from 42 to 79% of the energy provided by the gas burner alone.

Considering collectors operating in parallel, the energy required is evidently increased due to higher airflow levels. The useful energy collected by the solar system is also higher. The solar fraction calculated is the same obtained when the system is operated in series, meaning that both connections will offset the the same energy levels relative to the required ones. The advantage of operating in parallel over in series is that the amount of barley dried is increased by 3 times: 122 – 366 kg of barley can be dried to reduce its moisture content from 20 to 15% in dry basis.

Table 5.3: Quantity of barley dried and amount of CO_2 released for 8h of operation as function of the airflow rate using gas burner and solar system for air heating for connection of up to 3 collectors in series.

G_{air} (kg/h)	Q_{req} (kWh)	Q_u (kWh)	Q_{burner} (kWh)	Gas Volume (L)	M_{CO2} (kg)	Solar Fraction
After the 1st collector						
26.10	2.053	0.933	1.119	100.75	0.198	0.4547
39.15	3.083	0.978	2.106	189.50	0.373	0.3171
52.20	4.108	1.000	3.108	279.75	0.551	0.2434
78.30	6.161	1.100	5.061	455.50	0.897	0.1785
After the 2nd collector in series						
26.10	2.053	1.544	0.508	45.75	0.090	0.7524
39.15	3.083	1.635	1.448	130.31	0.257	0.5304
52.20	4.108	1.726	2.382	214.38	0.422	0.4202
78.30	6.161	1.908	4.253	382.75	0.754	0.3097
After the 3rd collector in series						
26.10	2.053	1.819	0.233	21.00	0.041	0.7904
39.15	3.083	2.015	1.068	96.13	0.189	0.6850
52.20	4.108	2.211	1.897	170.75	0.336	0.5766
78.30	6.161	2.603	3.558	320.25	0.631	0.4225

5.4.3 Scenario 3 – Air heating using solar system alone

In this scenario, the energy transferred to the airflow is only provided by the solar collectors. For most of the time, the solar energy is insufficient to rise the temperature to 60 ^{o}C, which resulted in low drying rates, and therefore in lower dried mass of barley. Table 5.5 shows the mass of barley that can be dried if only the solar heating system is would be used in the operation. The quantity of mass dried varies from 22 – 61 kg, considerably less compared to the other systems as the drying rate is lower.

When the air heating collectors are connected in parallel, the thermal energy absorbed by the airflow rate is higher, which results in more mass dried, as shown in Table 5.6. As the airflow rate is tripled, the quantity of barley dried is tripled as well (66 – 84 kg), which is an advantage over the connection in series.

In this study, a particular airflow range was utilized, and a common level of 78.3 kg/h can be used to compare the three previously analyzed scenarios. This assessment can

Table 5.4: Quantity of barley dried and amount of CO_2 released for 8h of operation as function of the airflow rate using gas burner and solar system for air heating for connection of 3 collectors in parallel.

G_{air} (kg/h)	Q_{req} (kWh)	Q_u (kWh)	Q_{burner} (kWh)	Gas Volume (L)	M_{CO2} (kg)	Solar Fraction
3x26.10	6.161	4.870	1.291	116.20	0.229	0.7904
3x39.15	9.250	6.336	2.914	262.55	0.517	0.6850
3x52.20	12.325	7.107	5.218	469.66	0.925	0.5766
3x78.30	18.483	7.810	10.673	960.60	1.892	0.4225

Table 5.5: Quantity of barley dried and amount of CO_2 released for 8h of operation as function of the airflow rate using solar system alone for air heating for connection of 3 collectors in series.

G_{air} (kg/h)	After 1st collector		After 2nd collector		After 3rd collector	
	Q_u (kWh)	$M_{bar,dried}$ (kg)	Q_u (kWh)	$M_{bar,dried}$ (kg)	Q_u (kWh)	$M_{bar,dried}$ (kg)
26.10	0.933	22	1.544	33	1.819	37
39.15	0.978	24	1.635	37	2.015	43
52.20	1.000	25	1.726	40	2.211	50
78.30	1.100	28	1.908	47	2.603	61

be conducted by examining the mass of dried barley, the amount of natural gas burned, and the solar fraction, all of which are presented in Table 5.7. The gas burner system has the highest gas volume consumption of 554.5 L and a solar fraction of 0, meaning it relies completely on gas for heating. On the other hand, the SAHS standalone system produces less dried mass, but both connections have a solar fraction of 1, indicating that they rely solely on solar energy. The results indicate that the use of solar air heating systems can substantially reduce dependence on natural gas heating. Specifically, the gas burner + SAHS in parallel configuration exhibited the lowest gas consumption and highest solar fraction among all the listed systems with gas burner. Nevertheless, the selection of a heating system will depend on various factors, such as sunlight availability, natural gas cost, and accessibility.

5.5 Chapter Summary

A thermal modelling and simulation of the proposed solar air heating system was developed and it was validated against experimental data. Results show that, in general,

Table 5.6: Quantity of barley dried and amount of CO_2 released for 8h of operation as function of the airflow rate using solar system alone for air heating for connection of 3 collectors in parallel.

G_{air} (kg/h)	Q_u (kWh)	$M_{bar,dried}$ (kg)
3x26.10	2.800	66
3x39.15	2.933	72
3x52.20	3.000	75
3x78.30	3.300	84

Table 5.7: Comparison of the 3 scenarios at G_{air} = 78.3 kg/h for 8h of operation.

Type of system	$M_{bar,dried}$ (kg)	Gas volume (L)	Solar fraction
Gas burner only	122	554.50	0.00
Gas burner + SAHS series	122	320.25	0.42
Gas burner + SAHS parallel	122	116.20	0.79
SAHS series	61	0.00	1.00
SAHS parallel	65	0.00	1.00

the heat transfer model underestimates 65% of the data and 95% of the residues generated are between ±2 °C and ±50 W/m^2. In overall, the mean absolute error in terms of temperature was found to be 2% and in terms of useful energy was 8%. After validation, the system has been characterised within a certain range of inputs.

The model was also used to simulate results at nearly steady state condition. The thermal efficiency curve was plotted and compare it to the experimental one. The parameters of the Hottel-Whillier-Bliss equation $F_R\eta_o$ and $F_R U_L$ calculated by the thermal model are 0.64 and -3.02, with relative difference of 2% and 10%, respectively, in relation to the parameters of the experimental data.

The thermal modelling was also used to predict the thermal performance of three connected collectors in series and in parallel. The connection in series is able to deliver higher outlet airflow temperatures whereas the connection in parallel can collect more useful heat but delivering the same airflow temperature as if it is leaving the first collector in series.

Lastly, this model was used for simulating barley drying. Three scenarios were considered to meet the energy demand: simulating only a gas burner to heat the airflow up to 60 °C; simulating the solar heating system and a gas burner to heat the airflow up to 60 ^{o}C, and; simulating only the solar heating system to heat the airflow with no air temperature limit. From an specific airflow level used in the simulations, the gas burner system has the highest gas volume consumption and a solar fraction of 0, meaning it relies completely on gas for heating. On the other hand, the SAHS standalone system produces less dried mass, but both connections have a solar fraction of 1, indicating that they rely solely on solar energy. The results indicate that the use of solar air heating systems can substantially reduce dependence on natural gas heating. Specifically, the gas burner + SAHS in parallel configuration exhibited the lowest gas consumption and highest solar fraction among all the listed systems with gas burner. Nevertheless, the selection of a heating system will depend on various factors, such as sunlight availability, natural gas cost, and accessibility.

CHAPTER 6

CONCLUSIONS

The conclusions from this PhD work are listed as follows:

✓ Development of a 3D ray tracing for optical analysis of direct radiation to assist the selection of a collector design: an optical analysis has been undertaken to evaluate its optical efficiency considering factors as: glazing transmittance, truncation level, length and tertiary section height. The results show that there is a maximum value of optical efficiency for a particular parabolic reflector shape and a maximum value of glazing transmittance at different inclinations. The proposed air heater concentrator is able to absorb in average 67% of direct solar radiation during most part of the day in the period evaluated;

✓ Performance of experimental work to characterise the specific type of collector: the experiments were carried out in open loop configuration, where the air was blown by a 12-W fan with a voltage adaptor to vary the airflow rate. Experimental results were analysed for different airflow rates ranging between 0.04 and 0.115 kg/m^2.s. Results show that the maximum outlet air temperatures at solar noon (13:00 to 14:00) varied from 40 ^{o}C at the highest airflow to 52 ^{o}C at the lowest and the thermal efficiency varied from 52% to 62%.

✓ Thermal modelling of the solar air heating concentrator and validation against experimental results: it was shown that, in general, the heat transfer model underestimates 65% of the data and 95% of the residues generated are between ±2 ^{o}C and ±50 W/m^2. In overall, the mean absolute error in terms of temperature was found to be 2% and in terms of useful energy was 8%. The model was also used to simulate results at nearly steady state condition. The thermal efficiency curve was plotted and compare it to the experimental one. The parameters of the Hottel-Whillier-Bliss equation were calculated by the thermal model with relative difference of 2% and 10%, respectively, in relation to the parameters of the experimental data.

✓ Thermal simulation of a system consisted of more than one collector connected together: The thermal modelling was also used to predict the thermal performance of three connected collectors in series and in parallel. The connection in series is able to deliver higher outlet airflow temperatures whereas the connection in parallel can collect more useful heat but delivering the same airflow temperature as if it is leaving the first collector in series.

✓ Use of this thermal model for simulating barley drying: Three scenarios were considered to meet the energy demand: simulating only a gas burner to heat the airflow up to 60 ^{o}C; simulating the solar heating system and a gas burner to heat the airflow up to 60 ^{o}C, and; simulating only the solar heating system to heat the airflow with no air temperature limit. From an specific airflow level used in the simulations, the gas burner system has the highest gas volume consumption and a solar fraction of 0, meaning it relies completely on gas for heating. On the other hand, the SAHS standalone system produces less dried mass, but both connections have a solar fraction of 1, indicating that they rely solely on solar energy.

The suggestions for the future are listed as follows:

✓ Use the ray tracing technique to simulate diffuse radiation in 3D to have better results for optical modelling;

✓ Run experiments using more than one solar air heating collector connected to find the best configuration in terms of air temperature delivered and energy collection.

✓ Perform a Computational Fluid Dynamics (CFD) modelling to better understand the heat transfer within the concentrator. Simulations will be undertaken to investigate the effect of the tertiary section height and the collector's size;

✓ Develop a control algorithm to deliver airflow temperature at a certain set-point and further use of proper equipment to maintain this air temperature at the set-point according to the application required.

✓ Couple a solar air heating system to a real dryer and run experiments to measure how much barley can be dried at a fixed air temperature.

REFERENCES

Abdel-Khalik, S. I., Li, H.-W., and Randall, K. R. (1978). "Natural Convection In Compound Parabolic Concentrators – A Finite-Element Solution". *Journal of Heat Transfer* 100.2, pp. 199–204. DOI: 10.1115/1.3450781.

Abdullahi, B., Al-Dadah, R., Mahmoud, S., and Hood, R. (2015). "Optical and thermal performance of double receiver compound parabolic concentrator". *Applied Energy* 159, pp. 1–10. DOI: 10.1016/j.apenergy.2015.08.063.

Abu-Bakar, S. H., Muhammad-Sukki, F., Ramirez-Iniguez, R., Mallick, T. K., Munir, A. B., Yasin, S. H. M., and Rahim, R. A. (2014). "Rotationally asymmetrical compound parabolic concentrator for concentrating photovoltaic applications". *Applied Energy* 136, pp. 363–372. DOI: 10.1016/j.apenergy.2014.09.053.

Alanod (2016). *MIRO-SUN*. URL: https://www.alanod.com/en/reflection/miro-sun/.

Ali, I. M. S., O'Donovan, T. S., Reddy, K., and Mallick, T. K. (2013). "An optical analysis of a static 3-D solar concentrator". *Solar Energy* 88, pp. 57–70. DOI: 10.1016/j.solener.2012.11.004.

Ali, I. M. S., Vikram, T. S., O'Donovan, T. S., Reddy, K., and Mallick, T. K. (2014). "Design and experimental analysis of a static 3-D elliptical hyperboloid concentrator for process heat applications". *Solar Energy* 102, pp. 257–266. DOI: 10.1016/j.solener.2014.01.031.

Alta, D., Bilgili, E., Ertekin, C., and Yaldiz, O. (2010). "Experimental investigation of three different solar air heaters: Energy and exergy analyses". *Applied Energy* 87.10, pp. 2953–2973. DOI: 10.1016/j.apenergy.2010.04.016.

Ammari, H. (2003). “A mathematical model of thermal performance of a solar air heater with slats”. *Renewable Energy* 28.10, pp. 1597–1615. DOI: 10.1016/s0960-1481(02)00253-7.

Arulanandam, S., Hollands, K., and Brundrett, E. (1999). “A CFD heat transfer analysis of the transpired solar collector under no-wind conditions”. *Solar Energy* 67.1-3, pp. 93–100. DOI: 10.1016/S0038-092X(00)00042-6.

Assari, M. R., Tabrizi, H. B., and Jafari, I. (2011). “Experimental and theoretical investigation of dual purpose solar collector”. *Solar Energy* 85.3, pp. 601–608. DOI: 10.1016/j.solener.2011.01.006.

Athienitis, A. K., Bambara, J., O’Neill, B., and Faille, J. (2011). “A prototype photovoltaic/thermal system integrated with transpired collector”. *Solar Energy* 85.1, pp. 139–153. DOI: 10.1016/j.solener.2010.10.008.

Badache, M., Hallé, S., Rousse, D. R., Quesada, G., and Dutil, Y. (2014). “An experimental investigation of a two-dimensional prototype of a transparent transpired collector”. *Energy and Buildings* 68, pp. 232–241. DOI: 10.1016/j.enbuild.2013.09.010.

Bala, B. K. (2017). *Drying and Storage of Cereal Grains*. 2nd ed. John Wiley and Sons Ltd. ISBN: 9781119124238. DOI: 10.1002/9781119124207.

Banks, J. and Carson, J. S. (1987). “Applying the simulation process”. *Proceedings of the 19th Conference on Winter Simulation*. ACM Press. DOI: 10.1145/318371.318386.

Bellos, E., Korres, D., Tzivanidis, C., and Antonopoulos, K. (2016). “Design, simulation and optimization of a compound parabolic collector”. *Sustainable Energy Technologies and Assessments* 16, pp. 53–63. DOI: 10.1016/j.seta.2016.04.005.

Benrejeb, R., Helal, O., and Chaouachi, B. (2015). “Optical and thermal performances improvement of an ICS solar water heater system”. *Solar Energy* 112, pp. 108–119. DOI: 10.1016/j.solener.2014.11.011.

Benrejeb, R., Helal, O., and Chaouachi, B. (2016). “Study of the effect of truncation on the optical and thermal performances of an ICS solar water heater system”. *Solar Energy* 132, pp. 84–95. DOI: 10.1016/j.solener.2016.02.057.

Binotti, M., Zhu, G., Gray, A., Manzolini, G., and Silva, P. (2013). “Geometric analysis of three-dimensional effects of parabolic trough collectors”. *Solar Energy* 88, pp. 88–96. DOI: 10.1016/j.solener.2012.10.025.

Buker, M. S. and Riffat, S. B. (2015). “Building integrated solar thermal collectors – A review”. *Renewable and Sustainable Energy Reviews* 51, pp. 327–346. DOI: 10.1016/j.rser.2015.06.009.

Carvalho, M., Collares-Pereira, M., Gordon, J., and Rabl, A. (1985). “Truncation of CPC solar collectors and its effect on energy collection”. *Solar Energy* 35.5, pp. 393–399. DOI: 10.1016/0038-092x(85)90127-6.

Cengel, Y. A. and Turner, R. H. (2004). *Fundamentals of Thermal-Fluid Sciences*. 2nd ed. McGraw-Hill. ISBN: 0-07-245426-1.

Christensen, C. B., Kutscher, C. F., and Gawlik, K. M. (1997). *Unglazed transpired solar collector having a low thermal conductance absorber*. U. S. Patent No. 5,692,491, Application No. 639,852.

COST Office (2015). “Building Integration of Solar Thermal Systems”. *Proceedings of COST Action TU1205 Symposium*. Ed. by S. A. Kalogirou. ISBN: 978-9963-697-17-5.

Decker, G. V., Hollands, K., and Brunger, A. (2001). “Heat-exchange relations for unglazed transpired solar collectors with circular holes on a square or triangular pitch”. *Solar Energy* 71.1, pp. 33–45. DOI: 10.1016/s0038-092x(01)00014-7.

Delta-T Devices (2018). *DL2e Data Logger*. URL: https://www.delta-t.co.uk/product/dl2e/.

Dev, R., Abdul-Wahab, S. A., and Tiwari, G. (2011). “Performance study of the inverted absorber solar still with water depth and total dissolved solid”. *Applied Energy* 88.1, pp. 252–264. DOI: 10.1016/j.apenergy.2010.08.001.

Diaz, G. and Winston, R. (2008). “Effect of Surface Radiation on Natural Convection in Parabolic Enclosures”. *Numerical Heat Transfer, Part A: Applications* 53.9, pp. 891–906. DOI: 10.1080/10407780701789518.

Duffie, J. A. and Beckman, W. A. (2013). *Solar Engineering of Thermal Processes*. 4th ed. John Wiley & Sons, Inc. ISBN: 978-0-470-87366-3.

Eames, P. C., Norton, B., and Kothdiwala, A. F. (1996). "The state of the art in modelling line-axis concentrating solar energy collectors". *Renewable Energy* 9.1-4, pp. 562–567. DOI: 10.1016/0960-1481(96)88352-2.

Eames, P. and Norton, B. (1993a). "Detailed parametric analyses of heat transfer in CPC solar energy collectors". *Solar Energy* 50.4, pp. 321–338. DOI: 10.1016/0038-092x(93)90027-l.

Eames, P. and Norton, B. (1993b). "Validated, unified model for optics and heat transfer in line-axis concentrating solar energy collectors". *Solar Energy* 50.4, pp. 339–355. DOI: 10.1016/0038-092x(93)90028-m.

Eames, P. and Norton, B. (1995). "Thermal and optical consequences of the introduction of baffles into compound parabolic concentrating solar energy collector cavities". *Solar Energy* 55.2, pp. 139–150. DOI: 10.1016/0038-092x(95)00039-t.

Eames, P., Smyth, M, and Norton, B (2001). "The experimental validation of a comprehensive unified model for optics and heat transfer in line-axis solar energy systems". *Solar Energy* 71.2, pp. 121–133. DOI: 10.1016/s0038-092x(01)00027-5.

Easy Composites (2017). *Carbon Fibre Plain Weave 3k 210g 1m Wide*. URL: https://www.easycomposites.co.uk/#!/fabric-and-reinforcement/carbon-fibre-reinforcement/woven-carbon-cloth-under-400gsm/plain-weave-200gsm-3k.html.

El-Sebaii, A., Aboul-Enein, S., Ramadan, M., Shalaby, S., and Moharram, B. (2011). "Investigation of thermal performance of-double pass-flat and v-corrugated plate solar air heaters". *Energy* 36.2, pp. 1076–1086. DOI: 10.1016/j.energy.2010.11.042.

El-Sebaii, A. and Al-Snani, H. (2010). "Effect of selective coating on thermal performance of flat plate solar air heaters". *Energy* 35.4, pp. 1820–1828. DOI: 10.1016/j.energy.2009.12.037.

Embrapa (Dec. 20, 2021). *Cevada. Secagem*. Ed. by P. R. V. da Silva Pereira and E. Minella. URL: https://www.embrapa.br/agencia-de-informacao-tecnologica/cultivos/cevada/pos-producao/secagem.

European Solar Thermal Technology Platform (2009). *Solar Heating and Cooling for a Sustainable Energy Future in Europe*. Tech. rep. European Technology and Innovation Platform on Renewable Heating and Cooling. URL: https://www.rhc-platform.org/content/uploads/2019/05/ESTTP_SRA_RevisedVersion.pdf.

Evangelisti, L., Vollaro, R. D. L., and Asdrubali, F. (2019). "Latest advances on solar thermal collectors: A comprehensive review". *Renewable and Sustainable Energy Reviews* 114, p. 109318. DOI: 10.1016/j.rser.2019.109318.

Fanney, A. H. and Thomas, W. C. (1981). "Simulation of Thermal Performance of Solar Collector Arrays". *Journal of Solar Energy Engineering* 103.3, pp. 258–267. DOI: 10.1115/1.3266249.

First Glass Ltd (2016). *Toughened Glass*. URL: http://www.firstglass.ie/products_toughened_glass.html.

Francesconi, M. and Antonelli, M. (2018). "A CFD analysis to investigate thermal losses in a panel composed of several CPC concentrators". *Thermal Science and Engineering Progress* 5, pp. 278–288. DOI: 10.1016/j.tsep.2017.12.005.

Furbo, S. and Shah, L. J. (2003). "Thermal advantages for solar heating systems with a glass cover with antireflection surfaces". *Solar Energy* 74.6, pp. 513–523. DOI: 10.1016/s0038-092x(03)00186-5.

Gawlik, K., Christensen, C., and Kutscher, C. (2005). "A Numerical and Experimental Investigation of Low-conductivity Unglazed, Transpired Solar Air Heaters". *Journal of Solar Energy Engineering* 127.1, pp. 153–155. DOI: 10.1115/1.1823494.

Gawlik, K. M. and Kutscher, C. F. (Aug. 2002). "Wind Heat Loss From Corrugated, Transpired Solar Collectors". 124.3, pp. 256–261. DOI: https://doi.org/10.1115/1.1487886.

Goswami, D. Y. (2015). *Principles of Solar Engineering*. Ed. by T. F. Group. 3rd ed. CRC Press. ISBN: 9781466563780.

GOV-UK (July 28, 2022). *Digest of UK Energy Statistics (DUKES): calorific values and density of fuels*. URL: https://www.gov.uk/government/statistics/dukes-calorific-values.

Harmim, A., Merzouk, M., Boukar, M., and Amar, M. (2012). "Mathematical modeling of a box-type solar cooker employing an asymmetric compound parabolic concentrator". *Solar Energy* 86.6, pp. 1673–1682. DOI: 10.1016/j.solener.2012.03.020.

Hastings Robert; Morck, O., ed. (2000). *Solar Air Systems: A Design Handbook*. 1st ed.

Hegazy, A. A. (1999). "Optimum channel geometry for solar air heaters of conventional design and constant flow operation". *Energy Conversion and Management* 40.7, pp. 757–774. DOI: 10.1016/S0196-8904(98)00107-1.

Hegazy, A. A. (2000). "Comparative study of the performances of four photovoltaic/thermal solar air collectors". *Energy Conversion and Management* 41.8, pp. 861–881. DOI: 10.1016/s0196-8904(99)00136-3.

Heimsath, A., Bern, G., Rooyen, D. van, and Nitz, P. (2014). "Quantifying Optical Loss Factors of Small Linear Concentrating Collectors for Process Heat Application". *Energy Procedia* 48, pp. 77–86. DOI: 10.1016/j.egypro.2014.02.010.

Hoffman, J. D. (2001). *Numerical Methods For Engineers And Scientists*. 2nd ed. New York, USA: Marcel Dekker. ISBN: 0-8247-0443-6.

Hongn, M., Larsen, S. F., Gea, M., and Altamirano, M. (2015). "Least square based method for the estimation of the optical end loss of linear Fresnel concentrators". *Solar Energy* 111, pp. 264–276. DOI: 10.1016/j.solener.2014.10.042.

Incropera, F. P., DeWitt, D. P., Bergman, T. L., and Lavine, A. S. (2006). *Fundamentals of Heat and Mass Transfer*. 6th ed. John Wiley & Sons. ISBN: 978-0471457282.

Jaaz, A. H., Hasan, H. A., Sopian, K., Ruslan, M. H. B. H., and Zaidi, S. H. (2017). "Design and development of compound parabolic concentrating for photovoltaic solar collector: Review". *Renewable and Sustainable Energy Reviews* 76, pp. 1108–1121. DOI: 10.1016/j.rser.2017.03.127.

Jafarkazemi, F. and Ahmadifard, E. (2013). "Energetic and exergetic evaluation of flat plate solar collectors". *Renewable Energy* 56, pp. 55–63. DOI: 10.1016/j.renene.2012.10.031.

Kalogirou, S. A. (2004). "Solar thermal collectors and applications". *Progress in Energy and Combustion Science* 30.3, pp. 231–295. DOI: 10.1016/j.pecs.2004.02.001.

Karim, M. and Hawlader, M. (2004). "Development of solar air collectors for drying applications". *Energy Conversion and Management* 45.3, pp. 329–344. DOI: 10.1016/s0196-8904(03)00158-4.

Karsli, S. (2007). "Performance analysis of new-design solar air collectors for drying applications". *Renewable Energy* 32.10, pp. 1645–1660. DOI: 10.1016/j.renene.2006.08.005.

Khoukhi, M. and Maruyama, S. (2006). "Theoretical approach of a flat-plate solar collector taking into account the absorption and emission within glass cover layer". *Solar Energy* 80.7, pp. 787–794. DOI: 10.1016/j.solener.2005.06.002.

Kienzlen, V., Gordon, J. M., and Kreider, J. F. (1988). "The Reverse Flat Plate Collector: A Stationary, Nonevacuated, Low-Technology, Medium-Temperature Solar Collector". *Journal of Solar Energy Engineering* 110.1, p. 23. DOI: 10.1115/1.3268232.

Kostić, L. T. and Pavlović, Z. T. (2012). "Optimal position of flat plate reflectors of solar thermal collector". *Energy and Buildings* 45, pp. 161–168. DOI: 10.1016/j.enbuild.2011.10.059.

Kothdiwala, A. F., Eames, P. C., and Norton, B. (1997). "Experimental analysis and performance of an asymmetric inverted absorber compound parabolic concentrating solar collector at various absorber gap configurations". *Renewable Energy* 10.2-3, pp. 235–238. DOI: 10.1016/0960-1481(96)00071-7.

Kothdiwala, A. F., Eames, P. C., Norton, B., and Zacharopolous, A. (1999). "Technical note: Comparison between inverted absorber asymmetric and symmetric tubular-absorber compound parabolic concentrating solar collectors". *Renewable Energy* 18.2, pp. 277–281. DOI: 10.1016/s0960-1481(98)00786-1.

Kothdiwala, A. F., Eames, P. C., and Norton, B. (1996). "Optical performance of an asymmetric inverted absorber compound parabolic concentrating solar collector". *Renewable Energy* 9.1-4, pp. 576–579. DOI: 10.1016/0960-1481(96)88355-8.

Kothdiwala, A. F., Norton, B., and Eames, P. (1995). "The effect of variation of angle of inclination on the performance of low-concentration-ratio compound parabolic concentrating solar collectors". *Solar Energy* 55.4, pp. 301–309. DOI: 10.1016/0038-092x(95)00049-w.

Koyuncu, T. (2006). "Performance of various design of solar air heaters for crop drying applications". *Renewable Energy* 31.7, pp. 1073–1088. DOI: 10.1016/j.renene.2005.05.017.

Kurtbas, I. and Durmus, A. (2004). "Efficiency and exergy analysis of a new solar air heater". *Renewable Energy* 29.9, pp. 1489–1501. DOI: 10.1016/j.renene.2004.01.006.

Kutscher, C. F. (1994). "Heat Exchange Effectiveness and Pressure Drop for Air Flow Through Perforated Plates with and without Crosswind". *Journal of Heat Transfer* 116.2, pp. 391–399. DOI: 10.1115/1.2911411.

Leon, M. A. and Kumar, S. (2007). "Mathematical modeling and thermal performance analysis of unglazed transpired solar collectors". *Solar Energy* 81.1, pp. 62–75. DOI: 10.1016/j.solener.2006.06.017.

Li, X., Li, C., and Li, B. (2016). "Net heat gain assessment on a glazed transpired solar air collector with slit-like perforations". *Applied Thermal Engineering* 99, pp. 1–10. DOI: 10.1016/j.applthermaleng.2015.12.069.

Mallick, T and Eames, P (2007). "Design and fabrication of low concentrating second generation PRIDE concentrator". *Solar Energy Materials and Solar Cells* 91.7, pp. 597–608. DOI: 10.1016/j.solmat.2006.11.016.

Mallick, T. K., Eames, P. C., and Norton, B. (2006). "Non-concentrating and asymmetric compound parabolic concentrating building façade integrated photovoltaics: An experimental comparison". *Solar Energy* 80.7, pp. 834–849. DOI: 10.1016/j.solener.2005.05.011.

Mallick, T. K., Eames, P. C., and Norton, B. (2007). "Using air flow to alleviate temperature elevation in solar cells within asymmetric compound parabolic concentrators". *Solar Energy* 81.2, pp. 173–184. DOI: 10.1016/j.solener.2006.04.003.

McCabe, W. L., Smith, J. C., and Harriott, P. (1993). *Unit operations of chemical engineering*. McGraw-Hill, p. 1130. ISBN: 0070448442.

McIntire, W. R. (1979). "Truncation of nonimaging cusp concentrators". *Solar Energy* 23.4, pp. 351–355. DOI: 10.1016/0038-092x(79)90130-0.

Met Eireann (2018). *Historical Data*. URL: https://www.met.ie/climate/available-data/historical-data.

Michalopoulos, D. and Massouros, G. (Aug. 1994). "The effect of glazing on solar collectors". *Energy* 19.8, pp. 911–918. DOI: 10.1016/0360-5442(94)90044-2.

Mills, D. R. and Giutronich, J. E. (1978). "Asymmetrical non-imaging cylindrical solar concentrators". *Solar Energy* 20.1, pp. 45–55. DOI: 10.1016/0038-092x(78)90140-8.

Norton, B. (2012). "Industrial and Agricultural Applications of Solar Heat". *Comprehensive Renewable Energy*. Elsevier, pp. 567–594. DOI: 10.1016/b978-0-08-087872-0.00317-6.

Norton, B., Eames, P. C., and Yadav, Y. P. (1991). "Symmetric and asymmetric linear compound parabolic concentrating solar energy collectors: The state-of-the-art in optical and thermo-physical analysis". *International Journal of Ambient Energy* 12.4, pp. 171–190. DOI: 10.1080/01430750.1991.9675201.

Norton, B. (2006). "Anatomy of a solar collector". *Refocus* 7.3, pp. 32–35. DOI: 10.1016/s1471-0846(06)70570-4.

Nowzari, R., Mirzaei, N., and Aldabbagh, L. (2015). "Finding the best configuration for a solar air heater by design and analysis of experiment". *Energy Conversion and Management* 100, pp. 131–137. DOI: 10.1016/j.enconman.2015.04.058.

Oonk, R. L., Jones, D. E., and Cole-Appel, B. E. (1979). "Calculation of performance of N collectors in series from test data on a single collector". *Solar Energy* 23.6, pp. 535–536. DOI: 10.1016/0038-092X(79)90079-3.

Pottler, K., Sippel, C., Beck, A., and Fricke, J. (July 1999). "Optimized finned absorber geometries for solar air heating collectors". *Solar Energy* 67.1-3, pp. 35–52. DOI: 10.1016/S0038-092X(00)00036-0.

Pranesh, V., Velraj, R., Christopher, S., and Kumaresan, V. (2019). "A 50 year review of basic and applied research in compound parabolic concentrating solar thermal collector for domestic and industrial applications". *Solar Energy* 187, pp. 293–340. DOI: 10.1016/j.solener.2019.04.056.

Prapas, D. E., Norton, B., and Probert, S. D. (1987). "Optics of parabolic-trough, solar-energy collectors, possessing small concentration ratios". *Solar Energy* 39.6, pp. 541–550. DOI: 10.1016/0038-092x(87)90061-2.

Pu, S. and Xia, C. (2011). "End-Effect of Linear Fresnel Collectors". *Asia-Pacific Power and Energy Engineering Conference*. IEEE. DOI: 10.1109/APPEEC.2011.5748793.

Pujol-Nadal, R., Martínez-Moll, V., Sallaberry, F., and Moià-Pol, A. (2015). "Optical and thermal characterization of a variable geometry concentrator using ray-tracing tools and experimental data". *Applied Energy* 155, pp. 110–119. DOI: 10.1016/j.apenergy.2015.06.005.

Qin, H., Lei, C., Liu, H., Wang, Y., and Yuan, W. (2013). "Optical design of an aspherical cylinder-type reflecting solar concentrator". *Energy* 57, pp. 751–758. DOI: 10.1016/j.energy.2013.05.059.

Rabl, A., O'Gallagher, J., and Winston, R. (1980). "Design and test of non-evacuated solar collectors with compound parabolic concentrators". *Solar Energy* 25.4, pp. 335–351. DOI: 10.1016/0038-092X(80)90346-1.

Rabl, A. (1976a). "Comparison of solar concentrators". *Solar Energy* 18.2, pp. 93–111. DOI: 10.1016/0038-092x(76)90043-8.

Rabl, A. (1976b). "Optical and Thermal Properties of Compound Parabolic Concentrators". *Solar Energy* 18.6, pp. 497–511. DOI: 10.1016/0038-092x(76)90069-4.

Rabl, A. (1985). *Active Solar Collectors and Their Applications*. Oxford University Press. 518 pp. ISBN: 0195035461.

Ratismith, W., Inthongkhum, A., and Briggs, J. (2014). "Two non-tracking solar collectors: Design criteria and performance analysis". *Applied Energy* 131, pp. 201–210. DOI: 10.1016/j.apenergy.2014.06.030.

Roux, W. L. (2016). "Optimum tilt and azimuth angles for fixed solar collectors in South Africa using measured data". *Renewable Energy* 96, pp. 603–612. DOI: 10.1016/j.renene.2016.05.003.

Sarmah, N., Richards, B. S., and Mallick, T. K. (2011). "Evaluation and optimization of the optical performance of low-concentrating dielectric compound parabolic concentrator using ray-tracing methods". *Applied Optics* 50.19, pp. 3303–3310. DOI: 10.1364/ao.50.003303.

Saxena, A., Varun, and El-Sebaii, A. (2015). "A thermodynamic review of solar air heaters". *Renewable and Sustainable Energy Reviews* 43, pp. 863–890. DOI: 10.1016/j.rser.2014.11.059.

Sellami, N. and Mallick, T. K. (2013). "Optical efficiency study of PV Crossed Compound Parabolic Concentrator". *Applied Energy* 102, pp. 868–876. DOI: 10.1016/j.apenergy.2012.08.052.

Sellami, N., Mallick, T. K., and McNeil, D. A. (2012). "Optical characterisation of 3-D static solar concentrator". *Energy Conversion and Management* 64, pp. 579–586. DOI: 10.1016/j.enconman.2012.05.028.

Shams, N. (2013). "Design of a Transpired Air Heating Solar Collector with an Inverted Perforated Absorber and Asymmetric Compound Parabolic Concentrator". PhD Thesis. Dublin Institute of Technology. Dublin, Ireland. DOI: 10.21427/D7NK67.

Shams, S. M. N., Keever, M. M., Cormack, S. M., and Norton, B. (2016). "Design and experiment of a new solar air heating collector". *Energy* 100, pp. 374–383. DOI: 10.1016/j.energy.2015.12.136.

Shukla, A., Nkwetta, D. N., Cho, Y., Stevenson, V., and Jones, P. (2012). "A state of art review on the performance of transpired solar collector". *Renewable and Sustainable Energy Reviews* 16.6, pp. 3975–3985. DOI: 10.1016/j.rser.2012.02.029.

Smyth, M., McGarrigle, P., Eames, P. C., and Norton, B. (2005). "Experimental comparison of alternative convection suppression arrangements for concentrating integral collector storage solar water heaters". *Solar Energy* 78.2, pp. 223–233. DOI: 10.1016/j.solener.2004.06.004.

Smyth, M., Zacharopoulos, A., Eames, P., and Norton, B. (1999). "An experimental procedure to determine solar energy flux distributions on the absorber of line-axis compound parabolic concentrators". *Renewable Energy* 16.1-4, pp. 761–764. DOI: 10.1016/s0960-1481(98)00274-2.

Soares, M. A. B., Matos Jorge, L. M. de, and Montanuci, F. D. (2016). "Drying kinetics of barley grains and effects on the germination index". *Food Science and Technology* 36.4, pp. 638–645. DOI: 10.1590/1678-457X.11916.

Solar Tribune (2011). *Solar Air Collectors*. URL: https://solartribune.com/solar-hot-air-panels/.

Souliotis, M., Quinlan, P., Smyth, M., Tripanagnostopoulos, Y., Zacharopoulos, A., Ramirez, M., and Yianoulis, P. (2011). "Heat retaining integrated collector storage solar water heater with asymmetric CPC reflector". *Solar Energy* 85.10, pp. 2474–2487. DOI: 10.1016/j.solener.2011.07.005.

SunCalc (May 2, 2018). *Computation path of the Sun*. Ed. by T. Hoffmann. URL: https://www.suncalc.org/#/53.3621,-6.2779,5/.

Syngenta (July 2, 2020). *Drying malt barley for acceptance*. URL: https://www.syngenta.ca/agronomy/drying-malt-barley.

Tchinda, R. (2008). "Thermal behaviour of solar air heater with compound parabolic concentrator". *Energy Conversion & Management* 49, pp. 529–540. DOI: 10.1016/j.enconman.2007.08.004.

Tian, M., Su, Y., Zheng, H., Pei, G., Li, G., and Riffat, S. (2018). "A review on the recent research progress in the compound parabolic concentrator (CPC) for solar energy applications". *Renewable and Sustainable Energy Reviews* 82, pp. 1272–1296. DOI: 10.1016/j.rser.2017.09.050.

Time and Date (May 2, 2018). *Sun calculator*. Ed. by K. Bikos. URL: https://www.timeanddate.com/sun/ireland/dublin.

Tiwari, G. and Suneja, S. (1998). "Performance evaluation of an inverted absorber solar still". *Energy Conversion and Management* 39.3-4, pp. 173–180. DOI: 10.1016/s0196-8904(96)00227-0.

Tonui, J. and Tripanagnostopoulos, Y. (2007). "Air-cooled PV/T solar collectors with low cost performance improvements". *Solar Energy* 81.4, pp. 498–511. DOI: 10.1016/j.solener.2006.08.002.

Tonui, J. and Tripanagnostopoulos, Y. (2008). "Performance improvement of PV/T solar collectors with natural air flow operation". *Solar Energy* 82.1, pp. 1–12. DOI: 10.1016/j.solener.2007.06.004.

Tourlonias, M. and Bueno, M.-A. (2016). "Experimental simulation of friction and wear of carbon yarns during the weaving process". *Composites Part A: Applied Science and Manufacturing* 80, pp. 228–236. DOI: 10.1016/j.compositesa.2015.07.024.

Tripanagnostopoulos, Y, Yianoulis, P, Papaefthimiou, S, and Zafeiratos, S (2000). "CPC Solar Collectors With Flat Bifacial Absorbers". *Solar Energy* 69.3, pp. 191–203. DOI: 10.1016/s0038-092x(00)00061-x.

Tyagi, V., Panwar, N., Rahim, N., and Kothari, R. (2012). "Review on solar air heating system with and without thermal energy storage system". *Renewable and Sustainable Energy Reviews* 16.4, pp. 2289–2303. DOI: 10.1016/j.rser.2011.12.005.

Ustaoglu, A., Alptekin, M., Okajima, J., and Maruyama, S. (2016). "Evaluation of uniformity of solar illumination on the receiver of compound parabolic concentrator (CPC)". *Solar Energy* 132, pp. 150–164. DOI: 10.1016/j.solener.2016.03.014.

Wall, M., Probst, M. C. M., Roecker, C., Dubois, M.-C., Horvat, M., Jørgensen, O. B., and Kappel, K. (2012). "Achieving Solar Energy in Architecture-IEA SHC Task 41". *Energy Procedia* 30, pp. 1250–1260. DOI: 10.1016/j.egypro.2012.11.138.

Winston, R. (1974). "Principles of solar concentrators of a novel design". *Solar Energy* 16.2, pp. 89–95. DOI: 10.1016/0038-092x(74)90004-8.

Winston, R., Minano, J. C., and Benitez, P. G. (2005). *Nonimaging Optics*. Academic Press. ISBN: 0-12-759751-4. DOI: 10.1016/B978-0-12-759751-5.X5000-3.

Wu, S. S., Boley, C. D., Florando, J. N., LeBlanc, M. M., Lowdermilk, W. H., Rubenchik, S. M., and Stanley, J. R. (2012). *Deep Penetration in Aerospace Composite Materials Using Near-Infrared Laser Radiation*. Tech. rep. Livermore, United States: Lawrence Livermore National Lab. (LLNL). DOI: 10.2172/1059098.

Wu, Y. (2009). "Thermal Management of Concentrator Photovoltaics". PhD Thesis. University of Warwick. Warwick, UK. URL: http://go.warwick.ac.uk/wrap/3218.

Xu, C., Chen, Z., Li, M., Zhang, P., Ji, X., Luo, X., and Liu, J. (Feb. 2014). "Research on the compensation of the end loss effect for parabolic trough solar collectors". *Applied Energy* 115, pp. 128–139. DOI: 10.1016/j.apenergy.2013.11.003.

Yeh, H. M. and Ho, C. D. (2009). "Solar air heaters with external recycle". *Applied Thermal Engineering* 29.8-9, pp. 1694–1701. DOI: 10.1016/j.applthermaleng.2008.07.027.

Yousef, B. and Adam, N. (2008). "Performance analysis for flat plate collector with and without porous media". *Journal of Energy in Southern Africa* 19.4, pp. 32–42. DOI: 10.17159/2413-3051/2008/v19i4a3336.

Zacharopoulos, A., Eames, P. C., McLarnon, D., and Norton, B. (2000). "Linear Dielectric Non-Imaging Concentrating Covers For PV Integrated Building Facades". *Solar Energy* 68.5, pp. 439–452. DOI: 10.1016/s0038-092x(00)00013-x.

Zheng, H., Tao, T., Dai, J., and Kang, H. (2011). "Light tracing analysis of a new kind of trough solar concentrator". *Energy Conversion and Management* 52.6, pp. 2373–2377. DOI: 10.1016/j.enconman.2010.12.042.

Zheng, W., Li, B., Zhang, H., You, S., Li, Y., and Ye, T. (2016). "Thermal characteristics of a glazed transpired solar collector with perforating corrugated plate in cold regions". *Energy* 109, pp. 781–790. DOI: 10.1016/j.energy.2016.05.064.

Zomorodian, A. and Zamanian, M. (2012). "Designing and Evaluating an Innovative Solar Air Collector with Transpired Absorber and Cover". *ISRN Renewable Energy* 2012, pp. 1–5. DOI: 10.5402/2012/282538.